Molecules in intense laser fields: Studies of ionization, high-order harmonic generation and alignment

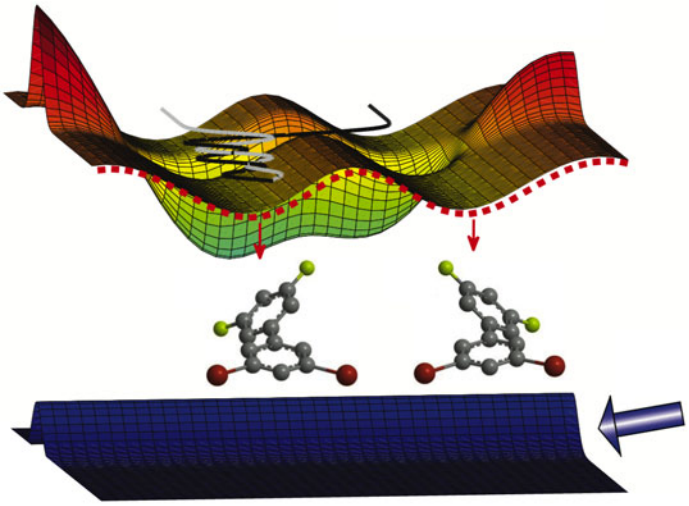

Christian Bruun Madsen

Lundbeck Foundation Theoretical Center for Quantum System Research
Department of Physics and Astronomy
University of Aarhus
DK-8000 Århus C
Denmark

PhD Thesis
August 2010

This thesis is submitted to the Faculty of Science at the University of Aarhus, Denmark, in order to fulfill the requirements for obtaining the PhD degree in Physics. The studies have been carried out under the supervision of Associate Professor Lars Bojer Madsen in the Lundbeck Foundation Theoretical Center for Quantum System Research at the Department of Physics and Astronomy.

Til mine forældre

Preface

In this dissertation you will find a presentation of the work I have been involved in during my PhD program. This research was carried out in the period from August 1st 2006 to July 31st 2010 under supervision of Lars Bojer Madsen. Most of the work covered in this thesis has been presented in the publications listed below. I hope, however, in this document the reader will find a more in-depth and comprehensive discussion of my research. Further, Chapter 3 and parts of Chapters 6 and 7 cover unpublished work.

List of publications

i C. B. Madsen and L. B. Madsen, *High-order harmonic generation from arbitrarily oriented diatomic molecules including nuclear motion and field-free alignment*, Phys. Rev. A **74**, 023403 (2006)

ii C. B. Madsen, A. S. Mouritzen, T. K. Kjeldsen and L. B. Madsen, *Effects of orientation and alignment in high-order harmonic generation and above-threshold ionization*, Phys. Rev. A **76**, 035401 (2007)

iii C. B. Madsen and L. B. Madsen, *Theoretical studies of high-order harmonic generation: Effects of symmetry, degeneracy, and orientation*, Phys. Rev. A **76**, 043419 (2007)

iv V. Kumarappan, L. Holmegaard, C. Martiny, C. B. Madsen, T. K. Kjeldsen, S. S. Viftrup, L. B. Madsen and H. Stapelfeldt, *Multiphoton Electron Angular Distributions from Laser-Aligned CS_2 Molecules*, Phys. Rev. Lett. **100**, 093006 (2008)

v C. B. Madsen, L. B. Madsen, S. S. Viftrup, M. P. Johansson, T. B. Poulsen, L. Holmegaard, V. Kumarappan, K. A. Jørgensen and H. Stapelfeldt, *Manipulating the Torsion of Molecules by Strong Laser Pulses*, Phys. Rev. Lett. **102**, 073007 (2009)

vi C. B. Madsen, L. B. Madsen, S. S. Viftrup, M. P. Johansson, T. B. Poulsen, L. Holmegaard, V. Kumarappan, K. A. Jørgensen and H. Stapelfeldt, *A combined experimental and theoretical study on realizing and using laser controlled torsion of molecules*, J. Chem. Phys. **130**, 234310 (2009)

vii A. Etches, C. B. Madsen and L. B. Madsen, *Inducing elliptically polarized high-order harmonics from aligned molecules with linearly polarized femtosecond pulses*, Phys. Rev. A **81**, 013409 (2010)

viii C. B. Madsen, M. Abu-samha and L. B. Madsen, *High-order harmonic generation from polyatomic molecules including nuclear motion and a nuclear modes analysis*, Phys. Rev. A **81**, 043413 (2010)

Papers in preparation

ix C. B. Madsen, F. Anis, L. B. Madsen and B. D. Esry, *Correlated electron-nuclear continuum energy distribution following strong-field ionization of* H_2^+, in preparation

x C. B. Madsen and L. B. Madsen, *Influence of the torsion on high-order harmonic generation from biphenyl*, in preparation

Acknowledgments

First of all, I would like to thank my supervisor Lars Bojer Madsen who has been an excellent role model for me since I started working in his research group in 2005. His encouraging and careful supervision, and his emphasis on developing my ingenuity and creativity has greatly shaped me as a physicist.

I would also like to acknowledge my fellow students with whom I have shared many joyful hours at the office: Heine Thomsen, Henriette Leth, Anne Nielsen and Christian Martiny. I would like to extend a special thanks to Christian Martiny for the many enjoyable and productive collaborations and discussions since we started exploring the area of strong-field physics together in the fall of 2004.

I have appreciated working closely with several group members from the Lundbeck Foundation Theoretical Center for Quantum System Research. This includes Thomas Kjeldsen, who introduced me to many concepts of strong-field physics. Later, Thomas Kjeldsen as well as Anders Mouritzen and I revisited some fundamental concepts of the quantities measured in modern laser experiments. Over the last couple of years I have benefited from the company and skills of Adam Etches and Mahmoud Abu-samha in my studies of high-order harmonic generation from molecules.

Also, I thank Femtolab for a very fruitful collaboration and point out numerous instructive discussions with Henrik Stapelfeldt. This interaction has been invaluable and has greatly affected my research on laser-induced alignment and systems involving lasers and complex molecules.

For their hospitality in the first half-year of 2009, I would like to thank Brett Esry and his research group at Kansas State University, Manhattan, USA. Here I was taught many new aspects of computational physics in solving the time-dependent Schrödinger equation for H_2^+ in a laser field and further enjoyed the collaboration with several of the other research groups at the J. R. Macdonald Laboratory.

I owe much to my family for always supporting me and especially my parents for believing in me and encouraging me to pursue my interests since I was a young boy in elementary school.

A special thanks goes to Varun Makhija and Michael Chini for proofreading this thesis.

Last but not least, I am very thankful for the endless love and support from my fiancée Adrian.

Contents

1 Introduction and thesis outline **1**
- 1.1 Introduction . . . 1
- 1.2 Outline of the thesis . . . 3

2 Charged particles in laser fields **5**
- 2.1 The laser field . . . 5
- 2.2 The time-dependent Schrödinger equation . . . 7
  - 2.2.1 Gauge considerations . . . 8
- 2.3 Summary . . . 8

3 Ionization of H_2^+ in one dimension **11**
- 3.1 The one dimensional model . . . 11
- 3.2 Numerical solution of the TDSE . . . 12
  - 3.2.1 FEDVR . . . 12
  - 3.2.2 Lanczos propagator . . . 13
- 3.3 Energy analysis . . . 15
- 3.4 Results and discussion . . . 15
- 3.5 Summary . . . 21

4 HHG and ionization **23**
- 4.1 An introduction to HHG . . . 23
- 4.2 Influence of nuclear degrees of freedom on HHG . . . 25
- 4.3 Influence of nuclear degrees of freedom on ionization . . . 27
- 4.4 Summary . . . 29

5 HHG and ionization in the strong-field approximation **31**
- 5.1 Introduction to the SFA . . . 31
- 5.2 The Lewenstein model for HHG . . . 32
  - 5.2.1 The molecular orbital in a Gaussian basis . . . 33
  - 5.2.2 Evaluation of the momentum integral . . . 34
  - 5.2.3 Treating molecular orientation in the Lewenstein model 35
- 5.3 HHG in the Kuchiev-Ostrovsky model . . . 36
  - 5.3.1 The molecular orbital in the Kuchiev-Ostrovsky model . 36
  - 5.3.2 Expression for HHG . . . 37
  - 5.3.3 Asymptotic expression for HHG . . . 38
- 5.4 Semiclassical orbits in the model calculations of HHG . . . 39

5.5 Ionization in the SFA 41
5.6 Summary 41

6 HHG and the influence of molecular structure 43
6.1 Signature of ionization and recombination in the HHG signal . 43
6.2 Polarization effects 47
6.2.1 Elliptically polarized harmonics from N_2 with a linearly polarized driving pulse 48
6.2.2 Structural interference effects 52
6.3 HHG as probe of molecular torsion 53
6.4 Summary 54

7 HHG and the influence of molecular vibration 57
7.1 The basics of vibration in HHG 57
7.2 Tracing nuclear reconfiguration of methane with HHG 59
7.2.1 Structure of methane 59
7.2.2 High-order harmonic spectra and nuclear motion 60
7.2.3 Discussion of the the current treatment of nuclear motion 61
7.3 The influence of nuclear motion on heavy molecules 63
7.3.1 The N_2 molecule – negligible effect of nuclear motion . . 64
7.3.2 The O_2 molecule – significant effect of nuclear motion . 65
7.4 The potential for using HHG to probe nuclear dynamics in ethylene 66
7.5 Summary 68

8 Laser induced alignment and orientation 69
8.1 The principle of laser induced alignment 69
8.2 Quantum mechanical description 71
8.3 Summary 75

9 ATI and HHG from aligned and oriented molecules 77
9.1 Calculating the alignment dynamics of linear molecules 77
9.2 Ionization from aligned CS_2 79
9.2.1 The experimental setup 79
9.2.2 Experimental observations 80
9.2.3 Modeling the experiment using the strong-field approximation 82
9.2.4 Shortcomings of the strong-field approximation 84
9.3 HHG from the oriented CO molecules 84
9.4 Summary 85

10 Laser controlled torsion of molecules 87
10.1 The principle of laser controlled torsion of molecules 88
10.2 The experimental setup 89
10.2.1 Experimental observations 89
10.3 A semi-classical theory on laser controlled torsion 92
10.3.1 Modeling the molecule 92

10.3.2 Laser induced dynamics 96
10.4 Theoretical results 97
10.5 Outlook 100
10.6 Summary 102

11 Summary (Dansk resumé) 103
11.1 Dansk resumé 104

A Numerical solution of the TDSE 107
A.1 FEDVR 107
A.2 Finding the outgoing scattering states 110

B Determining Franck-Condon integrals 113

Bibliography 117

Chapter 1

Introduction and thesis outline

1.1 Introduction

The study of light-matter interactions at the atomic level dates back more than one hundred years starting with Heinrich Hertz' discovery of the photoelectric effect and Johann Balmers observations of the hydrogen emission lines in the late 1880s. These observations led to the concept of photons introduced by Einstein in 1905 to explain the photoelectric effect and to Bohr's quantum model of the atom from 1913 that reproduced Balmer lines. The early investigations of emission and absorption spectra of atoms and molecules provided a wealth of knowledge about both the nature of light and about electronic structure and the desire for a deeper understanding of these phenomena led to the development of quantum mechanics in the first half of the 1900s. When coherent and monochromatic laser radiation became available starting in the 1960s, our knowledge of the structure of atoms and molecules was further revolutionized.

Over the last couple of decades intense lasers between 10^{13} and 10^{15} W/cm^2 have become standard equipment in laboratories worldwide. These are the types of laser fields we will be concerned with in this thesis. They are *'intense'* in the sense that the flux of the incident photons is so high that a classical description of the laser field is sufficient and the strength of the applied laser is comparable to or much stronger than the electric field strength that binds the outer shell electrons.[1] These lasers will usually emit short laser pulses of less than 100 fs (1 fs=10^{-15} s) at an infrared central wavelength of around 800 nm. Electrons are so strongly driven by these fields that normal perturbative approaches break down, and new theoretical methods are required. With these new methods emerges a series of novel phenomena such as the absorption of more photons than the minimum required for ionization, also known as above-threshold ionization (ATI), and the conversion of a large number of laser

[1] Note that we work in the intensity regime where non-relativistic quantum mechanics is still appropriate.

photons into a single photon of high frequency in a process called high-order harmonic generation (HHG).

Ionization is one of the most fundamental and important strong-field processes to understand. For example, ionization is the key initial process in HHG, as we will see in Chapter 4. Additionally, many experiments rely on the detection of electrons created by a strong ionizing pulse and any interpretation of such experiments relies on the understanding of strong-field ionization. When molecules ionize, the additional freedom associated with nuclear motion gives rise to phenomena that do not occur for atoms in strong fields. These include the softening and hardening of molecular bonds by the strong laser fields and molecules absorbing more photons than necessary to dissociate, similar to ATI [11].

If a laser field is intense but non-ionizing, the forces and torques that the field applies to a molecule can be sufficient to effectively manipulate the external degrees of freedom. In particular, the intensity gradient of a focused laser beam may deflect, focus and slow molecules. The dependence of the induced dipole interaction on molecular orientation has proven highly useful for controlling the alignment and rotation of a variety of molecules [12]. Molecular manipulation by induced dipole forces extends beyond external degrees of freedom and can also be applied to internal degrees of freedom such as vibrational motion and the internal rotation or, as we will discuss in Chapter 10, torsion of molecules.

The interaction of intense lasers with atoms and molecules revived and renewed the field of atomic, molecular and optical physics by moving it away from an arena that is well understood with perturbative methods. Looking alone at the rate at which papers on this topic are published and cited in high-impact peer-reviewed journals such as Nature, Science, and Physical Review Letters demonstrates the growing interest and activity occurring in this field. However, the new physics involved in laser-matter interaction is not only interesting in its own right. As the research field is maturing, interesting applications are evolving for using the intense laser fields to investigate ultrafast dynamical processes in different systems, ranging from small molecules to complex biological systems. Using pump-probe techniques with ultrashort laser pulses, one can monitor molecular motion (such as vibrations, or making and breaking of molecular bonds) occurring on the femtosecond timescale and thus gain invaluable insight into the structure and the short-time dynamics of molecules. This concept has led to the birth of femto chemistry for which the 1999 Nobel Prize in chemistry was awarded to Ahmed Zewail [13]. In the HHG process, the generated radiation is coherent and is used for creating attosecond pulses [14]. Further, HHG is used as a diagnostic tool to determine molecular properties such as the internuclear distance [15–17] or photo recombination cross section [18]. Finally, HHG holds the promise of attosecond imaging of molecular electronic wavepackets [19, 20]. Ultimately, the above techniques may become standard methods to steer chemical reactions and observe electronic dynamics in real time [21].

1.2 Outline of the thesis

In this thesis we will look at ionization, high-order harmonic generation and alignment. We will start out in Chapter 2 by discussing how to treat the laser-molecule interaction for the typical intense laser of optical frequencies. This material is well known from courses on atomic and molecular physics. In Chapter 3 we investigate the ionization of the H_2^+ molecular ion by a linearly polarized laser field. Both nuclear and electron dynamics are taken into account, but restricted to the dimension of the laser electric field, and we study the joint energy distribution of the products from ionization. Chapter 4 discusses the relationship between the observables of high-harmonic generation and ionization and the quantities calculated in theoretical models. We then go on to describe how to calculate HHG and above-threshold ionization (ATI) within the strong field approximation (SFA) in Chapter 5. In Chapters 6 and 7 we look at results obtained within the SFA that uncover the effect of molecular structure and vibrations on HHG. We then move to something different, namely laser-induced alignment and orientation. Chapter 8 gives a basic introduction on laser-induced alignment. We then revisit HHG and ATI by calculating signals from aligned targets. In Chapter 10 we demonstrate how to use lasers to control the torsion of molecules. Chapter 11 contains a conclusion and an outlook. Appendix A contains a review of some numerical methods that are used in Chapter 3. Appendix B presents a method for calculating Franck-Condon factors as these are needed to treat the influence of nuclear motion on HHG.

Atomic units, $m_e = e = a_0 = \hbar = 1$, are used throughout unless otherwise indicated.

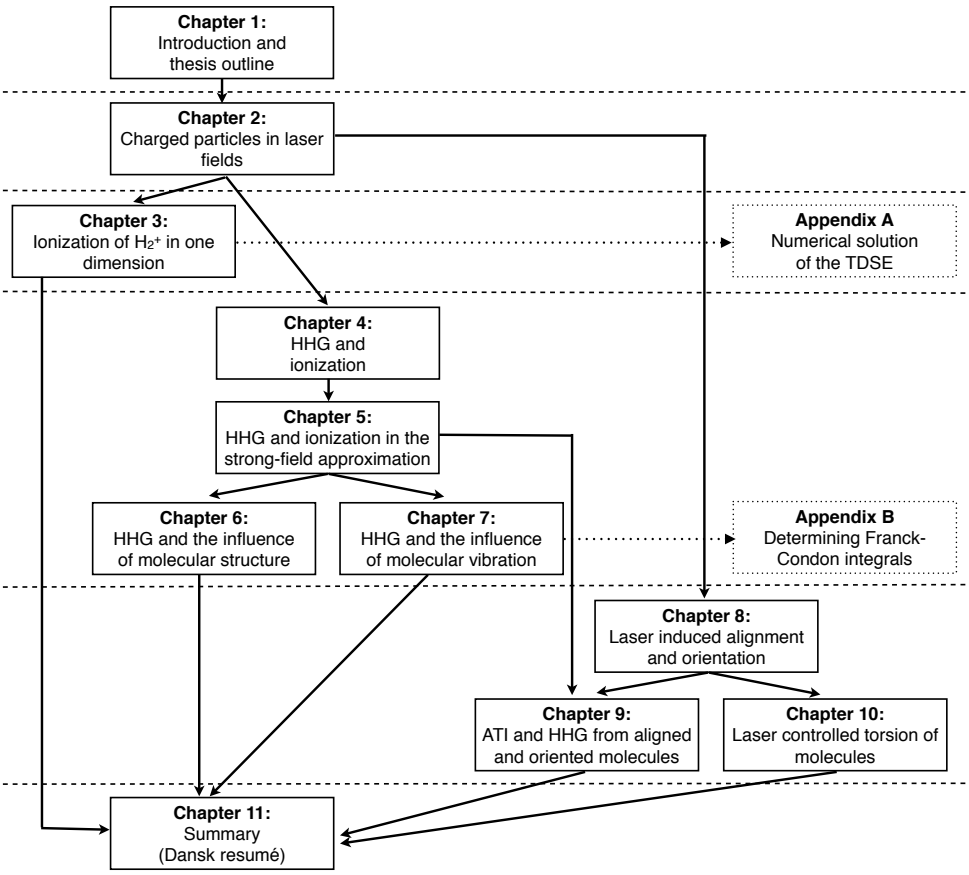

Figure 1.1: Reading guide to the thesis.

Chapter 2

Charged particles in laser fields

The first thing we must do is to set up the theoretical framework that describes the interaction between particles and electromagnetic fields. Although we often imagine that the particle under consideration is the electron, this chapter treats an arbitrary particle with charge q and mass M.

In a rigorous treatment, we would have to start by studying quantum electrodynamics, in which the electromagnetic field is expressed in terms of its quanta, the photons. However, even in comparatively weak fields the photon density can be very high implying that the number of photons can be treated as a continuous variable and consequently the field can be described classically using Maxwell's equations. This leads to the *semi-classical* theory in which the radiation field is treated classically, but the molecular system is described using quantum mechanics. We will also assume that the influence of the atom on the external field can be neglected.

2.1 The laser field

The classical electromagnetic field is described by the electric and magnetic field vectors $\boldsymbol{F}$ and $\boldsymbol{B}$, which satisfy Maxwell's Equations [22]. We shall express these quantities using SI units. The electric field $\boldsymbol{F}$ and magnetic field $\boldsymbol{B}$ can be generated from scalar and vector potentials ϕ and $\boldsymbol{A}$ by

$$\boldsymbol{F}(\boldsymbol{r},t) = -\boldsymbol{\nabla}\phi(\boldsymbol{r},t) - \frac{\partial}{\partial t}\boldsymbol{A}(\boldsymbol{r},t). \tag{2.1}$$

and

$$\boldsymbol{B}(\boldsymbol{r},t) = \boldsymbol{\nabla} \times \boldsymbol{A}(\boldsymbol{r},t). \tag{2.2}$$

The potentials are not completely defined by these equations, since the physical fields, $\boldsymbol{F}$ and $\boldsymbol{B}$, are invariant under the (classical) *gauge transformation* $\boldsymbol{A} \to \boldsymbol{A} + \nabla\chi, \phi \to \phi - \partial\chi/\partial t$, where χ is any real, differentiable function of $\boldsymbol{r}$ and t. The freedom implied by this *gauge invariance* allows us to impose a

further condition on the vector potential $\boldsymbol{A}$, which we shall choose to be

$$\nabla \cdot \boldsymbol{A}(\boldsymbol{r}, t) = 0 \tag{2.3}$$

When $\boldsymbol{A}$ satisfies this condition, we are said to be using the *Coulomb gauge*. This choice of gauge is convenient when no sources are present, which is the case being considered here. One may then take $\phi = 0$, and $\boldsymbol{A}$ satisfies the wave equation

$$\nabla^2 \boldsymbol{A}(\boldsymbol{r}, t) - \frac{1}{c^2} \frac{\partial^2}{\partial t^2} \boldsymbol{A}(\boldsymbol{r}, t) = 0 \tag{2.4}$$

where c is the velocity of light in vacuum.

For a monochromatic field with the electric field polarized along the unit vector $\boldsymbol{e}$ the solution may be written as

$$\boldsymbol{A}(\boldsymbol{r}, t) = \boldsymbol{e} \frac{F_0}{\omega_0} \sin(\omega_0 t - \boldsymbol{k} \cdot \boldsymbol{r} + \delta_0) \tag{2.5}$$

$$\boldsymbol{F}(\boldsymbol{r}, t) = \boldsymbol{e} F_0 \cos(\omega_0 t - \boldsymbol{k} \cdot \boldsymbol{r} + \delta_0) \tag{2.6}$$

$$\boldsymbol{B}(\boldsymbol{r}, t) = \boldsymbol{k} \times \boldsymbol{e} \frac{F_0}{\omega_0} \cos(\omega_0 t - \boldsymbol{k} \cdot \boldsymbol{r} + \delta_0) \tag{2.7}$$

where $\boldsymbol{k}$ is the wave vector that denotes the propagation direction of the electromagnetic field, ω_0 is the angular frequency, and δ_0 is the phase of the laser field. Here, the dispersion relation $\omega_0 = kc$ holds. We shall only be concerned with linearly polarized laser fields in this report.

For infrared, optical, and ultraviolet light with wavelengths 100 nm $\leq \lambda \leq$ 1000 nm interacting with molecules, the bound electrons are typically confined within a region of radius $a \sim 1$ nm. Therefore $|\boldsymbol{k} \cdot \boldsymbol{r}| \leq ka = (2\pi/\lambda)a \ll 1$ and the dipole approximation holds, i.e., $\exp(i\boldsymbol{k} \cdot \boldsymbol{r}) \sim 1$. Physically, the dipole approximation means that the molecules are small enough that the electric field does not change appreciably over the dimensions of the molecule and as such we may assume that the fields are constant in space. Since the vector potential only depends on time within this approximation the magnetic field vanishes according to Eq. (2.2).

In the SI system, one atomic unit of field strength is given by $F_{0,\mathrm{au}} = e/(4\pi\epsilon_0 a_0^2)$ with e the size of the electron charge, a_0 the Bohr radius and ϵ_0 the vacuum permittivity. We find $F_{0,\mathrm{au}} = 5.14 \times 10^9$ V/cm. The corresponding unit of intensity is the time averaged Poynting vector $I_{0,\mathrm{au}} = |F_{0,\mathrm{au}}|^2/(2\mu_0 c)$, where the factor of $1/2$ comes from the time-averaging, and μ_0 is the vacuum permeability. We plug in numbers and find $I_{0,\mathrm{au}} = 3.51 \times 10^{16}$ W/cm^2. This determines how we relate the peak field strength, F_0, and intensity, I, in this report:

$$F_0 = \sqrt{\frac{I(\mathrm{W/cm^2})}{3.51 \times 10^{16}}} \text{ [a.u.]} \tag{2.8}$$

The $\boldsymbol{F}$ and $\boldsymbol{B}$ fields that follow from Eq. (2.5) have infinite extension in both temporal and spatial dimensions. While such a description is appropriate for fields induced by continuous wave lasers, this situation obviously cannot

correspond to a short laser pulse. Instead, a pulse of finite duration can be produced by a superposition of plane waves with different frequencies and with a well-defined phase relationship between the frequency components. Then, for a superposition of plane waves with the same polarization $\boldsymbol{e}$ and with the same propagation direction, it is possible to obtain a field of finite duration T of the form

$$\boldsymbol{F}(t) = \boldsymbol{e}F_0 h(t)\cos(\omega_0 t + \delta), \tag{2.9}$$

where $h(t)$ is an envelope function which is zero outside the time interval $t \in (t_0, t_0 + T)$ and varies somewhat slower than the oscillating cosine factor. We will be using sinusoidal, trapezoidal and gaussian envelopes in this thesis and further we will only study cases with $\delta = 0$. We find the vector potential as $\boldsymbol{A}(t) = -\int_{t_0}^{t} \boldsymbol{F}(t')dt'$. Note that the value $\boldsymbol{A}(t_0 + T)$ is equivalent to the integral of the electric field over all times, in other words, the zero-frequency or dc component of the laser electric field. Such a component is not allowed for a propagating laser pulse and consequently we see that $\boldsymbol{A}(t_0 + T) = 0$ has to be fulfilled.

2.2 The time-dependent Schrödinger equation

The classical electromagnetic field from the previous section needs to be incorporated into the time-dependent Schrödinger equation (TDSE). The coupling between the laser and the charged particle is described by replacing the momentum operator of the electron with the minimal coupled momentum, $\boldsymbol{p} \to \boldsymbol{p} - q\boldsymbol{A}$ [23] and the procedure leads to

$$i\frac{\partial}{\partial t}\Psi'(\boldsymbol{r},t) = H(t)\Psi'(\boldsymbol{r},t) = \left[\frac{(\boldsymbol{p} - q\boldsymbol{A}(t))^2}{2M} + V(\boldsymbol{r})\right]\Psi'(\boldsymbol{r},t) \tag{2.10}$$

$$= \left[\frac{\boldsymbol{p}^2}{2M} + V(\boldsymbol{r}) - \frac{q}{M}\boldsymbol{A}(t)\cdot\boldsymbol{p} + \frac{q^2\boldsymbol{A}(t)^2}{2M}\right]\Psi'(\boldsymbol{r},t), \tag{2.11}$$

where we assume that the potential depends only on the spatial coordinate $\boldsymbol{r}$. When the interaction of the charged particle with the field is represented in this way, the interaction is described by the *velocity gauge* (VG). In VG, the interaction of the field with the atom is represented by the term $(-q/M)\boldsymbol{A}(t)\cdot\boldsymbol{p}$. Since the first two terms of Eq. (2.11) are simply the Hamiltonian describing the charged particle in the absence of any laser field, we will often denote this by the *field-free Hamiltonian*, H_0.

The transformation

$$\Psi(\boldsymbol{r},t) = e^{-iq\boldsymbol{r}\cdot\boldsymbol{A}(t)}\Psi'(\boldsymbol{r},t) \tag{2.12}$$

can be substituted into Eq. (2.11) leading to the *length gauge* (LG) equation:

$$i\frac{\partial}{\partial t}\Psi(\boldsymbol{r},t) = \left[\frac{\boldsymbol{p}^2}{2M} + V(\boldsymbol{r}) - q\boldsymbol{r}\cdot\boldsymbol{F}\right]\Psi(\boldsymbol{r},t). \tag{2.13}$$

In this form the laser field couples to the displacement $\boldsymbol{r}$ or "length" of the charged particle.

2.2.1 Gauge considerations

From a physical point of view, there are a couple of features that favor LG over VG. First, in VG the kinematic momentum, which is the measurable quantity, is related to the canonical momentum, $\boldsymbol{p}$, through the vector potential $M\boldsymbol{v}(t) = \boldsymbol{p} - q\boldsymbol{A}(t)$, i.e., the two quantities do not coincide. The difference in canonical and kinematic momentum in VG leads to a number of surprising results. One example comes about if the potential, V is not simply dependent on $\boldsymbol{r}$, but is rather non-local. Such a potential is a key ingredient in many *ab inito* electronic structure calculations as it eliminates the largely inert and thus physically unimportant core electrons. The price to be paid in VG is that the time-dependent vector potential shift of the kinematic momentum enters the supposedly field-free non-local potential that the valence electrons feel [25]. In LG, the kinematic momentum is $M\boldsymbol{v}(t) = \exp[-iq\boldsymbol{r}\cdot\boldsymbol{A}(t)][\boldsymbol{p} - q\boldsymbol{A}(t)]\exp[iq\boldsymbol{r}\cdot\boldsymbol{A}(t)] = \boldsymbol{p}$ and thus is identical to the canonical momentum and none of these surprising issues appear. Another and maybe more important property of the LG Hamiltonian is the fact that the interaction of the laser field with the unperturbed system enters as a time-dependent (spatial) deformation of the potential V. Such interaction is easily envisioned physically as one may draw the modified potential curves at any point of time (see, e.g., Fig. 10.1). The VG laser coupling that involves the momentum operator cannot be visualized in this manner and thus is less intuitive. As a another surprising result, it has been shown necessary to adjust the vector potential when modeling attosecond-pump-femtosecond-probe experiments in VG [24].

In general, observables have the same value independent of the chosen gauges as long as the TDSE is solved exactly. This follows from the fact that the different gauges are related by unitary transformations [26]. As soon as approximations are made, different gauges lead to different results. Qualitatively this difference arises from the fact that LG probes large distances, whereas VG probes regions where the wave function change rapidly with, $\boldsymbol{r}$, that is, typically positions close to the nuclei. Differences are seen for example if the calculation is carried out on too small a numerical grid or if one applies approximate schemes such as the strong-field approximation (SFA) that is described in Chapter 5.

For completeness we mention that a third form of the TDSE is often used and is known as the *acceleration gauge* or *Kramers-Henneberger frame* which is the formulation in the accelerated frame of the free electron driven by the laser field [27]. Again, the physical picture is somewhat clearer than that of VG since in this frame the initial field-free potential is simply shaking back and forth and this quivering eventually modifies the initial wave function.

2.3 Summary

In this Chapter we introduced the semi-classical theory in which the radiation field is treated classically, but the molecular field is described using quan-

tum mechanics. We wrote down the equation for the laser electric field in Coulomb gauge using the dipole approximation. Further, we presented the time-dependent Schrödinger equation for a charged particle in a laser field in both the velocity gauge and the length gauge and argued that length gauge may be the more intuitive representation.

Chapter 3

Ionization of H_2^+ in one dimension

The simplest of all molecules is the hydrogen molecular ion, H_2^+, which is composed of two protons and one electron. Understanding the behavior of H_2^+ in a strong laser field provides a basis for understanding more complex molecules. From a theoretical point of view, however, it remains a challenge to calculate ionization for even this simplest of molecules. Accordingly, despite several results on the solution of the time-dependent Schrödinger equation (TDSE) within reduced dimensionality models, the calculation of physical observables such as energy or momentum distributions has rarely been accomplished.

In this chapter, we study how the energy absorbed from an intense linearly polarized laser field at wavelengths 400 to 600 nm and intensities of the order of 10^{14} W/cm^2 is shared among the nuclei and the electron of H_2^+. We calculate the two dimensional electron-nuclei momentum distribution from a full solution of the TDSE. We use a one dimensional model with the electron and nuclear motion restricted to the electric field direction of the laser.

3.1 The one dimensional model

We consider an H_2^+ molecule in a linearly polarized laser field with the molecule aligned along the polarization axis, and we apply the method of reduced dimensionality to the H_2^+ molecular ion. The most important coordinates are the internuclear separation R and the electronic coordinate x in the direction of the laser polarization axis, measured with respect to the nuclear center-of-mass (see Fig. 3.1). In terms of these coordinates the length gauge Schrödinger equation reads

$$i\frac{\partial}{\partial t}\Psi(R,x,t) = H(t)\Psi(R,x,t) = \left[H_0 + F(t)x\right]\Psi(R,x,t), \tag{3.1}$$

where H_0 is the field-free Hamiltonian. The laser field, $F(t)$, is of the form of (2.9) with a sinusoidal envelope

$$h(t) = \sin^2(\pi t/T) \tag{3.2}$$

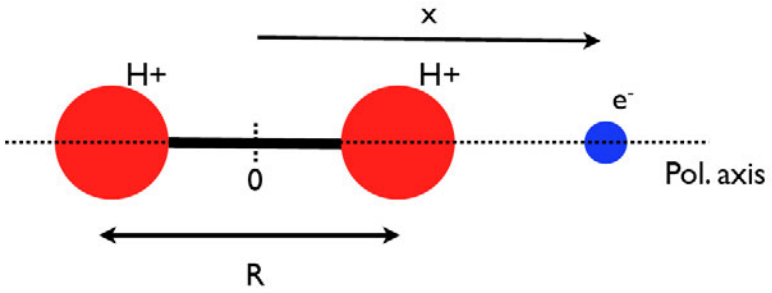

Figure 3.1: One dimensional H_2^+ model molecule where the nuclear separation, R, and the electron coordinate, x, are confined to the linear polarization axis of the laser field.

with a pulse length of $T = N \times 2\pi/\omega_0$ with N the number of cycles. Aside from being one dimensional, the field-free Hamiltonian is slightly modified compared to Eq. (2.13), as we now deal with three charged particles rather than one:

$$H_0 = -\frac{1}{m_\mathrm{p}}\frac{\partial^2}{\partial R^2} + \frac{1}{2}\frac{\partial^2}{\partial x^2} - \left\{ \frac{1}{\sqrt{(x-R/2)^2 + a(R)}} + \frac{1}{\sqrt{(x+R/2)^2 + a(R)}} \right\} + \frac{1}{R}. \tag{3.3}$$

Here, the first term is the nuclear kinetic energy, where m_p is the proton mass, the second term represents the electron kinetic energy, the third term the electron-nuclei Coulomb interaction and the last term is the Coulomb repulsion of the two protons. We model the electron-nuclei Coulomb interaction using a soft-core potential. The parameter $a(R)$ is varied with the internuclear distance to reproduce the $1\sigma_g$ Born-Oppenheimer (BO) potential curve [28–30] (cf. Fig. 3.2). Using a softcore potential avoids the numerical difficulties of a Coulomb singularity. It mimics the fact that in three dimensions the electron can bypass the nuclei.

3.2 Numerical solution of the TDSE

3.2.1 FEDVR

Any numerical solution of the TDSE must rely on an expansion of the wave functions and operators in some finite basis representation, since computers only have a finite amount of memory. Here, we use a grid representation where the fundamental element is the discretization of the variables (R, x) in coordinate space. This is accomplished by a partitioning of the R and x axes into a number of finite elements (FE's). In each FE the wave function is then expressed using a local discrete variable representation (DVR) basis. The

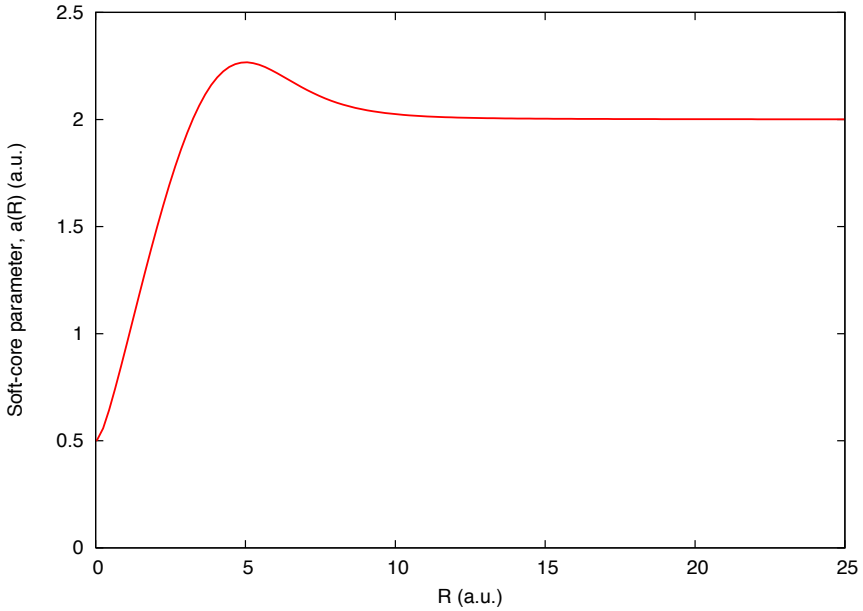

Figure 3.2: The curve shows the parameter, $a(R)$, fitted to make the model Hamiltonian given by Eq. (3.3) reproduce the $1\sigma_g$ BO potential curve of the H_2^+ molecule.

DVR gives an economical means of accurately calculating the matrix elements of various operators in this basis. In Appendix A.1 we detail how to use this so-called Finite Element Discrete Variable Representation (FEDVR) to solve the TDSE.

3.2.2 Lanczos propagator

Given an initial state $\Psi(0)$ at time $t = 0$ we may formally write the solution of the TDSE at time t as

$$\Psi(t) = U(t,0)\Psi(0) = T\exp\left(-i\int_0^t H(t')dt'\right)\Psi(0), \tag{3.4}$$

where $T\exp$ is the so-called chronological exponent which represents the evolution operator $U(t,t_0)$. For sufficiently small time intervals Δt, meaning Δt is much smaller than the time scale over which the Hamiltonian changes appreciably, it is accurate to approximate a time-dependent Hamiltonian by a series of piecewise time-independent Hamiltonians

$$H(t) \approx \begin{cases} H(\frac{\Delta t}{2}), & 0 \le t \le \Delta t \\ H(\frac{3\Delta t}{2}), & \Delta t \le t \le 2\Delta t \\ H(\frac{5\Delta t}{2}), & 2\Delta t \le t \le 3\Delta t \\ \vdots \end{cases} .$$

For each such time interval we may integrate Eq. (3.4) to get

$$\begin{aligned}\Psi(R,x,t+\Delta t) &= U(t+\Delta t,t)\Psi(R,x,t)\\ &\approx e^{-iH(t+\Delta t/2)\Delta t}\Psi(R,x,t)\end{aligned} \tag{3.5}$$

The *Lanczos algorithm* provides a unitary approximation to the evolution operator through an expansion where the full Hamiltonian is needed only for a simple matrix vector multiplication. This expansion is constructed within the so-called *Krylov subspace* with dimension K, spanned by the vectors $B_{\text{Krylov}} = \{\Psi(t), H(t+\Delta t/2)\Psi(t), \ldots, [H(t+\Delta t/2)]^{K-1}\Psi(t)\}$.

By applying the Gram-Schmidt algorithm to the basis B_{Krylov} we may derive the K-dimensional tridiagonal representation of the Hamiltonian projected onto the Krylov subspace [31]

$$H_K = \begin{pmatrix} \alpha_0 & \beta_1 & 0 & \ldots & 0 \\ \beta_1 & \ddots & & & \vdots \\ 0 & & \ddots & & 0 \\ \vdots & & & \ddots & \beta_{K-1} \\ 0 & \ldots & 0 & \beta_{K-1} & \alpha_{K-1} \end{pmatrix}. \tag{3.6}$$

Here, $\Psi_0 = \Psi(t)$, $\beta_0 = 0$ and for $j = 0, 1, \ldots$

$$\alpha_j = \langle \Psi_j | H(t+\Delta t/2) | \Psi_j \rangle, \tag{3.7}$$

$$\tilde{\Psi}_{j+1} = H(t+\Delta t/2)\Psi_j - \alpha_j \Psi_j - \beta_j \Psi_{j-1}, \tag{3.8}$$

$$\beta_{j+1} = |\tilde{\Psi}_{j+1}| \tag{3.9}$$

$$\Psi_{j+1} = \frac{\tilde{\Psi}_{j+1}}{\beta_{j+1}}. \tag{3.10}$$

The unitary propagation operator is then approximated by replacing H in Eq. (3.5) by H_K from Eq. (3.6) and this tridiagonal matrix is easily diagonalized to get the eigenvalues, λ_j, and the eigenvector matrix, $\boldsymbol{Z}$, resulting in the following expression for the propagated wave function

$$\Psi(t+\Delta t) \approx \sum_{k=0}^{K-1} a_k \Psi_k \tag{3.11}$$

where

$$a_k = \sum_{j=0}^{K-1} (\boldsymbol{Z})_{k,j} e^{-i\lambda_j \Delta t} (\boldsymbol{Z})_{0,j}. \tag{3.12}$$

The error related to the Lanczos time propagation may be estimated from

$$|\Psi_{\text{exact}}(t+\Delta t) - \Psi_{\text{Lanczos}}(t+\Delta t)| \approx \frac{(\Delta t)^K}{K!} \prod_{i=1}^{K} \beta_i \tag{3.13}$$

which is proportional to the magnitude, β_K, of the first vector outside of the Krylov basis used (cf. Eq. (3.9)). According to Eq. (3.13) convergence of the Lanczos algorithm is optimized by balancing the dimension, K, of the Krylov space and the size of the time step, Δt, used.

3.3 Energy analysis

We assume that we have obtained the time-dependent wave function after the laser pulse is over. We may then apply scattering states to investigate the correlated electron-nuclear dynamics.

We use a BO energy analysis similar to the method in Ref. [32]. The probability of observing proton and electron fragments with a relative kinetic energy E_N of the nuclei and a kinetic energy of E_e of the electron is

$$P(E_\mathrm{N}, E_\mathrm{e}) = \sum_{l=g,u} |C_l(E_\mathrm{N}, E_\mathrm{e})|^2, \tag{3.14}$$

where $l = g, u$ denotes the parity, i.e., gerade and ungerade symmetry, respectively and where $C_l(E_\mathrm{N}, E_\mathrm{e}) = \langle \psi^l_{E_\mathrm{N},E_\mathrm{e}} | \Psi(t) \rangle$ obtained numerically by evaluating the projections of the wave packet after the end of the pulse onto the outgoing continuum scattering states ($\psi^l_{E_\mathrm{N},E_\mathrm{e}}(R,x) = \psi_{E_\mathrm{N}}(R)\psi^l_{E_\mathrm{e}}(R;x)$)

$$\left[T_\mathrm{e} + V_\mathrm{N,e}(R,x)\right] \psi^l_{E_\mathrm{e}}(R;x) = E_\mathrm{e}\psi^l_{E_\mathrm{e}}(R;x), \tag{3.15}$$

$$\left[T_\mathrm{N} + \frac{1}{R}\right] \psi_{E_\mathrm{N}}(R) = E_\mathrm{N}\psi_{E_\mathrm{N}}(R). \tag{3.16}$$

To determine the continuum scattering states we use the eigenchannel R-matrix formulation described in Appendix A.2. Equation (3.15) is solved for each internuclear separation R.

The exact scattering states are eigenstates of the (total) field-free Hamiltonian and are thus orthogonal to all bound states. Hence, it is not necessary to project the bound state away from the wave function on the continuum. Further, using the eigenstates of the Hamiltonian ensures that the projections do not change in time [33]. The BO scattering states are only approximate and consequently orthogonality and time-independence are not guaranteed. However, we have checked that the projections do not change in time once the laser pulse is over.

3.4 Results and discussion

We have solved the one dimensional H_2^+ TDSE for a range of wavelengths and intensities and for a number of initial states. Figures 3.3 and 3.4 show energy spectra for H_2^+ exposed to a 400 nm laser and starting from the $\nu = 0$ and 7 initial vibrational state of the H_2^+ electronic ground state.

The two dimensional color plots in the figures show the joint energy distribution, $P(E_\mathrm{N}, E_\mathrm{e})$, of Eq. (3.14). A characteristic feature is the occurrence of

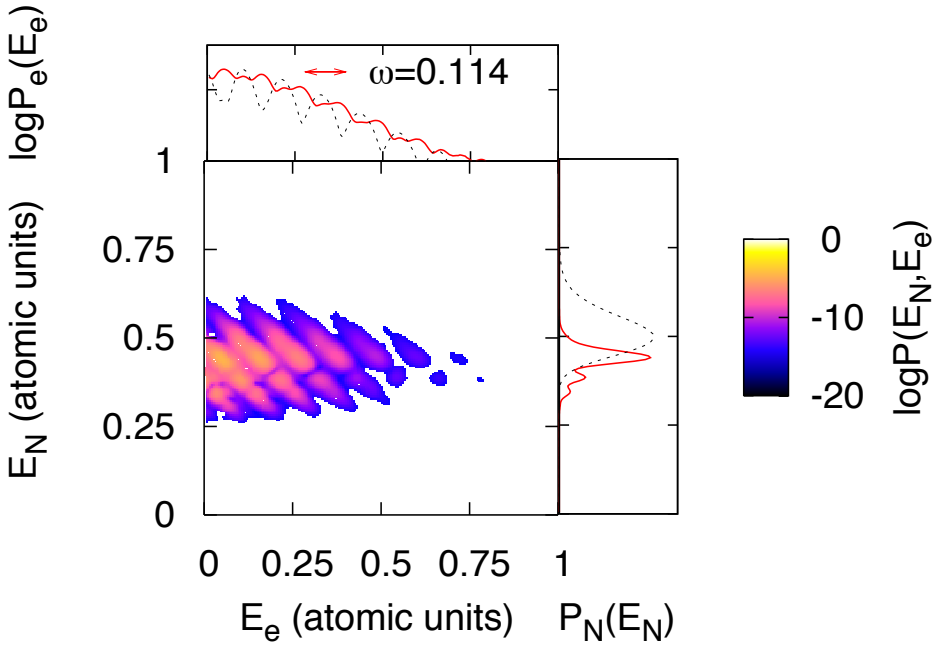

Figure 3.3: Energy analysis of dissociative ionization from H_2^+ starting from the $\nu = 0$ vibrational state. The ionizing laser has intensity 8.8×10^{13} W/cm^2, wavelength 400 nm ($\omega = 0.114$ a.u.) and consists of $N = 10$ cycles. The color plot shows the joint energy distribution calculated from Eq. (3.14) and the solid (red) curves on the side and top panels show the result of integrating the two dimensional, energy resolved probability distribution with respect to electron energy or nuclear energy, respectively. For comparison the dashed line in the side panel shows the nuclear kinetic energy release (KER) obtained using the reflection method (see text for details), and the top panel shows the ATI spectrum retrieved from a one dimensional calculation with the nuclei frozen at internuclear distance $R = 2.0$. Main features are the tilted lines with a distance corresponding to the photon energy and the shift of the energies (solid curves) compared to a frozen nuclei (dashed curves) calculation. The arrow in the top panel indicates the size of a laser photon on the energy scale. We note, in passing, the very impressive resolution provided by the FEDVR method that spans about 30 orders of magnitude.

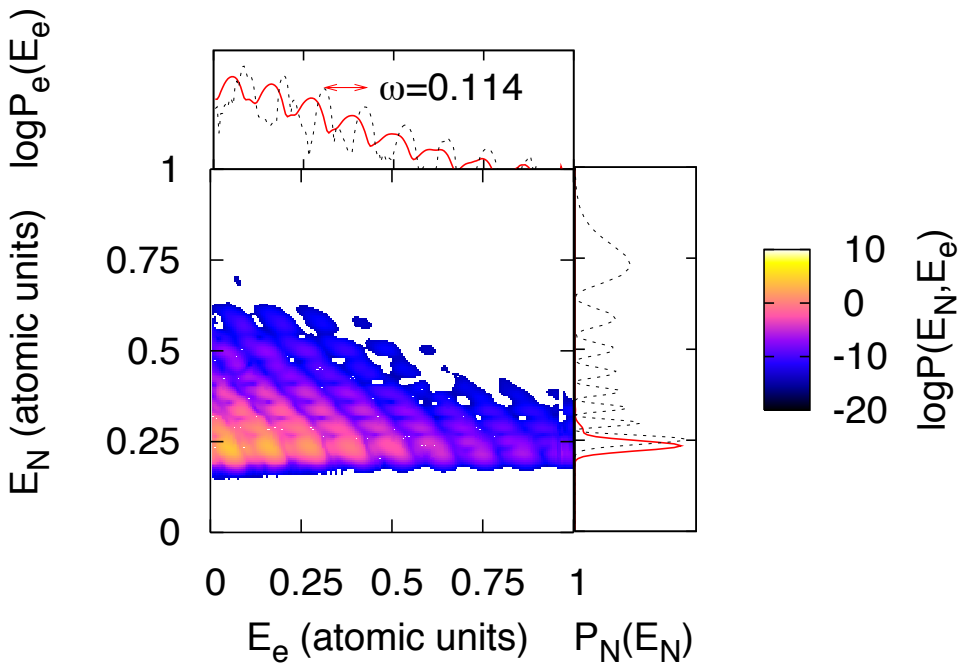

Figure 3.4: Same as Fig. 3.3, but with the initial state being the vibrational $\nu = 7$ state in the electronic ground state. The top panel is a one dimensional calculation with nuclei frozen at $R = 3.97$ which corresponds to the position of the highest density peak of the initial vibrational state. Note the horizontal lines in the joint energy distribution. These are traces of the initial vibrational state.

density lines parallel to the line $E_{\mathrm{N}} = -E_{\mathrm{e}}$. These lines are separated by the photon energy ($\omega = 0.114$ a.u.), so we ascribe them to multi-photon absorption. This has been confirmed via calculations at other wavelengths spanning over the range from 400 nm to 600 nm. The density lines, shown here, peak at a fixed nuclear KER of $E_{\mathrm{N}} = 0.44$ and 0.23 for the $\nu = 0$ and $\nu = 7$ cases, respectively independent of the electron energy. For the $\nu = 0$ calculation, we ascribe ionization enhancement to the three-photon resonance between the σ_g and σ_u BO curves. In the $\nu = 7$ case the much stronger one-photon resonance is responsible for the increased ionization around a fixed nuclear KER (see Fig. 3.5). This has been corroborated by calculations where we vary the initial state (not shown here). Focusing on initial states $\nu = 7, 8, \ldots, 11$ we observed that the ionization yields peak for the calculation using $\nu = 9$ as initial vibrational state. At the same time the position of the peaks in the nuclear KER varied only very little with the initial state. This is exactly the behavior we would expect for the stated one-photon resonance, since the probability density of the $\nu = 9$ vibrational state peaks very close to the 400 nm one-photon resonance between the σ_g and the σ_u curves (see Fig. 3.5).

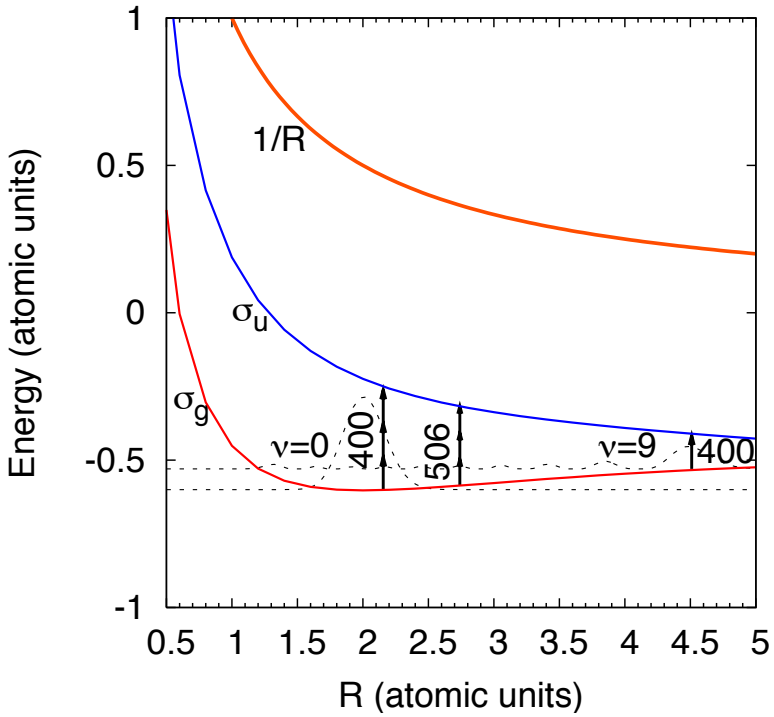

Figure 3.5: The lowest field-free Born-Oppenheimer curves σ_g and σ_u obtained with the soft-core potential of Eq. (3.3) and the Coulomb explosion curve $1/R$. The arrows indicate two three-photon resonances at wavelengths 400 and 506 nm (at $R = 2.21$ a.u. and 2.73 a.u.) and the 400 nm one-photon resonance (at $R = 4.68$ a.u.). Also, we show the $\nu = 0$ and the $\nu = 9$ vibronic ground states as they peak very close to the 400 nm three-photon and one-photon resonances. This leads to enhanced ionization of these vibrational states compared to neighboring vibrational states.

Additional horizontal lines appear in the the joint energy distribution for the $\nu = 7$ case. These lines are signatures of the the initial vibrational state. They occur due to the increased ionization from points where the initial vibrational state probability density is high. Conclusively, the joint probability distribution is characterized by the tilted multi-photon lines superimposed by horizontal weights that are the result of a product of resonances and the initial vibrational state.

The solid red lines on the side panels of Figs. 3.3 and 3.4 are obtained by integrating along lines of constant nuclear energy E_{N}. Thus, they show the distribution of the final relative kinetic energy of the nuclei after the ionization, also known as the nuclear kinetic energy release (KER). The solid (red) curves on the top panels are likewise obtained by integrating along lines of constant electron energy E_{e} and the multi-photon peaks survive and cause the well-

known above-threshold ionization (ATI) peaks corresponding to absorption of more photons than needed to bring the electron into the continuum.

For reference, we have carried out calculations with the nuclei fixed at some distance R. With no nuclear motion during the laser pulse, the electron escapes and leaves two bare protons. The protons will sequentially Coulomb explode thereby converting the initial potential energy, $1/R$, into kinetic energy of the nuclei, E_{N}. In this model, we can obtain the nuclear KER distribution by reflecting the probability density of the initial vibrational state, $\chi_i(R)$ onto the nuclear KER axis using the relation $P_N(E_N) = |\chi_i(1/E_N)|^2$. To calculate the ATI spectrum, we simply clamp the nuclei at the distance corresponding to the highest value of the probability density of the initial vibrational state and solve the one dimensional electronic TDSE. The result of the frozen nuclei approximation are shown with dashed lines in the side and top panels. The general trend is that the nuclei escapes with a higher kinetic energy than they would if nuclear motion is accounted for. Correspondingly, the ATI peaks are shifted.

Figure 3.6 displays the nuclear KER spectra obtained when the molecule starts out in the $\nu = 0$ vibronic ground state and interacts with a laser pulse of intensity 8.8×10^{13} W/cm^2. We show the KER obtained at different wavelengths. As already mentioned, we believe that the main peak in each case is due to the three-photon resonance between the σ_g and σ_u curve. Referring to Fig. 3.5 and the reflection method, we would expect the peak to be positioned $1/2.21$ a.u. $= 0.45$ a.u. in the 400 nm case to $1/2.73$ a.u. $= 0.37$ a.u. in the 506 nm case which is in good agreement with the results of Fig. 3.6 where the peaks are at 0.44 (400 nm case) and 0.377 (506 nm case). The origin of the side peaks in Fig. 3.6 is not known at the time of writing. We have carried out the energy analysis at several instants of time after the end of the pulse and arrive at the same result. Thus, the peaks are not due to inadequacy of the approximate BO scattering states employed for the energy analysis.

Next, we look at how the ionization fragments, i.e., the nuclei and the electron, share the absorbed laser field energy. We show that for a given number of photons absorbed by the system there is a finite probability that the nuclei take most of the energy leaving an electron behind almost at rest ($E_{\mathrm{e}} \sim 0$). This is surprising since only the electron couples directly to the field (Eq. (3.1)) and all nuclear dynamics must be mediated through electronic transitions. In other words this process requires a high correlation between the electron and nuclear dynamics. We believe that the observed correlation makes the system a valuable supplement to the thoroughly studied case of double ionization of helium where the two correlated particles are identical electrons that both couple directly to the laser field [34].

In the typical experiment the initial state is not one specific vibrational state. Instead, H_2^+ has been prepared from H_2 by, for instance, electron impact ionization. In this case, we start out with an incoherent mixture of vibrational states (see also Chapter 4). The population of each vibrational state corresponds to the Franck-Condon (FC) factor, i.e., the norm squared projection of the ground H_2 ground vibrational state onto each vibrational state of the

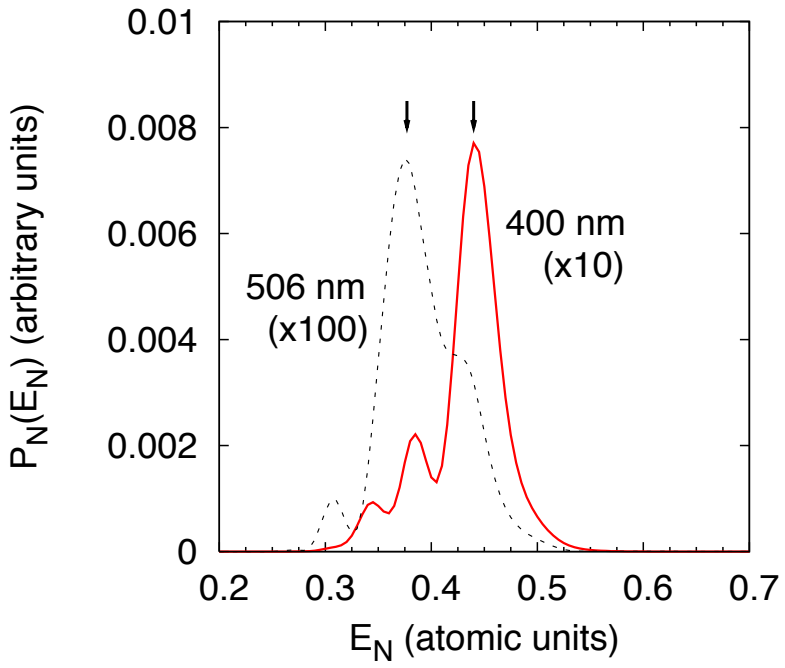

Figure 3.6: Nuclear KER spectra obtained for a 10 cycle, 8.8×10^{13} W/cm^2 laser at wavelengths at 400 nm (solid curve) and 506 nm (dashed curve) starting from the $\nu = 0$ vibrational state of the electronic ground state. The arrows indicates peaks that we ascribe to a three-photon resonance between the σ_g and the σ_u curve (cf. Fig. 3.5). For the sake of clarity the amplitudes have been multiplied with a factor of 10 and 100 as indicated.

H_2^+ ion. Figure 3.7 shows the energy resolved spectrum averaged according to an FC distribution. The multi-photon peaks in the joint energy distribution survive the averaging, whereas the traces of the initial wave function wash out. Also, the ATI spectrum survives the averaging, but there is no structure in the nuclear KER spectrum.

We mention for completeness that in a real experiment the averaging over varying intensities (see Chapter 9) further blurs the spectrum. However, this averaging simply means that calculations at lower intensities, where the multi-photon peaks are narrower and less intense, will be added to the result displayed in Fig. 3.7. We do not expect that this procedure will suppress the multi-photon structure. As such the joint energy distribution in Fig. 3.7 serve as a great motivation for future experiments where the ionized electron and the nuclear fragments are measured in coincidence.

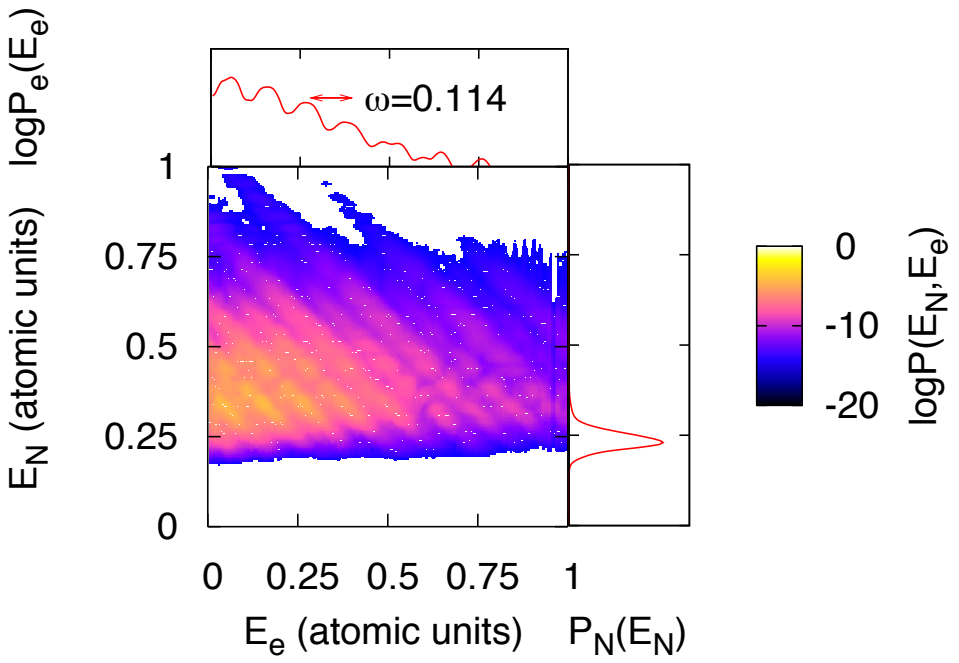

Figure 3.7: Same as Fig. 3.3, but FC averaged including the vibrational states $\nu = 0$ through $\nu = 13$. This is comparable to an experimental situation, and we see that the multi-photon structure survives in the two dimensional, joint energy distribution. Also, ATI peaks survives (top panel) whereas the structure of the nuclear KER is washed out (side panel).

3.5 Summary

We have solved the time-dependent Schrödinger equation for the H_2^+ molecule in a linearly polarized laser field. We used a reduced dimensionality model, where we restricted dynamics to the direction of the laser polarization. We carried out an energy analysis to map the energy sharing of the absorbed laser photons among the ionizing electron and the dissociating nuclei. The appearance of structures corresponding to multi-photon absorption structures was observed. These structures survive if we integrate out the nuclear energy dependence, and we see no multi-photon structure if we integrate out the electron energy. Further, there is, surprisingly, a finite probability that the nuclei take most of the energy leaving an electron behind almost at rest.

Chapter 4

HHG and ionization

In the previous chapter we looked at a full solution of the time-dependent Schrödinger equation (TDSE) within a one dimensional model for an H_2^+ molecule in a laser field, and we saw how the ionization signal was calculated. For other, more complex molecules, both the solution of the TDSE and the analysis of the solution becomes much more difficult.

The durations of intense laser fields are short, typically on the order of femtoseconds. This is comparable to the vibrational period in light molecules, so one commonly used approximation to facilitate numerics is to consider the nuclei as fixed or only restricted to vibrate, not rotate. In the current chapter we show how this type of approximation may be used to evaluate high-order harmonic generation (HHG) and ionization, but we begin with an introduction to HHG.

4.1 An introduction to HHG

The exploitation of nonlinear media for second harmonic generation, i.e., frequency doubling of laser radiation, is essentially as old as the operating laser itself. The availability of femtosecond lasers in the late 80s with intensities typically between 10^{14} and 10^{15} W/cm^2 led to the observation of a new type of frequency conversion known as HHG [35]. Simply put, a gas of atoms exposed to such fields emits not only second or third order harmonics, but coherent radiation at high-order harmonics of the laser frequency with an almost constant efficiency up to some cutoff.

A general understanding of HHG is gained from the *three-step model* [36] which is illustrated in Fig. 4.1 for the hydrogen atom. We arrive at the three-step model by combining the length gauge TDSE (Eq. (2.13)) with the assumption that it is valid to describe the laser atom interaction in terms of an instantaneous electric field (a quasi-static assumption). In this picture, the Coulomb potential is distorted at each time by the instantaneous laser electric field. Given that the change of the electric field is slow compared to the bound-state electronic motion, the electron wave function has time to tunnel through the barrier (step 1). After this *tunnel ionization*, the electron

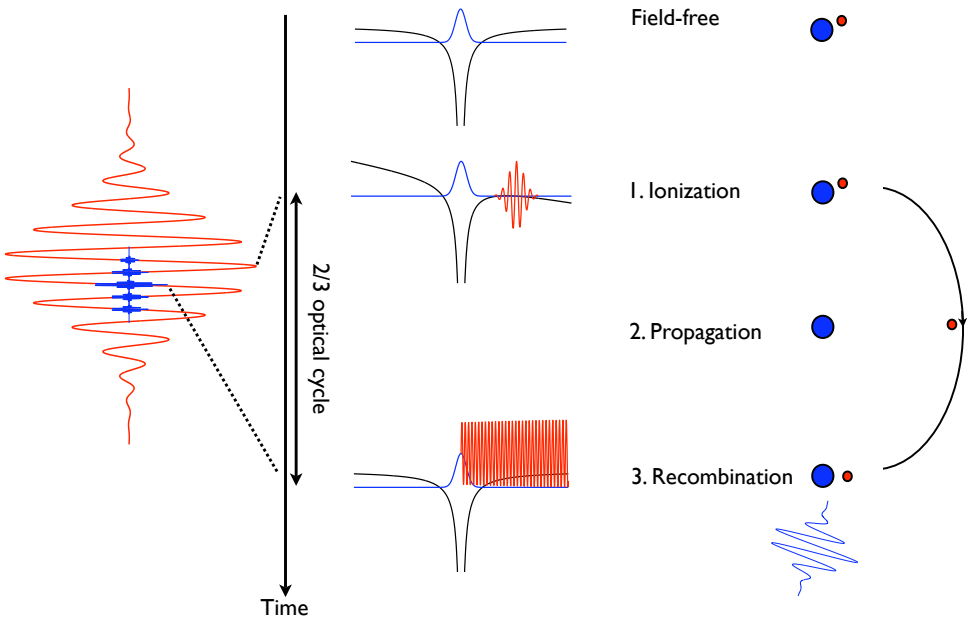

Figure 4.1: Illustration of the three-step model for HHG. Time progresses from top to bottom. Leftmost, the red curve illustrates the laser field and the blue curve, the corresponding high-order harmonic (attosecond) pulse. The middle panel shows the potential and the wave function as a function of time, which is also displayed in the simplified particle picture on the right. The three steps that lead to high-order harmonic generation are: 1. Ionization where part of the electron wave function tunnels due to the laser field distortion of the potential curve. 2. Acceleration of the electron accompanied by a transverse spread of the wave function. 3. Recombination of the continuum electron with the initial state via the laser field accompanied by the emission of a high-order harmonic photon. The three steps take place within two thirds of an optical cycle.

experiences a *propagation*, strongly accelerated by the laser field with little influence from the Coulomb potential. Due to the oscillation of the laser field, the electron is first driven away from the cation, but later accelerated back towards the nucleus (step 2). Finally, about two thirds of an optical cycle after ionization, the electron *recombines* and the energy accumulated by the electron is released as a high-order harmonic photon (step 3). Molecules exhibit the same kind of behavior. In this case, however, nuclear structure and dynamics will affect the radiative response.

The observable in HHG is the frequency-dependent emitted intensity of the radiation, $S(\omega)$. For a large gas of uncorrelated emitting molecules [37]

$S(\omega)$ can be found through the expectation value of the velocity $\langle \boldsymbol{v}(t) \rangle$ [38]

$$S(\omega) = \left(\frac{1}{\omega T} \left| \int_0^T dt\, e^{-i\omega t} \langle \boldsymbol{v}(t) \rangle \right| \right)^2 , \tag{4.1}$$

where the laser field driving the process is non-zero only in the time interval $[0, T]$. Here, $\boldsymbol{v}$ should in principle be the velocity operator of all nuclei and electrons. However, as a result of its much smaller mass, the electron is accelerated to much greater velocities by the laser field. Consequently, HHG is vastly dominated by the electrons' contribution, i.e., $\boldsymbol{v} \simeq -i \sum_n \boldsymbol{\nabla}_{\boldsymbol{r}_n}$ with $\boldsymbol{r}_n$ denoting the coordinates of the nth electron.

In principle, the radiation emitted from one molecule has to propagate through the gas of the remaining molecules and thus the effect of propagation of the laser field and the harmonics through the generating medium should be included [39]. Understanding the single-molecule response is, nonetheless, a prerequisite for understanding the more complex situation involving all of the molecules.

4.2 Influence of nuclear degrees of freedom on HHG

Evaluation of the dipole velocity of Eq. (4.1) is non-trivial, but as stated in the introduction to this chapter, the order of magnitude in time difference between laser field duration and the timescale of nuclear motion of molecules, implies that we can neglect some or all nuclear motion. However, with this elimination comes a caveat. Specifically, how to correctly eliminate the rotational degree of freedom. Say that we have a collection of molecules in an incoherent mixture as will be the case unless the molecules have been identically prepared by, e.g., a laser. Then the initial system cannot simply be described by a single wave function, but rather we deal with a collection of wave functions with no relative phase information. In other words, we loose interference. Imagine now that our mixed state of molecules is exposed to an intense laser pulse leading to HHG in the molecules while the nuclei are essentially stationary. One is tempted to think that the total signal from a incoherent mixture is simply calculated by adding the harmonic intensities calculated at different orientations as has been done previously in literature, see, e.g., [40–42]. However, the electric fields, not the intensities, of molecules with different nuclear coordinates should be added and then squared to find the intensity. This implies that there will be interference in the intensity signal from the squaring of the total electric field summed over each of the differently oriented molecules.

Let us turn to a formal treatment of the concepts discussed above. The characteristic incoherent mixture in an experiment consists of a thermal ensemble at some temperature T. Here, the energy eigenstate $\psi_{\boldsymbol{\alpha}}$ with energy $E_{\boldsymbol{\alpha}}$ is initially, at time $t = 0$, represented with the Boltzmann weight $P_{\boldsymbol{\alpha}} = \exp(-E_{\boldsymbol{\alpha}}/k_B T)/Z$, with partition function $Z = \sum_{\boldsymbol{\alpha}} \exp(-E_{\boldsymbol{\alpha}}/k_B T)$].

The rovibronic label $\boldsymbol{\alpha} = (\xi, \boldsymbol{v}, \boldsymbol{n})$ denotes the state of the molecule through electronic ξ, vibrational $\boldsymbol{v}$ and rotational $\boldsymbol{n}$ indices and k_B is Boltzmann's constant. This type of mixed state can be handled formally using the density operator [43]

$$\rho(0) = \sum_{\boldsymbol{\alpha}} P_{\boldsymbol{\alpha}} |\psi_{\boldsymbol{\alpha}}(0)\rangle\langle\psi_{\boldsymbol{\alpha}}(0)|. \tag{4.2}$$

The system is now excited and propagated to time t and we express this in terms of the evolution operator $U(t,0)$ so that $|\Psi_{\boldsymbol{\alpha}}(t)\rangle = U(t,0)|\psi_{\boldsymbol{\alpha}}(0)\rangle$, and

$$\rho(t) = \sum_{\boldsymbol{\alpha}} P_{\boldsymbol{\alpha}} |\Psi_{\boldsymbol{\alpha}}(t)\rangle\langle\Psi_{\boldsymbol{\alpha}}(t)|. \tag{4.3}$$

In this development we can find the expectation value of the time-dependent velocity operator (or any other operator), entering Eq. (4.1) for the HHG yield, by tracing the product of the density matrix with the operator

$$\begin{aligned} \boldsymbol{v}(t) &= \text{Trace}\left[\rho(t)\boldsymbol{v}\right] = \sum_{\boldsymbol{\alpha}} P_{\boldsymbol{\alpha}} \langle\Psi_{\boldsymbol{\alpha}}(t)|\boldsymbol{v}|\Psi_{\boldsymbol{\alpha}}(t)\rangle \\ &= \sum_{\boldsymbol{\alpha}} P_{\boldsymbol{\alpha}} \int d\Omega d\boldsymbol{R} d\boldsymbol{r}\; \Psi^*_{\boldsymbol{\alpha}}(\Omega, \boldsymbol{R}, \boldsymbol{r}, t)(-i\boldsymbol{\nabla}_{\boldsymbol{r}})\Psi_{\boldsymbol{\alpha}}(\Omega, \boldsymbol{R}, \boldsymbol{r}, t), \end{aligned} \tag{4.4}$$

where Ω represents all rotational angles, $\boldsymbol{R}$ denotes all the vibrational coordinates and $\boldsymbol{r}$ represents all of the electrons' positions. According to Eq. (4.1), we note that one can observe interferences in the intensity $S(\omega)$ from incoherent rovibronic ($\boldsymbol{\alpha}$) states.

In most HHG calculations, the Born Oppenheimer (BO) approximation is applied to separate out the relatively slow rotational motion of the nuclei

$$\Psi_{\boldsymbol{\alpha}}(\Omega, \boldsymbol{R}, \boldsymbol{r}, t) \approx \phi_{\boldsymbol{\alpha}}(\Omega, t)\psi_{\boldsymbol{\alpha}}(\Omega; \boldsymbol{R}, \boldsymbol{r}, t), \tag{4.5}$$

where $\phi_{\boldsymbol{\alpha}}(\Omega, t)$ is the rotational part of the wave function, and $\psi_{\boldsymbol{\alpha}}(\Omega; \boldsymbol{R}, \boldsymbol{r}, t)$ is the vibronic wave function for fixed rotational coordinates. This separation much eases calculations of rotational excitations with non-ionizing pump laser pulses that causes alignment (see Chapter 8). Further, the rotational motion of the nuclei can effectively be considered fixed during the interaction with the intense laser pulse that produces HHG. This allows us to propagate the vibronic part $\psi_{\boldsymbol{\alpha}}(\Omega; \boldsymbol{R}, \boldsymbol{r}, t)$ of the state in the strong laser field, while keeping the rotational coordinates fixed. These points taken into account, the dipole velocity is well approximated by

$$\boldsymbol{v}(t) \approx \sum_{\boldsymbol{\alpha}} P_{\boldsymbol{\alpha}} |\phi_{\boldsymbol{\alpha}}(\Omega, \bar{t})|^2 \int d\boldsymbol{R} d\boldsymbol{r} \psi^*_{\boldsymbol{\alpha}}(\Omega; \boldsymbol{R}, \boldsymbol{r}, t)(-i\boldsymbol{\nabla}_{\boldsymbol{r}})\psi_{\boldsymbol{\alpha}}(\Omega; \boldsymbol{R}, \boldsymbol{r}, t). \tag{4.6}$$

Here $\bar{t}$ is some time in the interval where the HHG driving pulse is non-zero.

For molecules with vibrational frequencies much smaller than the inverse duration of the laser pulse causing HHG, the vibrational coordinates can also generally be treated as fixed (see Chapter 7). We then additionally separate out the vibrational part of the vibronic wave function $\psi_{\boldsymbol{\alpha}}(\Omega; \boldsymbol{R}, \boldsymbol{r}, t) \approx$

$\psi'_\xi(\Omega, \boldsymbol{R}; \boldsymbol{r}, t))\chi_{\boldsymbol{\alpha}}(\boldsymbol{R}, t)$ and arrive at an expression for the dipole velocity with clamped nuclei

$$\boldsymbol{v}(t) \approx \sum_{\boldsymbol{\alpha}} P_{\boldsymbol{\alpha}} |\phi_{\boldsymbol{\alpha}}(\Omega, \bar{t})|^2 \int d\boldsymbol{R} |\chi_{\boldsymbol{\alpha}}(\boldsymbol{R}, \bar{t})|^2 \times \int d\boldsymbol{r} \psi'^{*}_{\xi}(\Omega, \boldsymbol{R}; \boldsymbol{r}, t)(-i\boldsymbol{\nabla}_{\boldsymbol{r}})\psi'_\xi(\Omega, \boldsymbol{R}; \boldsymbol{r}, t). \tag{4.7}$$

Equations. (4.6) and (4.7) are relevant because the propagation during the short HHG driving pulse is immensely more manageable when the dimensionality is reduced. The ro-vibrational part $|\phi_{\boldsymbol{\alpha}}(\Omega, \bar{t}|^2 |\chi_{\boldsymbol{\alpha}}(\boldsymbol{R}, \bar{t})|^2$ weighs the HHG contribution to the electric field from all the orientations and vibrational distances of the molecule that was initially in the state $\boldsymbol{\alpha}$. Since these functions vary slowly with t compared to the electronic part during the short pulse, these functions can be taken to be time-independent during this interaction.

The effect of vibrational motion is usually of much smaller consequence than the rotational (see Chapter 7) and one may safely set $\boldsymbol{R} = \boldsymbol{R}_0$, the equilibrium bond distance corresponding to the initial vibrational state $\boldsymbol{\nu}$.

4.3 Influence of nuclear degrees of freedom on ionization

We now turn our attention to ionization. In the typical experiment the electron momentum distribution is observed, which lets us reconstruct $W(\boldsymbol{p})$, the probability of measuring an electron with asymptotic, field free momentum $\boldsymbol{p}$. This yields information about the behavior of the electron in the asymptotic region of the detector far from the residual cation, but we do not learn about its wave function close to the nuclei. The quantity $W(\boldsymbol{p})$ is the expectation value of the projection operator $|\psi_{\boldsymbol{p}}\rangle\langle\psi_{\boldsymbol{p}}| \otimes I_{\Omega,\boldsymbol{R}}$, where $\psi_{\boldsymbol{p}}$ is the exact field-free continuum eigenstate in the asymptotic region with momentum $\boldsymbol{p}$, and $I_{\Omega,\boldsymbol{R}}$ is an identity operator working on the nuclear coordinates only. Finding the expectation value of this operator in the state $\rho(t)$ from Eq. (4.3) gives us:

$$W(\boldsymbol{p}) = \text{Trace}[\rho(t)|\psi_{\boldsymbol{p}}\rangle\langle\psi_{\boldsymbol{p}}| \otimes I_{\Omega,\boldsymbol{R}}] = \sum_{\boldsymbol{\alpha}} P_{\boldsymbol{\alpha}} \langle\Psi_{\boldsymbol{\alpha}}(t)|\psi_{\boldsymbol{p}}\rangle\langle\psi_{\boldsymbol{p}}|\Psi_{\boldsymbol{\alpha}}(t)\rangle$$
$$= \sum_{\boldsymbol{\alpha}} P_{\boldsymbol{\alpha}} \int d\Omega d\boldsymbol{R} \left| \int d\boldsymbol{r} \psi^*_{\boldsymbol{p}}(\boldsymbol{r}) \Psi_{\boldsymbol{\alpha}}(\Omega, \boldsymbol{R}, \boldsymbol{r}, t) \right|^2 . \tag{4.8}$$

Here t is any time after the ionization pulse has ended, since projecting on $\psi_{\boldsymbol{p}}$ at any later time yields the same result (see also Chapter 3). It is important to note here that the experimental observable $W(\boldsymbol{p})$ only contains information about the asymptotic momentum distribution of the electron. In particular, no information is retrieved about the nuclei in contrast to the case of the coincidence measurements of electrons and protons from Chapter 3. Still, the state $\psi_{\boldsymbol{p}}$ entering the projection operator above corresponds to the exact

continuum state in all space for the given fixed nuclear coordinates $(\Omega, \boldsymbol{R})$. The theoretical calculation can be made to agree by propagating the solution to large times until the wave function is far away from the parent ion. Then, a suitable region around the parent ion is removed and the remaining part of the electronic wave function is projected on exact momentum eigenstates [33].

We will again use the BO approximation to separate out the rotational part of the excited state $\Psi_{\boldsymbol{\alpha}}(\Omega, \boldsymbol{R}, \boldsymbol{r}, t) \approx \psi_{\boldsymbol{\alpha}}(\Omega; \boldsymbol{R}, \boldsymbol{r}, t)\phi_{\boldsymbol{\alpha}}(\Omega, t)$. Invoking once more the argument that $\phi_{\boldsymbol{\alpha}}(\Omega, t)$ changes only very slowly on the time scale of interest (the pulse duration of the ionizing laser) $\psi_{\boldsymbol{\alpha}}(\Omega; \boldsymbol{R}, \boldsymbol{r}, t)$ is propagated using fixed Ω

$$W(\boldsymbol{p}) \approx \sum_{\boldsymbol{\alpha}} P_{\boldsymbol{\alpha}} \int d\Omega |\phi_{\boldsymbol{\alpha}}(\Omega, \bar{t})|^2 \int d\boldsymbol{R} \left| \int d\boldsymbol{r} \psi^*_{\boldsymbol{p}}(\boldsymbol{r}) \Psi_{\boldsymbol{\alpha}}(\Omega; \boldsymbol{R}, \boldsymbol{r}, t) \right|^2 . \quad (4.9)$$

Further, if we can separate out the vibrational motion, then we can write $\psi_{\boldsymbol{\alpha}}(\Omega; \boldsymbol{r}, \boldsymbol{R}, t) = \psi'_{\boldsymbol{\alpha}}(\Omega, \boldsymbol{R}; \boldsymbol{r}, t)\chi_{\boldsymbol{\alpha}}(\boldsymbol{R}, t)$ and

$$\begin{aligned} W(\boldsymbol{p}) \approx \sum_{\boldsymbol{\alpha}} P_{\boldsymbol{\alpha}} \int d\Omega |\phi_{\boldsymbol{\alpha}}(\Omega, \bar{t})|^2 \int d\boldsymbol{R} |\chi_{\boldsymbol{\alpha}}(\boldsymbol{R}, \bar{t})|^2 \\ \times \left| \int d\boldsymbol{r} \psi^*_{\boldsymbol{p}}(\boldsymbol{r}) \psi'_{\xi}(\Omega, \boldsymbol{R}; \boldsymbol{r}, t) \right|^2 . \end{aligned} \quad (4.10)$$

This may be simplified even more by putting $\boldsymbol{R} = \boldsymbol{R}_0$ as discussed in the case of HHG in the previous section.

To consider the nuclei fixed while the electron propagates to the detector is certainly not literally true, since the time it takes an electron to reach a detector at a macroscopic distance is certainly much greater than any rotational or vibrational period of the molecule. However, the time it takes the electron to propagate many atomic diameters away from the molecule is small compared to rotational and, often, vibrational periods. Thus, the nuclei are approximately fixed during the time where the electron is close enough to the molecule to experience complicated interactions. Conversely, at the times after ionization where the nuclei have moved appreciably, the electron is so far away that only the Coulombic monopole terms have an effect [33]. It is in this sense that the nuclei can be considered fixed.

Different nuclear configurations are distinguishable, and we get quantum mechanical interference from neither pure nor mixed states. Only the distribution of internuclear distances and angles play a role. Looking at the Eqs. (4.9) and (4.10) we see exactly the same structure as in the HHG Eqs. (4.6) and (4.7): The contribution to the signal from molecules initially in the state $\boldsymbol{\alpha}$ is the integral of contributions $|\int d\boldsymbol{r} \psi^*_{\boldsymbol{p}}(\boldsymbol{r}) \psi'_{\xi}(\Omega, \boldsymbol{R}; \boldsymbol{r}, t)|^2$ from all different configurations of the nuclear coordinates weighed by the probability density $|\phi_{\boldsymbol{\alpha}}(\Omega, \bar{t})|^2 |\chi_{\boldsymbol{\alpha}}(\boldsymbol{R}, \bar{t})|^2$ of finding this nuclear configuration. The similarity comes naturally because we in both cases used the approximation of fixed nuclear coordinates and measured on the state of electrons only.

4.4 Summary

An introduction to the high-order harmonic generation has been given in this chapter via the three-step model. Next, we saw how the numerically demanding task of calculating harmonic yields from molecules is facilitated by invoking the Born-Oppenheimer approximation and treating the nuclei as partly or completely frozen during the interaction with the short pulse that generates the harmonics. Likewise, we discussed how to calculate ionization when nuclear motion can be partly or completely disregarded.

Chapter 5

HHG and ionization in the strong-field approximation

In this chapter we introduce the strong-field approximation (SFA) and implement it to calculate of high-order harmonic generation (HHG) and ionization. Two basic assumptions go into the SFA: (i) The electron is unaffected by the laser field until the time of ionization. (ii) The ionized electron is unaffected by the attractive potential of the residual cation. Further, we neglect the depletion of the bound state [44]. We detail how to evaluate the HHG using the Lewenstein model or the Kuchiev-Ostrovsky model.

5.1 Introduction to the SFA

To present a formal development of the SFA we start from the Dyson equation for the evolution operator:

$$U(t,t') = U_0(t,t') - i\int_{t'}^{t} dt'' U(t,t'') V_{\text{Laser}}(t'') U_0(t'',t'). \tag{5.1}$$

Here, U_0 stands for the evolution operator associated with the field-free Hamiltonian, H_0, and V_{Laser} denotes the time-dependent terms describing the laser interaction with the charged particle(s) in velocity or length gauge (cf. Eqs. (2.11) and (2.13)). Following the approximations outlined in Chapter 4, we apply the Born-Oppenheimer (BO) approximation and consider the orientation as fixed during the short high-harmonic generating femtosecond pulse. Also, assuming negligible electron-electron correlation, the electrons are put into orbitals obtained from Hartree-Fock calculations. We freeze all orbitals except the highest occupied molecular orbital (HOMO). This approach is motivated by the three-step model for high-order harmonic generation and the fact that the ionization of electrons in lower orbitals is exponentially suppressed, because the rate of tunnel ionization depends exponentially on the ionization potential. This is known as the *single active electron* (SAE) approximation. With these approximations in place, we go on with the SFA and estimate the

solution by replacing the full evolution operator U on the right hand side of Eq. (5.1) by the *Volkov propagator* U_{V}, i.e.,

$$U(t,t') \approx U_0(t,t') - i\int_{t'}^{t} dt'' U_{\mathrm{V}}(t,t'') V_{\mathrm{Laser}}(t'') U_0(t'',t'). \tag{5.2}$$

The molecular wave function on which this approximate evolution operator acts is the molecular orbital of the active electron $\psi_0(\boldsymbol{r})\exp(iI_p t)$, evaluated at the nuclear equilibrium configuration, $\boldsymbol{R}_0$, at fixed orientation Ω where I_p is the adiabatic ionization potential of the molecule, multiplied by the ground vibrational state of the neutral molecule, $\chi_{i,0}(\boldsymbol{R})$. The Volkov propagator is composed of the product of a Volkov wave, $\psi^{\mathrm{V}}_{\boldsymbol{p}}(\boldsymbol{r},t)$, and the $\boldsymbol{\nu}$th vibrational state of the molecular ion, $\chi_{f,\boldsymbol{\nu}}(\boldsymbol{R})$ (see also Appendix B). In length gauge, which we shall use below, the Volkov wave is given by

$$\psi^{\mathrm{V}}_{\boldsymbol{p}}(\boldsymbol{r},t) = (2\pi)^{-3/2}\exp\left\{ i\left[(\boldsymbol{p}+\boldsymbol{A}(t))\cdot\boldsymbol{r} - \int^{t} dt' \frac{(\boldsymbol{p}+\boldsymbol{A}(t'))^2}{2}\right]\right\} \tag{5.3}$$

and for the propagator we have

$$U_{\mathrm{V}}(t,t') = \int d\boldsymbol{p} \sum_{\boldsymbol{\nu}} |\psi^{\mathrm{V}}_{\boldsymbol{p}}(t)\chi_{f,\boldsymbol{\nu}}(t)\rangle\langle\psi^{\mathrm{V}}_{\boldsymbol{p}}(t')\chi_{f,\boldsymbol{\nu}}(t')|. \tag{5.4}$$

Finally, assuming that the field is turned on at time $t = 0$, we have

$$\begin{aligned} |\Psi(t)\rangle = U(t,0)|\Psi_0\chi_{i,0}(0)\rangle &= |\Psi_0\chi_{i,0}(t)\rangle \\ &- i\int_0^t dt' \int d\boldsymbol{p} \sum_{\boldsymbol{\nu}} |\psi^{\mathrm{V}}_{\boldsymbol{p}}(t)\chi_{f,\boldsymbol{\nu}}(t)\rangle \\ &\times \langle\psi^{\mathrm{V}}_{\boldsymbol{p}}(t')\chi_{f,\boldsymbol{\nu}}(t')|V_{\mathrm{Laser}}(t')|\psi_0(t')\chi_{i,0}(t')\rangle. \end{aligned} \tag{5.5}$$

To conclude, we discuss the limitations of the SFA. The model neglects bound-bound dynamics which play a significant role for low energy electrons. Also, such electrons feel the influence of the binding potential more than high-energy electrons. As such the SFA represents the low energy parts of spectra poorly. Additionally, neglecting the Coulomb potential leads to an erroneous value for the phase of the continuum electron. This error is carried over to the estimated phase of the harmonics. We will return to these points in Chapters 6 and 9.

5.2 The Lewenstein model for HHG

It follows from Eq. (4.1) that in order to calculate HHG the fundamental numerical consists of the the evaluation of the dipole velocity. To achieve this, we combine Eqs. (5.5) and (4.7) and include only bound-continuum transitions.

Thus, we arrive at

$$\begin{aligned}\langle \boldsymbol{v}(t)\rangle = i\int_0^t dt'\, C(t-t')F(t') \\ \times \int d\boldsymbol{p}\, \boldsymbol{v}^*_{\rm rec}(\boldsymbol{p}+\boldsymbol{A}(t)) d_{\rm ion}(\boldsymbol{p}+\boldsymbol{A}(t')) e^{-iS_{\boldsymbol{p}}(t,t')} \\ + c.c..\end{aligned} \tag{5.6}$$

In this equation

$$C(t-t') = \sum_{\boldsymbol{\nu}} \exp\left[-i\epsilon_{\boldsymbol{\nu}}(t-t')\right] |\langle \chi_{f,\boldsymbol{\nu}}|\chi_{i,0}\rangle|^2 \tag{5.7}$$

is the vibrational autocorrelation function and is given in terms of Franck-Condon (FC) factors $|\langle \chi_{f,\boldsymbol{\nu}}|\chi_{i,0}\rangle|^2$ and $\epsilon_{\boldsymbol{\nu}}$ the vibrational energy. Further,

$$\begin{aligned}\boldsymbol{v}_{\rm rec}(\boldsymbol{p}) &= \boldsymbol{p}(2\pi)^{-3/2}\int d\boldsymbol{r}\exp[-i\boldsymbol{p}\cdot\boldsymbol{r}]\psi_0(\boldsymbol{r}) \\ &\equiv \boldsymbol{p}\phi_0(\boldsymbol{p}), \end{aligned} \tag{5.8}$$

$$\begin{aligned} d_{\rm ion}(\boldsymbol{p}) &= \boldsymbol{e}\cdot(2\pi)^{-3/2}\int d\boldsymbol{r}\exp[-i\boldsymbol{p}\cdot\boldsymbol{r}]\boldsymbol{r}\psi_0(\boldsymbol{r}) \\ &= i\boldsymbol{e}\cdot\boldsymbol{\nabla}_{\boldsymbol{p}}\phi_0(\boldsymbol{p}), \end{aligned} \tag{5.9}$$

$$S_{\boldsymbol{p}}(t,t') = \int_{t'}^t dt''[(\boldsymbol{p}+\boldsymbol{A}(t''))^2/2 + I_p]. \tag{5.10}$$

The electronic part of Eq. (5.6) has appeared many times since the seminal paper of Lewenstein et al. [44] and clearly points out the three essential steps of HHG process: The electron ionizes to the continuum at time t' with probability amplitude $F(t')d_{\rm ion}(\boldsymbol{p}+\boldsymbol{A}(t'))$. It then propagates in the field until time t acquiring a phase factor $S_{\boldsymbol{p}}(t,t')$ and recombines with a probability amplitude $\boldsymbol{v}^*_{\rm rec}(\boldsymbol{p}+\boldsymbol{A}(t))$. Due to vibration this product of amplitudes is weighted by a nuclear factor $C(t-t')$ [45].

5.2.1 The molecular orbital in a Gaussian basis

To evaluate the electronic part of Eq. (5.6) we write the molecular orbital of the active electron in the molecular fixed (MF) frame, a coordinate system fixed to the molecule, as a linear combination of Gaussian orbitals

$$\psi_0^{\rm MF}(\boldsymbol{r}) = \sum_{n,i_x,i_y,i_z,m} N^n_{i_x,i_y,i_z,m}(x-R^n_x)^{i_x}(y-R^n_y)^{i_y}(z-R^n_z)^{i_z}e^{-\alpha_m(\boldsymbol{r}-\boldsymbol{R}^n)^2}. \tag{5.11}$$

Here, $\boldsymbol{R}^n = (R^n_x, R^n_y, R^n_z)$ denotes the coordinates of atom n. $N^n_{i,j,k,m}$ and α_m are expansion coefficients that we find using the GAMESS quantum chemistry code [46].

5.2.2 Evaluation of the momentum integral

The integration over the electron momenta in Eq. (5.6) is one of the main challenges of evaluating the Lewenstein model. The current expansion of the molecular orbitals in terms centered on the atoms allows us to evaluate the momentum integral of Eq. (5.6) using the improved stationary phase method [7, 47, 48]. In this approach, the electron does not simply escape and return to the center of mass of the molecule. Instead, the multi-center structure of the molecule is taken into account by including electron trajectories from one atom to another. The momentum space wave function of Eq. (5.11) which enters Eq. (5.6) may be calculated analytically. Using Eq. (3.462,2) from Ref. [49], we have

$$\phi_0^{\mathrm{MF}}(\boldsymbol{p}) = \sum_n e^{-i\boldsymbol{p}\cdot\boldsymbol{R}^n} f_n(\boldsymbol{p}), \tag{5.12}$$

$$\begin{aligned} f_n(\boldsymbol{p}) = &\sum_{i_x,i_y,i_z,m} (2\alpha_m)^{-3/2} N^n_{i_x,i_y,i_z,m} e^{-\frac{\boldsymbol{p}^2}{4\alpha_m}} \\ &\times \prod_{l=1}^{3} i_l! \left(\frac{-ip_l}{2\alpha_m}\right)^{i_l} \sum_{s=0}^{[i_l/2]} \frac{1}{(i_l-2s)!s!} \left(\frac{\alpha_m}{-p_l^2}\right)^s \end{aligned} \tag{5.13}$$

where $l = 1, 2, 3$ corresponds to x, y, z and $[i_l/2]$ is the integral part of the real number in the square brackets. Inserting the analytical expression of the momentum wave function back into Eq. (5.6) yields

$$\begin{aligned} \langle \boldsymbol{v}(t)\rangle = &-\sum_{n,n'} \int_0^t dt' \sum_{\boldsymbol{\nu}} |\langle \chi_{f,\boldsymbol{\nu}} | \chi_{i,0}\rangle|^2 \\ &\times \int d\boldsymbol{p}\, \boldsymbol{h}_{n,n'}(\boldsymbol{p},t,t') e^{-i\tilde{S}^{n,n'}_{\boldsymbol{p},\boldsymbol{\nu}}(t,t')} + c.c. \end{aligned} \tag{5.14}$$

$$\begin{aligned} \boldsymbol{h}_{n,n'}(\boldsymbol{p},t,t') = &\left(\boldsymbol{p}+\boldsymbol{A}(t)\right) f_n^*(\boldsymbol{p}+\boldsymbol{A}(t)) \\ &\times \left\{ \boldsymbol{F}(t') \cdot \left[-i\boldsymbol{R}^{n'} f_{\boldsymbol{n'}}(\boldsymbol{p}+\boldsymbol{A}(t')) + \boldsymbol{\nabla}_{\boldsymbol{p}} f_{n'}(\boldsymbol{p}+\boldsymbol{A}(t')) \right] \right\} \end{aligned} \tag{5.15}$$

$$\tilde{S}^{n,n'}_{\boldsymbol{p},\boldsymbol{\nu}}(t,t') = S_{\boldsymbol{p}}(t,t') - (\boldsymbol{p}+\boldsymbol{A}(t))\cdot\boldsymbol{R}^n + (\boldsymbol{p}+\boldsymbol{A}(t'))\cdot\boldsymbol{R}^{n'} + \epsilon_{\boldsymbol{\nu}}(t-t'), \tag{5.16}$$

To carry out the momentum integral, we notice that the molecular wave function is well-localized in space. Therefore, the momentum space wave function must vary slowly since $\boldsymbol{p}$ is the conjugate variable of the space coordinate. In other words, we expect ϕ_0 and consequently the factors, f_n^*, f_n to be broad and slowly varying. Thus, $\boldsymbol{h}_{n,n'}(\boldsymbol{p})$ is slowly varying with $\boldsymbol{p}$. The semiclassical action, $\tilde{S}^{n,n'}_{\boldsymbol{p},\boldsymbol{\nu}}(t,t')$, varies with $\boldsymbol{p}$ proportional to $(t-t')$ (cf. Eq. (5.10)). Here, $t-t'$ is typically of the order of an optical cycle. Therefore, the phase in the momentum integral oscillates rapidly, on the scale $(t-t')^{-1}$. This behavior tends to average the momentum integral to zero due to the slowly varying leading factor $\boldsymbol{h}_{n,n'}(\boldsymbol{p})$. We may therefore use the stationary phase method

(SPM). Here, we assume that the contributions to the momentum integral are from small $\boldsymbol{p}$ intervals around the stationary points (SP) that are given by

$$\boldsymbol{\nabla}_{\boldsymbol{p}}\tilde{S}^{n,n'}_{\boldsymbol{p},\boldsymbol{\nu}}(t,t')\Big|_{\boldsymbol{p}=\boldsymbol{p}_{\rm SP}} = \boldsymbol{0} \Rightarrow$$
$$\boldsymbol{p}_{\rm SP} = (t-t')^{-1}\left[-\int_{t'}^{t} dt''\boldsymbol{A}(t'') + \boldsymbol{R}^{n} - \boldsymbol{R}^{n'}\right]. \qquad (5.17)$$

If we Taylor expand the action around these points

$$\tilde{S}^{n,n'}_{\boldsymbol{p},\boldsymbol{\nu}}(t,t') \approx \tilde{S}^{n,n'}_{\boldsymbol{p}_{\rm SP},\boldsymbol{\nu}}(t,t') + \frac{1}{2}\sum_{i=1}^{3}\frac{\partial^2}{\partial p_i^2}\tilde{S}^{n,n'}_{\boldsymbol{p},\boldsymbol{\nu}}(t,t')\Big|_{\boldsymbol{p}=\boldsymbol{p}_{\rm SP}}(p_i - p_i^{\rm SP})^2$$
$$\approx \tilde{S}^{n,n'}_{\boldsymbol{p}_{\rm SP},\boldsymbol{\nu}}(t,t') + \frac{1}{2}\sum_{i=1}^{3}(t-t')(p_i - p_i^{\rm SP})^2, \qquad (5.18)$$

we may carry out the momentum integral

$$\int d\boldsymbol{p}\, \boldsymbol{h}_{n,n'}(\boldsymbol{p}) e^{-iS^{n,n'}_{\boldsymbol{p},\boldsymbol{\nu}}(t,t')} \approx \boldsymbol{h}_{n,n'}(\boldsymbol{p}_{\rm SP}) e^{-iS^{n,n'}_{\boldsymbol{p}_{\rm SP},\boldsymbol{\nu}}(t,t')}$$
$$\times \prod_{i=1}^{3}\int_{-\infty}^{\infty} dp_i e^{-i(t-t')(p_i - p_i^{\rm SP})^2/2} \qquad (5.19)$$
$$= \boldsymbol{h}_{n,n'}(\boldsymbol{p}_{\rm SP}) e^{-iS^{n,n'}_{\boldsymbol{p}_{\rm SP},\boldsymbol{\nu}}(t,t')}\left(\frac{2\pi}{t-t'}\right)^{3/2} e^{-i\frac{3\pi}{4}}. \qquad (5.20)$$

There is a numerical issue for the SPM for $t-t'$ equal to zero or very large. We handle that by a *regularized integration* replacing the argument $-i(t-t')(p_i - p_i^{\rm SP})^2$ with $-(\epsilon+i)(t-t')(p_i - p_i^{\rm SP})^2$, ϵ a small positive number.[1] In this way we arrive at the final result for the momentum integral

$$\int d\boldsymbol{p}\, \boldsymbol{h}_{n,n'}(\boldsymbol{p}) e^{-iS^{n,n'}_{\boldsymbol{p},\boldsymbol{\nu}}(t,t')} \approx \boldsymbol{h}_{n,n'}(\boldsymbol{p}_{\rm SP}) e^{-iS^{n,n'}_{\boldsymbol{p}_{\rm SP},\boldsymbol{\nu}}(t,t')}\left(\frac{2\pi}{\epsilon + i(t-t')}\right)^{3/2}. \qquad (5.21)$$

5.2.3 Treating molecular orientation in the Lewenstein model

The treatment from Eq. (5.11) and until now assumes that we are in the MF coordinate system. However, we wish to carry out calculations in a laboratory fixed (LF) system defined by the laser polarization, $\boldsymbol{e}$. For a molecule of arbitrary orientation the LF and MF coordinate axes do not coincide. If the LF coordinate system is rotated with angle Ω with respect to the MF system, the wave function is given by

$$\psi_0(\Omega, \boldsymbol{r}) = \psi_0^{\rm MF}(\boldsymbol{M}_\Omega(\boldsymbol{r})) \qquad (5.22)$$

[1] The final result is insensitive to the exact size of ϵ. We use $\epsilon = 1$.

where $\boldsymbol{M}_\Omega$ is the orthogonal matrix that rotates from the LF frame to the MF frame [50]. The property $\boldsymbol{M}_\Omega^{-1} = \boldsymbol{M}_\Omega^T$ may be used to show that $\boldsymbol{p} \cdot \boldsymbol{r} = (\boldsymbol{M}_\Omega \boldsymbol{p}) \cdot (\boldsymbol{M}_\Omega \boldsymbol{r})$. Also, the determinant of the Jacobian of $\boldsymbol{M}_\Omega$ is unity. These two properties are enough to prove that $\phi(\Omega, \boldsymbol{p}) = \phi_0^{\mathrm{MF}}(\boldsymbol{M}_\Omega(\boldsymbol{p}))$. Correspondingly, all momenta in the action of Eq. (5.16) have to be rotated into the MF frame. In Eq. (5.17) the nuclear coordinates must be transformed into the LF frame.

5.3 HHG in the Kuchiev-Ostrovsky model

As an alternative to the Lewenstein model, we will briefly mention another approach that may be followed to evaluate HHG. This model was first suggested by Kuchiev and Ostrovsky for atoms [51] and later generalized to molecules [1]. The method relies on more approximations than the Lewenstein model, but is also easier to evaluate. We start from the Fourier transformation of the dipole (cf. Chapter 4)

$$S(\omega) = \left(\frac{1}{T} \left| \int_0^T dt\, e^{-i\omega t} \langle \boldsymbol{d}(t) \rangle \right| \right)^2, \tag{5.23}$$

$$\langle \boldsymbol{d}(t) \rangle \approx \sum_{\boldsymbol{\alpha}} P_{\boldsymbol{\alpha}} |\phi_{\boldsymbol{\alpha}}(\Omega, \bar{t})|^2 \int d\boldsymbol{R} |\chi_{\boldsymbol{\alpha}}(\boldsymbol{R}, \bar{t})|^2 \int d\boldsymbol{r} |\psi'_\xi(\Omega, \boldsymbol{R}; \boldsymbol{r}, t)|^2 \boldsymbol{r}. \tag{5.24}$$

We note that it has been an ongoing discussion, since the early 1990's whether the HHG spectrum should be calculated from the (pulse limited) Fourier transform of the dipole moment, the dipole velocity (as in Eq. (4.1)) or the dipole acceleration. By partial integration of the Fourier integral it is easily shown that up to a well-known frequency dependent factor one can interchange the dipole velocity with the dipole moment or the dipole acceleration, and the appropriate boundary terms vanish as long as the dipole relaxes to its initial value after the pulse [52]. The latter condition amounts to the assumption that the electron remains bound after the laser pulse has gone or that the electron is isotropically ejected from the molecule which holds true for relatively long and weak laser pulses. For short and intense laser pulses this is no longer true, and the use of an incorrect form leads to an unphysical background in the HHG spectrum [53, 54].

5.3.1 The molecular orbital in the Kuchiev-Ostrovsky model

We express the molecular orbital of the active electron in an expansion on spherical harmonics. So, in the MF frame

$$\psi_0^{\mathrm{MF}}(\boldsymbol{r}) = \sum_{l,m} F_{l,m}(r) Y_l^m(\hat{\boldsymbol{r}}) \tag{5.25}$$

with $\hat{\boldsymbol{r}} = \boldsymbol{r}/r$. We obtain the $F_{l,m}$'s by projecting Eq. (5.11) onto spherical harmonics. Asymptotically this expression follows the Coulomb form

$$\psi_0^{\mathrm{MF}}(\boldsymbol{r}) \sim \sum_{l,m} C_{l,m} r^{1/\kappa - 1} \exp(-\kappa r) Y_l^m(\hat{\boldsymbol{r}}) \tag{5.26}$$

with $\kappa = \sqrt{2I_P}$ and where the $C_{l,m}$'s are constants. As in the previous section, we wish to carry out calculations in the LF frame. Hence, we rotate the MF wave function. However, we write the rotation as

$$\psi_0(\Omega, \boldsymbol{r}) = D(\Omega)\psi_0^{\mathrm{MF}}(\boldsymbol{r}), \tag{5.27}$$

since the effect of the rotation operator, $D(\Omega)$, is readily evaluated in the spherical harmonic basis appearing in Eqs. (5.25) and (5.26) [50].

5.3.2 Expression for HHG

A basic ingredient in the Kuchiev-Ostrovsky model is to assume that the harmonic laser pulse can be considered monochromatic. We can then describe the laser field by the vector potential $\boldsymbol{A}(t) = \boldsymbol{A}_0 \cos(\omega_0 t)$, and this leads to a *photon picture* for HHG: The HOMO electron is first transferred to the continuum via above threshold ionization (ATI), i.e., by absorbing a number of photons from the driving laser. The electron then propagates in the laser-dressed continuum. Eventually, the laser field drives the electron back to the molecule thereby causing a laser-assisted recombination (LAR) in which the electron returns to the HOMO by emission of a harmonic photon. Mathematically the complex amplitude for the emission of harmonic with frequency $\omega = N\omega_0$ in this picture is given by [1]

$$\begin{aligned}\langle \tilde{\boldsymbol{d}}(\omega) \rangle = \frac{\omega_0}{2\pi} \int_0^{\frac{2\pi}{\omega_0}} dt\, e^{-i\omega t} \langle \boldsymbol{d}(t) \rangle = \sum_{l_2,l_1} \sum_{m_2',m_1'} \sum_{m_2,m_1} D^{l_2 *}_{m_2',m_2}(\Omega) D^{l_1}_{m_1',m_1}(\Omega) \\ \times C_{l_1,m_1} \sum_{\boldsymbol{\nu}} |\, \langle \chi_{f,\boldsymbol{\nu}} | \chi_{i,0} \rangle \,|^2 \\ \times \sum_k \sum_{C(k)} \boldsymbol{B}^{N,\boldsymbol{\nu},k}_{l_2,m_2',m_2}(C(k)) A^{\boldsymbol{\nu},k}_{l_1,m_1'}(C(k)).\end{aligned} \tag{5.28}$$

Here the factors

$$\begin{aligned}C_{l_1,m_1} A^{\boldsymbol{\nu},k}_{l_1,m_1'}(C(k)) = -C_{l_1,m_1} \frac{\omega_0}{2\pi} \Gamma\left(1 + \frac{Z/\kappa}{2}\right) 2^{\frac{Z/\kappa}{2}} \kappa^{Z/\kappa} (\pm 1)^{l_1} \\ \times \frac{\exp[i S^k_{\boldsymbol{p},\boldsymbol{\nu}}(t'_{C(k)})]}{\sqrt{[-i S^{k''}_{\boldsymbol{p},\boldsymbol{\nu}}(t'_{C(k)})]^{1+Z/\kappa}}} \, Y^{m_1'}_{l_1}\left(\hat{\boldsymbol{p}}'\right) \Big|_{\boldsymbol{p}' = \boldsymbol{p}^{\nu}_k + \boldsymbol{A}(t'_{C(k)})},\end{aligned} \tag{5.29}$$

and

$$\boldsymbol{B}^{N,\boldsymbol{\nu},k}_{l_2,m_2',m_2}(C(k)) = i2\pi\omega_0 \int_0^{\frac{2\pi}{\omega_0}} dt \frac{\exp[i(N\omega_0 t - S^k_{\boldsymbol{p},\boldsymbol{\nu}}(t))]}{L_0(t,t'_{C(k)})} \times \boldsymbol{\nabla}_{\boldsymbol{p}} \left[G_{l_2,m_2}(p) Y^{m_2'}_{l_2}(\hat{\boldsymbol{p}})\right]^* \Big|_{\boldsymbol{p}=\boldsymbol{p}^{\boldsymbol{\nu}}_k+\boldsymbol{A}(t)} \tag{5.30}$$

along with their Wigner rotation functions are respectively interpreted as ATI and propagation-LAR amplitudes, of a HOMO electron having absorbed k photons during the ATI-step. In Eqs. (5.29) and (5.30) $\boldsymbol{p}$ and $\boldsymbol{p}'$ are electron momenta and

$$S^k_{\boldsymbol{p},\boldsymbol{\nu}}(t) = k\omega_0 t + \boldsymbol{p}^{\boldsymbol{\nu}}_k \cdot \boldsymbol{\alpha}_0 \sin(\omega_0 t) + \frac{U_p}{2\omega_0}\sin(2\omega_0 t). \tag{5.31}$$

The index $C(k)$ in Eqs. (5.28)-(5.30) denotes saddle-points. For each k the saddle-points $t'_{C(k)}$ are defined by the condition $S^{k'}_{\boldsymbol{p},\boldsymbol{\nu}}(t'_{C(k)}) = 0$. In this context, we restrict ourselves ourselves to points with $0 \leq \mathrm{Re}(t'_{C(k)}) < 2\pi/\omega_0$ and $\mathrm{Im}(t'_{C(k)}) > 0$. The factors $(\pm 1)^{l_1}$ in Eq. (5.29) correspond to the limits $\pm i\kappa$ of the magnitude p' of the electron momentum at the saddle-points. The factor $1/L_0(t,t'_{C(k)}) = \sigma\alpha_0(\sin\omega_0 t'_{C(k)} - \sin\omega_0 t)$ in Eq. (5.30) describes the decrease of the amplitude of the electron wave as it propagates in the field-dressed continuum. Here, $\sigma = \pm 1$ is chosen to assure $\mathrm{Re}(L_0) > 0$. $\boldsymbol{p}^{\boldsymbol{\nu}}_k$ is the part of the continuum electron momentum arising from absorption of k laser photons during ATI. It is parallel (antiparallel) with the polarization vector of the laser field if the value of σ is 1 (-1). The magnitude of the momentum is $p^{\boldsymbol{\nu}}_k = \sqrt{2(k\omega_0 - I_p - \epsilon_{\boldsymbol{\nu}} - U_p)}$ where $U_p = A_0^2/4$ is the ponderomotive potential. Finally, in Eq. (5.30) the function $G_{l_2,m_2}(p)$ is the radial part of the momentum space molecular orbital. It is obtained by taking the Fourier transform of Eq. (5.25) (see Ref. [1] for further details).

5.3.3 Asymptotic expression for HHG

To arrive at Eq. (5.28), we have used the asymptotic form of the molecular orbital (Eq. (5.26)) in the ATI step, but the exact form (Eq. (5.25)) in the recombination step. A simpler expression for the harmonic generation can be obtained by using the asymptotic form of the molecular orbital in both the ATI and the recombination step. In this approximation the Nth harmonic is given by

$$\langle \tilde{\boldsymbol{d}}^{as}(\omega)\rangle \sim \sum_{l_2,l_1}\sum_{m_2',m_1'}\sum_{m_2,m_1} D^{l_2*}_{m_2',m_2}(\Omega) D^{l_1}_{m_1',m_1}(\Omega) C^*_{l_2,m_2} C_{l_1,m_1} \times \sum_{\boldsymbol{\nu}} |\langle \chi_{f,\boldsymbol{\nu}} | \chi_{i,0}\rangle|^2 \sum_k \sum_{C(k)} \tilde{\boldsymbol{B}}^{N,\boldsymbol{\nu},k}_{l_2,m_2'}(C(k)) A^{\boldsymbol{\nu},k}_{l_1,m_1'}(C(k)), \tag{5.32}$$

with

$$\tilde{\boldsymbol{B}}^{N,\boldsymbol{\nu},k}_{l_2,m_2'}(C(k)) = i\sqrt{22}\pi\omega_0 \int_0^{\frac{2\pi}{\omega_0}} dt \frac{\exp[i(N\omega_0 t - S^k_{\boldsymbol{p},\boldsymbol{\nu}}(t))]}{L_0(t,t'_{C(k)})}$$
$$\times \boldsymbol{\nabla}_{\boldsymbol{p}} \Bigg[\left(\frac{p}{i\kappa}\right)^{l_2} \frac{1}{2^{l_2+1}\kappa^{2+Z/\kappa}} \frac{\Gamma(l_2+2+Z/\kappa)}{\Gamma(l_2+\frac{3}{2})} Y^{m_2'}_{l_2}(\hat{\boldsymbol{p}})$$
$$\times {}_2F_1\Bigg(\frac{l_2+2+Z/\kappa}{2}, \frac{l_2+2+Z/\kappa}{2}+\frac{1}{2}; \dots$$
$$l_2+\frac{3}{2}; -\left(\frac{p}{\kappa}\right)^2 \Bigg) \Bigg]^* \Bigg|_{\boldsymbol{p}=\boldsymbol{p}^{\boldsymbol{\nu}}_k+\boldsymbol{A}(t)} . \tag{5.33}$$

Here, ${}_2F_1(\dots)$ is Gauss' hypergeometric function.

The asymptotic expression in Eq. (5.32) is advantageous because all geometric factors are pulled outside the integration. In Chapter 7 we compare HHG spectra obtained with the two forms of Eqs. (5.28) and (5.32). Significant deviations are seen which shows that HHG is sensitive to the detailed structure of the target molecule, not simply the asymptotic behavior.

5.4 Semiclassical orbits in the model calculations of HHG

In the models presented above, we have reduced the computational costs by exploiting that action, S, (Eq. (5.16) in the Lewenstein case and Eq. (5.31) in the Kuchiev-Ostrovsky case) gives rise to a rapidly oscillating phase factor $\exp(-iS)$. This means that integration over either electron momenta in the Lewenstein case or time in the Kuchiev-Ostrovsky case can be simplified by integration only over small regions around points where derivative of S with respect to either momenta or time is zero. It is very useful to to connect these points with the quantum orbits.

In the Lewenstein case we deal with the SP momenta given by in Eq. (5.17) which can in each case be interpreted as the momentum coinciding with a semiclassical orbits of electrons that are ionized at $\boldsymbol{R}_{n'}$ and recombining at $\boldsymbol{R}_n$. This includes orbits from one atom to itself and from one atom to another. We refer to these as *direct* and *exchange harmonics* respectively. An example of the two types of orbits is presented in Fig. 5.1. The electron is ionized at one atomic center at the peak of the field and recombines two thirds of an optical cycle later. The orbit that gives rise to direct harmonics has been plotted with a small artificial transverse displacement in order to separate the two parts of the electron motion. Similar orbits exist which describe ionization at the other atomic center.

The Kuchiev-Ostrovsky model contains no geometrical information in the phase. Consequently, there is no multi-center character related to the times at which the time derivative of Eq. (5.31) is zero. It follows from this that

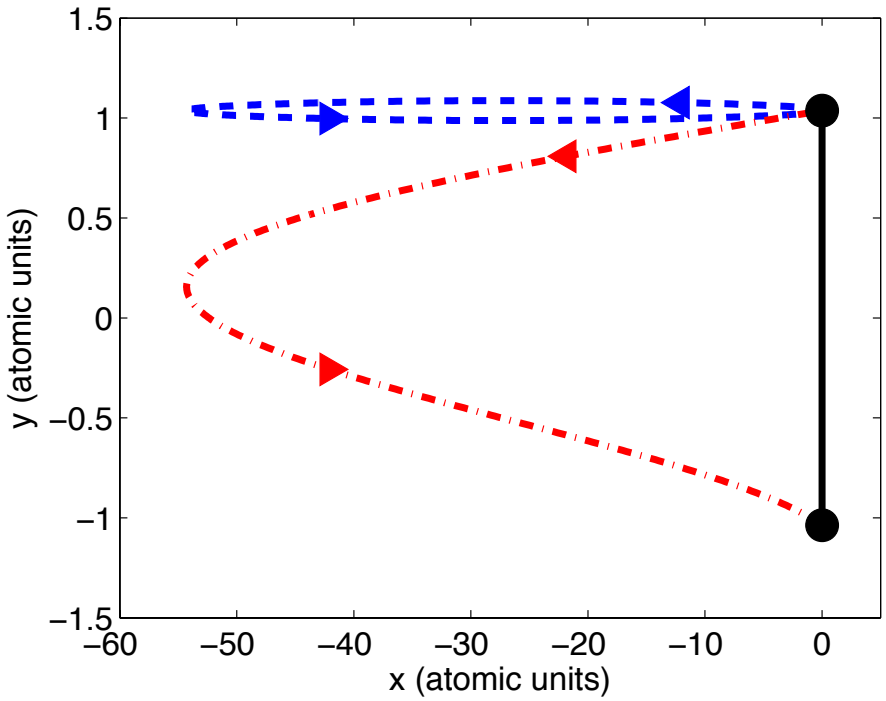

Figure 5.1: Two semiclassical orbits with ionization at the peak of the field and recombination two thirds of an optical cycle later (cf. the three-step model, Fig. 4.1). The atomic centers of the molecule are sketched as black dots to the right. The laser polarization is taken to be in the x-direction. The dashed (blue) line represents an orbit that gives rise to direct harmonics, i.e., ionization and recombination at the same center and consequently harmonic radiation polarized parallel to the laser field. The dash-dotted (red) line is an orbit that gives rise to exchange harmonics, i.e., ionization at one center and recombination at another center. In this case elliptically polarized harmonic radiation may be produced.

the momentum $\boldsymbol{p}_k^{\boldsymbol{\nu}}$ has to be parallel to the laser polarization. Referring to Fig. 5.1 an electron that leads to HHG is in the Kuchiev-Ostrovsky model starts and ends at the origin.

5.5 Ionization in the SFA

To calculate ionization within the SFA we project the solution from Eq. (5.5) onto the Volkov state at the end of the pulse, T, in order to get the amplitude for a transition to an outgoing continuum state of asymptotic momentum $\boldsymbol{p}$ [55]

$$T_{f,\boldsymbol{\nu},i}(\boldsymbol{p}) = -i \int_0^T dt' \langle \psi_{\boldsymbol{p}}^{\mathrm{V}}(t') \chi_{f,\boldsymbol{\nu}}(t') | V_{\mathrm{Laser}}(t') | \psi_0(t') \chi_{i,0}(t') \rangle. \tag{5.34}$$

We return to this result in Chapter 9.

5.6 Summary

In this chapter, we introduced the strong-field approximation, a very common method to calculate the dynamics of atoms and molecules in a strong field. The assumptions that goes into the strong-field approximation are that the electron is unaffected by the laser field until ionization and that the ionized electron does not feel the attractive potential of the residual cation. Within the strong-field approximation, we presented expressions for the calculation of high-order harmonic generation and ionization. In the case of high-order harmonic generation two explicit schemes for calculation were presented: the more general Lewenstein model and the Kuchiev-Ostrovsky model that applies to the case of continuous wave lasers.

Chapter 6

HHG and the influence of molecular structure

In this chapter we will use the strong-field approximation approach outlined in Chapter 5 to calculate the high-order harmonic generation from molecules. We focus on the influence of molecular structure on the HHG. More specifically, we are thinking about effects that are due to the geometry of the molecule (not nuclear dynamics) and that cannot play a role in HHG from atoms. It is clear from Eq. (5.6) that according to the SFA the molecular structure enters in the ionization step (Eq. (5.9)) and in the recombination step (Eq. (5.8)) and we expect general properties of the molecular orbitals such as symmetries and nodal planes to be imprinted in the HHG signal. In fact, the relation between the HHG yield and the molecular orbital resulted in several experimental efforts to use HHG to reconstruct molecular orbitals [19, 20]. Another not unrelated property, is the multi-center structure defined by the positions of the atoms that make up the molecule. We will see below how this gives rise to structural minima and accompanying elliptically polarized harmonics even though the laser pulse that drives HHG is linearly polarized.

6.1 Signature of ionization and recombination in the HHG signal

A commonly accepted statement is that the role of ionization is to influence the overall efficiency of HHG. The ionization yield can depend strongly upon the orientation of the molecule with respect to the laser polarization axis, which leads to an orientational dependence of HHG. For recombination, the momenta of the returning electron are significantly higher than the initial momenta, due to the acceleration of the electron in the laser field. The de Broglie wavelength of the electron can be comparable to the internuclear distance, and thus one may expect interference effects [first suggested in Ref. [15]]. We will return to the latter point in the next section.

To exemplify the roles of ionization and recombination in HHG, we consider the calculated HHG from ethylene (C_2H_4). Ethylene is a good candidate

for this purpose, because the relative angle between the molecule and the laser polarization can be controlled via the technique of field-free one dimensional alignment [56, 57] (see Chapter 8 for details on alignment) meaning that the orientation dependance of HHG from this molecule can be fully explored. In the calculations presented in this section, we assume that the laser driving the HHG is linearly polarized (which defines the LF Z axis) with a wavelength of 800 nm and intensity 1.8×10^{14} W/cm^2.

Figure 6.1 shows HHG spectra from ethylene at different angles θ between the MF z axis (see Fig. 6.2(a)) and the LF Z axis defined by the laser polarization, but where the directions of the MF x and y axes are undefined. This scenario corresponds to one dimensional alignment. First, we point out some generic features of HHG spectra. The absence of even harmonics in the spectrum is due to the inversion symmetry of the highest occupied molecular orbital (HOMO) of ethylene (see Fig. 6.2(a)). Basically, inversion symmetry implies that the harmonic radiation emitted at a given point of time has a π phase difference with radiation emitted half an optical cycle later. The Fourier spectrum of such a signal has only odd frequency components and the peaks are separated by twice the laser photon frequency. Another characteristic feature is the plateau structure[1] from harmonics 9 to 29 followed by a cutoff at the harmonic order given by the semiclassical formula:

$$\text{Cutoff energy} \approx I_p + 3.17U_p, \tag{6.1}$$

which yields $29 \times \omega_0$ (where we use $I_p = 10.5$ eV for ethylene). Here, U_p is the ponderomotive potential that was defined in Chapter 5. Finally, we comment on the fact that the overall effect of orienting the molecule is a scaling of the spectrum. The reason for this scaling is that all harmonics have similar orientational dependence.

To look into the interplay between ionization and recombination, we assume that MF z axis is oriented at an angle θ with respect to the LF Z and the molecule is rotated some fixed angle χ around the MF z axis. Then not only the MF z axis, but also the x and y axes are fixed which corresponds to the case of three dimensional alignment. Figure 6.2 shows representative results of the calculations. In order to understand the results, we also show the HOMO of ethylene in the figure. We use the Kuchiev-Ostrovsky model in this section and as explained in Chapter 5 this implies that the electron has to escape and return along the laser polarization axis (cf. Eq. (5.29)). This is impossible, if the polarization axis lies along the nodal plane, which is the reason for the vanishing harmonic signal, when either $\theta = 0^\circ$ (180°) or $\chi = 0^\circ$ $(180^\circ, 360^\circ)$. When the molecule is rotated, the nodal plane is removed from the polarization axis of the laser and the intensity of the harmonics increases. As seen in Figs. 6.2(b)-(c), the harmonics peak at different values of the Euler angle θ. The varying positions of the peaks arise from competing effects of the ionization and propagation-recombination steps making up the HHG process:

[1] The plateau structure is not displayed very clearly with the axis parameters used. See Fig. 7.4 for a better example.

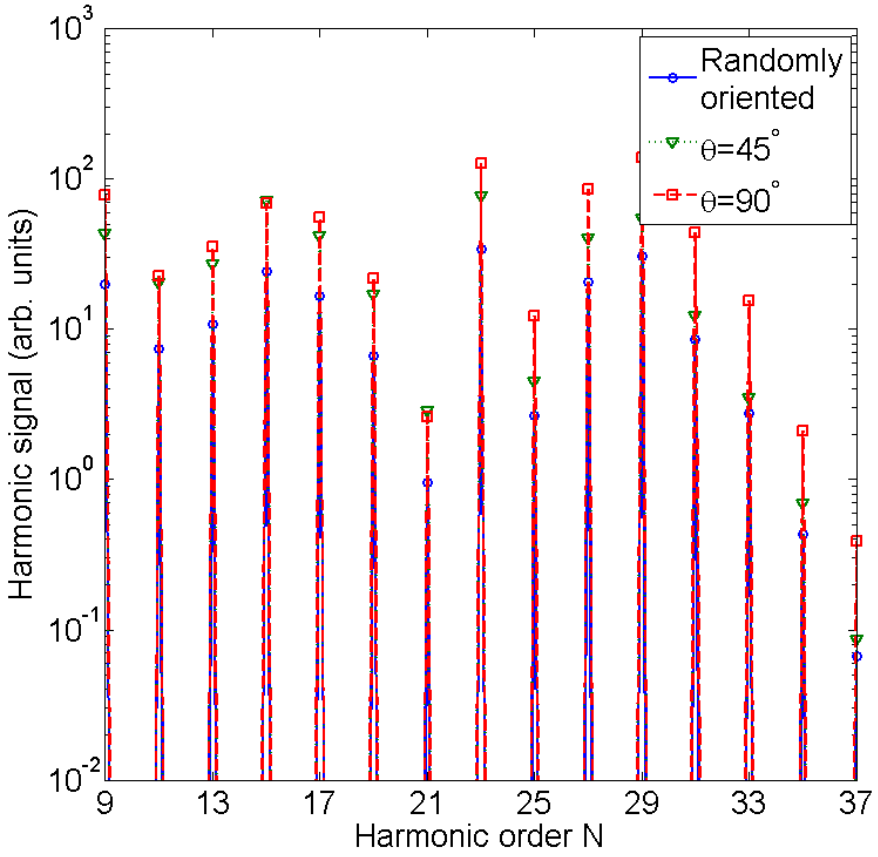

Figure 6.1: The orientational dependence of the harmonic spectrum from ethylene (C_2H_4). Effectively orientation corresponds to an overall scaling of the spectrum. The absence of even harmonics is explained by the inversion symmetry of the HOMO (see text for details). The results are for an 800 nm, 1.8×10^{14} W/cm^2 harmonic-generating laser.

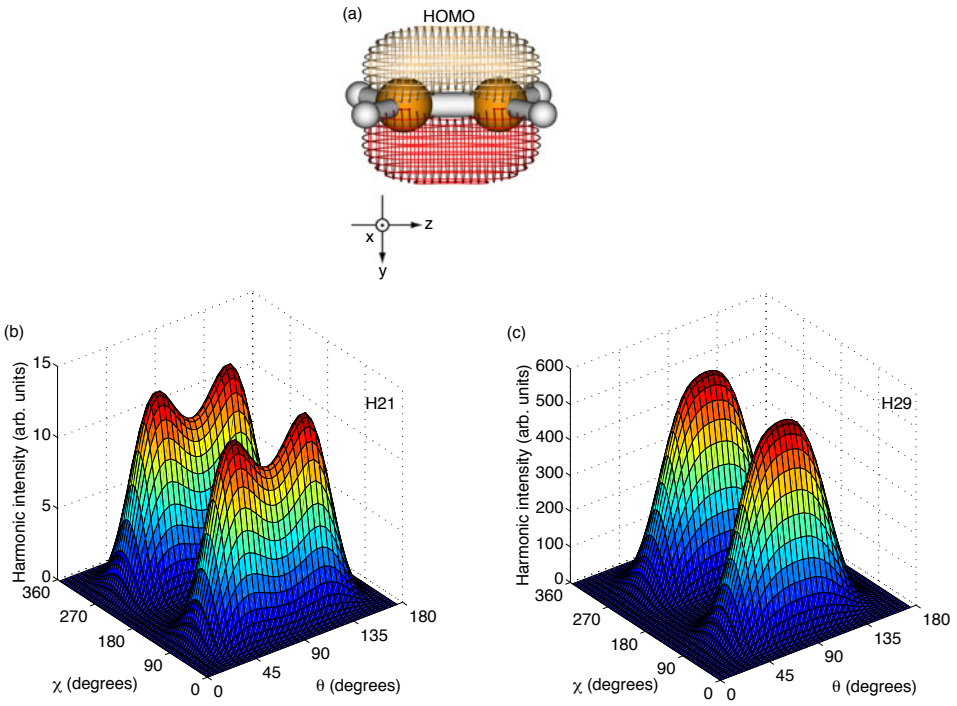

Figure 6.2: This figure illustrates the interplay of ionization and recombination in relation to HHG. (a) The geometry of ethylene (C_2H_4) along with an isocontour for the HOMO. We use the color red to indicate a negative sign of the HOMO wave function and golden to indicate a positive sign. Directions of the MF coordinate axes are shown (but we use the center of mass as the origin of the MF coordinate system). (b) and (c) show the dependencies of the 21st (H21) and 29th (H29) harmonics on orientation as given by Euler angles θ and χ (see text). The results are for an 800 nm harmonic-generating laser of intensity 1.8×10^{14} W/cm^2.

As the electron escapes along the polarization direction the ionization is maximal when θ lies in between 0° and 90°. The propagation-recombination step, however, is optimized when $\theta = 90°$, but the width of the θ-peak depends on the harmonic order. These observations account for the different orientational behavior of the harmonics shown in Fig. 6.2(b)-(c).

In the Kuchiev-Ostrovsky model for HHG the ionization and recombination basically enter as independent factors (see Eq. (5.28)). This idea is fundamental for the experimental procedures used to reconstruct molecular orbitals mentioned in the introduction to this chapter. As we will see in the next section, however, there is an important correlation between ionization and recombination when the less crude Lewenstein model is employed.

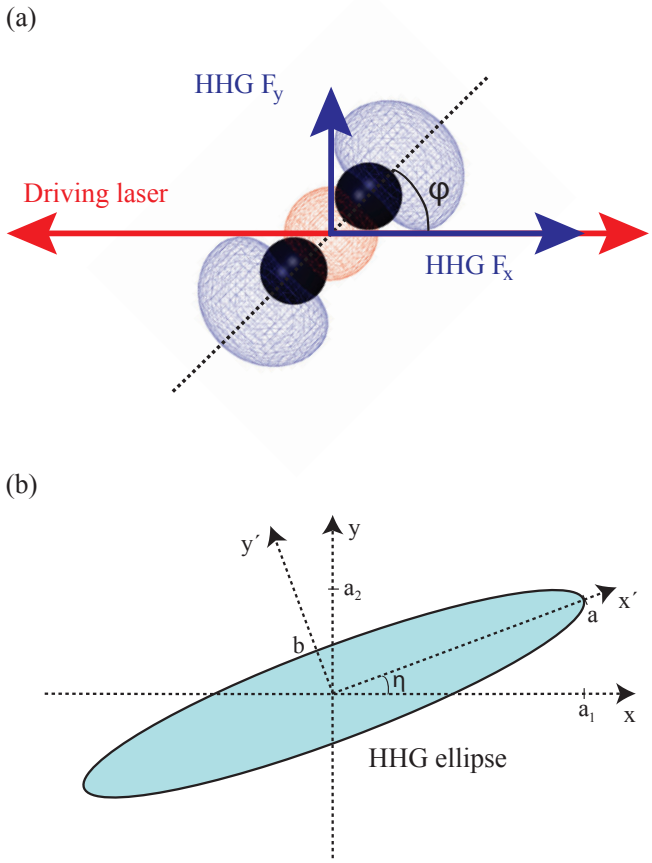

Figure 6.3: Coordinate systems and angles involved in studying the polarization of the high-order harmonics from N_2 with a linearly polarized driving laser. (a) We assume that the driving pulse is linearly polarized along the x-axis. The molecule is aligned at an angle of ϕ to the x-axis in the xy-plane. The alignment at a given angle with respect to the external field results in harmonic emission with components E_x and E_y. (b) The polarization ellipse for a single harmonic.

6.2 Polarization effects

For HHG from an isotropic target, such as a gas of atoms or unaligned molecules, it follows from symmetry arguments that the emitted harmonics have to be polarized parallel to the linearly polarized driving laser. Breaking the isotropy of the target by aligning the molecules (see Fig. 8.1) allows for a non-vanishing perpendicular polarization component in the emitted high-order harmonics. This scenario is depicted in Fig. 6.3 with an N_2 molecule.

Generally, the perpendicular component is heavily suppressed compared

to the parallel component and only the parallel component needs to be considered. However, recent experiments on aligned N_2, O_2 and CO_2 have reported a non-vanishing perpendicular component [58]. Moreover, elliptically polarized harmonics have been measured from aligned N_2 and CO_2 [59]. The observation of elliptically polarized harmonics is very interesting. First, the presence of elliptically polarized harmonics opens up the possibility of generating elliptically polarized ultrashort (attosecond) pulses in the extreme ultraviolet (XUV) wavelength regime. Second, it serves as an important benchmark for theory and as such the fundamental understanding of HHG.

Several approaches are currently used to calculate the HHG response. Ideally, one should propagate the TDSE. This approach has been used for atoms and small molecules [60, 61]. An example is the prediction of comparable polarization components from aligned H_2^+ near minima in the spectrum [62]. For systems beyond H_2^+ and H_2 one commonly uses methods such as the Lewenstein or Kuchiev-Ostrovsky models introduced in Chapter 5. For the Kuchiev-Ostrovsky model the electron has to escape and recombine parallel to the laser polarization axis, and it follows that a molecule exposed to a linearly polarized HHG driving laser always results in linearly polarized HHG radiation. We point out that this behavior is not because of the strong-field approximation. It owes to the fact that the method employed fails to take into account the spatial extent of the molecule. The Lewenstein model, on the other hand, is based on an expansion of the wave function around the atomic centers. This leads to *exchange harmonics* [47] that are caused by quantum orbits describing an ionization event at one atomic center followed by recombination at another atomic center (see Chapter 5). This then opens the possibility for generation of elliptically polarized high-order harmonics.

6.2.1 Elliptically polarized harmonics from N_2 with a linearly polarized driving pulse

In this section, we will show some proof-of-principle calculations on N_2 in order to illustrate that the Lewenstein model from Chapter 5 indeed leads to elliptically polarized harmonics when using a linearly polarized driving pulse. We assume that the molecules are perfectly aligned. The alignment geometry and the polarization ellipse are shown in Fig. 6.3. The driving field is taken to be an 800 nm pulse with 11 cycles in a trapezoidal envelope with 3 optical cycles for the linear ramp-up and ramp-down. The peak intensity is 6×10^{14} W/cm^2. This intensity is very high compared to the intensity used in experiments [59]. The discrepancy is due to our use of a trapezoidal envelope, which introduces some noise in the signal of the perpendicular harmonic component. Increasing the intensity reduces the importance of this noise. As we do not concern ourselves with parts of the spectrum near cutoff, this is an acceptable approach.

We follow the polarization conventions of Ref. [63]. This means that the

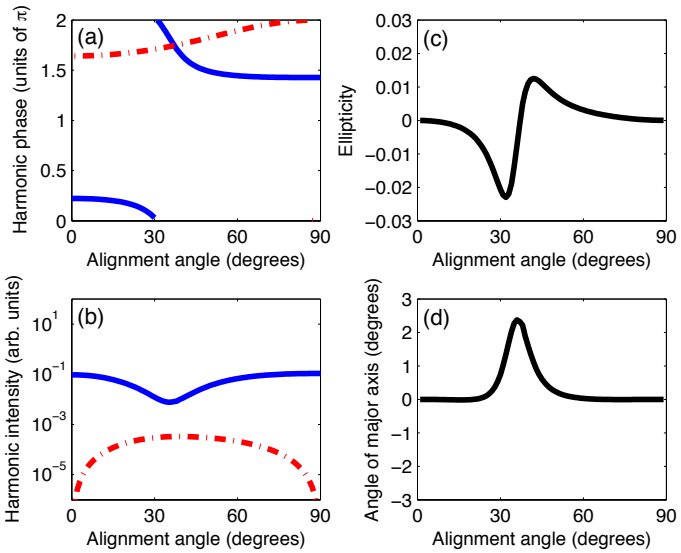

Figure 6.4: Orientation dependence of harmonic 17 from the HOMO of N_2 with equilibrium internuclear distance $R_0 = 1.0977$ Å. We use an 800 nm, 6×10^{14} W/cm^2 driving field. The envelope (for the vector potential) is trapezoidal with three optical cycles turn-on and turn-off and five cycles constant amplitude. (a) Harmonic phase (b) Harmonic intensity (c) Ellipticity (d) Angle of polarization ellipse major axis with respect to molecular axis. In (a) and (b) the solid (blue) curves refer to the parallel polarization component and the dash-dotted (red) curves to the perpendicular component.

harmonic of angular frequency ω is assumed to be a perfect plane wave

$$\mathbf{F}^H(t) = a_1 \cos(\omega t + \delta_1)\mathbf{e}_x + a_2 \cos(\omega t + \delta_2)\mathbf{e}_y \quad (6.2)$$

$$= a \cos(\omega t + \delta_0)\mathbf{e}_{x'} \pm b \sin(\omega t + \delta_0)\mathbf{e}_{y'}, \quad (6.3)$$

where the unit vectors $\boldsymbol{e}_x, \boldsymbol{e}_y, \boldsymbol{e}_{x'}, \boldsymbol{e}_{y'}$ and the axes $, a_1, a_2, a, b$ are defined in Fig. 6.3 (b). Phases δ_i $(i = 0, 1, 2)$ are found by assuming that the harmonic phase is equal to that of the dipole velocity [62, 64]. The two physically relevant quantities are the ellipticity ϵ, and the angle η that the polarization ellipse major axis makes with the polarization of the driving pulse. These are determined by

$$\epsilon = \pm\frac{b}{a} \quad , \quad -\frac{\pi}{4} \leq \tan^{-1}(\epsilon) \leq \frac{\pi}{4} \quad (6.4)$$

and

$$\tan(2\eta) = \frac{2a_1/a_2}{1 - (a_1/a_2)^2} \cos(\delta_2 - \delta_1). \quad (6.5)$$

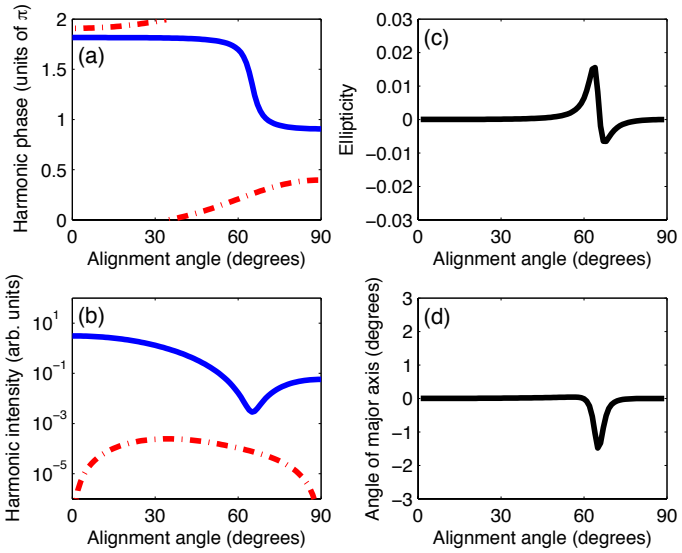

Figure 6.5: Same as Fig. 6.4, but for harmonic 27.

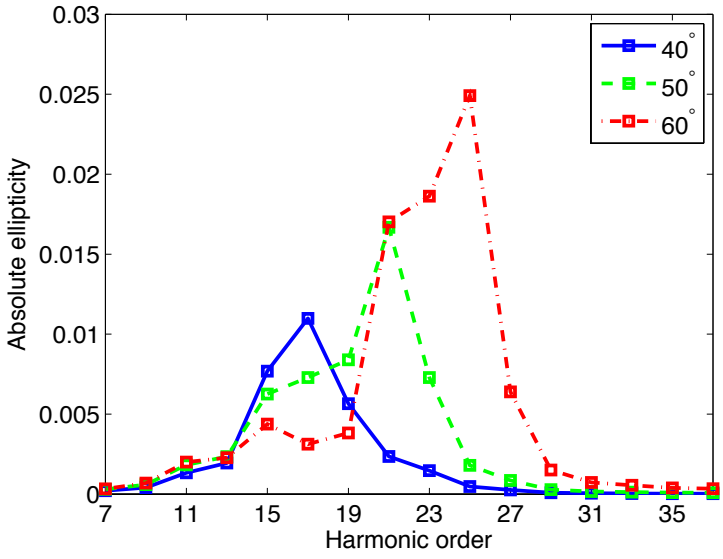

Figure 6.6: Absolute value of the harmonic ellipticity (see Fig. 6.3 and Eq. (6.4)) as a function of harmonic order for selected alignment angles ϕ of N_2. The nuclei are fixed at their equilibrium position. The solid (blue) curve refers to $\phi = 40°$, the dashed (green) curve to $\phi = 50°$, and the dash-dotted (red) curve to $\phi = 60°$. See the caption of Fig. 6.4 for laser parameters.

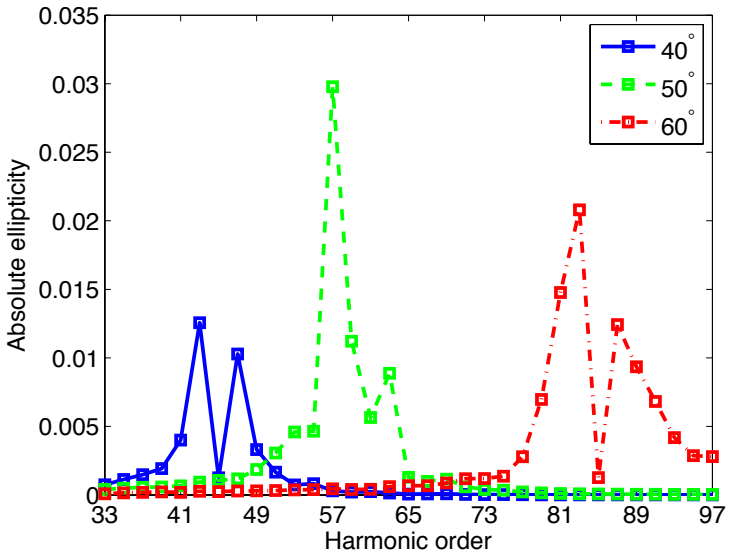

Figure 6.7: Same as Fig. 6.6, but with the nuclei fixed at $R = 2R_0$.

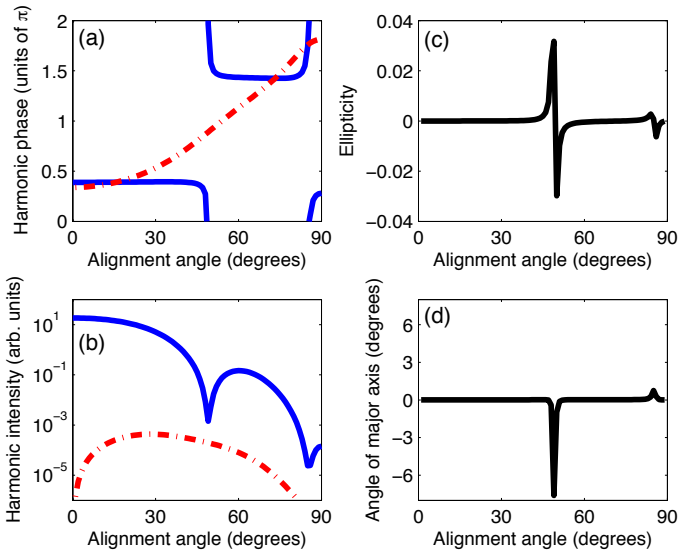

Figure 6.8: Same as Fig. 6.4, but for harmonic 57 and with $R = 2R_0$.

We now look at HHG from N_2 with the nuclei clamped at the equilibrium nuclear spacing of $R_0 = 1.0977$ Å. Figures 6.4(a)–(b) and 6.5(a)–(b) show data for harmonics 17 and 27, with solid (blue) curves referring to the component parallel with the linear polarization of the driving field and dash-dotted (red) curves referring to the perpendicular component. Panel (a) illustrates how the parallel polarization component of the harmonic emission changes its phase much faster than the perpendicular component. Comparison with panel (b) shows that the rapid change in phase is accompanied by a drop in harmonic intensity, causing an increase in the ratio of perpendicular to parallel harmonic intensity. We determine the ellipticity ϵ and the angle η of the major axis using Eqs. (6.4)–(6.5). Results are shown in panels (c) and (d). Both are seen to be very angle-dependent, taking non-vanishing values where the parallel component has a rapid change in phase. This variation in phase changes the helicity, i.e., the sense of rotation, of the harmonics over a very short angle interval, while the angle of the major axis has a definite sign for a given harmonic. Figure 6.6 shows the absolute value of the ellipticity as a function of harmonic order for selected alignment angles. The angular dependence can be mostly understood by comparing panel (b) in Fig. 6.4 with that in Fig. 6.5. The dip in the intensity of the parallel component is fairly narrow and moves to larger angles for increasing harmonic order. Below, we explore the origin of this structural dip of the harmonics which is due to interference in the recombination step.

The ellipticities calculated here do not compare well with [59]. The experimental ellipticities are an order of magnitude higher and have almost no angle-dependence. However, our results show that elliptically polarized high-order harmonics are predicted within the Lewenstein model. Improvements have to be made in order to compare the model directly with experimental data. One of these is to include the lower-lying molecular orbitals. The inclusion of these is expected to cause a dynamical minimum in the parallel component [65], which would change the detailed structure. Further, several results have indicated that the influence of the residual molecular potential on the electron, which is neglected in the SFA, leads to elliptically polarized harmonics [65–67].

6.2.2 Structural interference effects

We now return to the dip in the intensity of the parallel component of the harmonics. This is due to a two-center interference that comes about, because the recolliding electron finds two possible sites for recombination. For a diatomic homonuclear molecule we can write Eq. (5.11) as an atomic orbital, ϕ_0, centered at the two different atomic sites

$$\psi_0(\boldsymbol{r}) \simeq \phi_0(\boldsymbol{r} - \boldsymbol{R}/2) + \phi_0(\boldsymbol{r} + \boldsymbol{R}/2) \tag{6.6}$$

Note, that this form applies not only to the MF wave function, but also the rotated form. We then have for the recombination matrix element (Eq. (5.8))

$$\boldsymbol{v}_{\mathrm{rec}}(\boldsymbol{p}) \propto \boldsymbol{p} \int d\boldsymbol{r} \exp[-i\boldsymbol{p}\cdot\boldsymbol{r}]\phi_0(\boldsymbol{r}) \cos(\boldsymbol{p}\cdot\boldsymbol{R}/2). \tag{6.7}$$

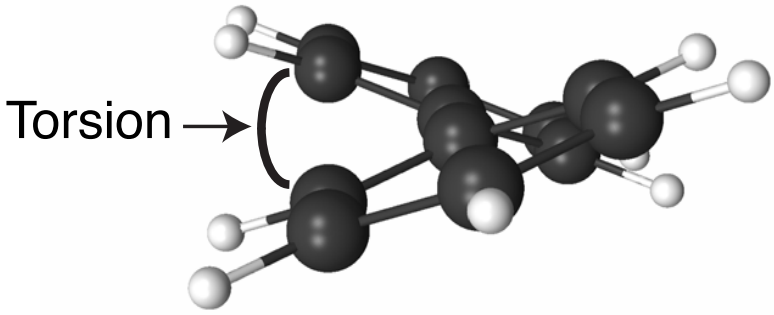

Figure 6.9: The biphenyl molecule is composed of two phenyl rings, i.e., each ring has the formula C_6H_{5-} where the six carbon atoms are arranged in a cyclic ring structure. The rings are connected by making a C-C bond. Torsion refers to the angle between the two phenyl rings.

The term $\cos(\boldsymbol{p} \cdot \boldsymbol{R}/2)$ is minimal when the destructive interference condition

$$\boldsymbol{p} \cdot \boldsymbol{R} = pR\cos\phi = (2n+1)\pi, n = 0, 1, \ldots \tag{6.8}$$

is met. This happens at specific electron recollision momenta p or equivalently de Broglie wavelengths, $2\pi/p$, corresponding to given harmonic orders for an alignment angle, ϕ. The explanation given above is actually a little too simple for N_2. In this case the atomic orbital is not exactly of the form given in Eq. (6.6), but will contain an additional term, where atomic orbitals centered at the two different atomic centers are subtracted. For this term (by itself) the interference condition is shifted by $\pi/2$, because the cosine becomes a sine. In any case, the internuclear separation will have an effect on this interference. Figure 6.7 shows results for N_2 with $R = 2R_0$. The plotted ellipticity is seen to peak at higher harmonic orders than at $R = R_0$. There is no significant change in the magnitude of the obtained ellipticities. Figure 6.8 shows the detailed behavior of the 55th harmonic.

We mention for the sake of completeness that a discussion of the polarization of the harmonic photons and a relation to the interference minima of N_2 was presented for the first time in [68]. Here, however, the dynamics were restricted to the recombination step and the photons were obtained from the complex conjugated photoionization transition amplitudes.

6.3 HHG as probe of molecular torsion

To conclude this chapter we briefly look at HHG from the biphenyl molecule. This molecule consists of two phenyl rings connected by a C-C axis (see Fig. 6.9). We will show in Chapter 10 how the *torsion* of the molecule, i.e.,

the angle between the two phenyl rings can be controlled by lasers. Such control is interesting in itself, but moreover it may be utilized to probe chemical processes such as de-racemization with time-resolution, and the torsion is a potential tool for the realization of molecular switches. As torsional motion of biphenyl takes place on a picosecond (1 ps = 10^{-12} s) time scale we may treat the torsion as fixed during the interaction with a femtosecond laser.

Figure 6.10 shows the electronic structure, more precisely the structure of the HOMO, of biphenyl as a function of torsion. As the torsion is increased from 0 towards 90°, a significant change in the spatial appearance of the HOMO is observed and further the binding energy is increased. The observed change of orbital structure is an important element in molecular switching. Since the increase of torsion from 0 towards 90° leads from a HOMO delocalized over the whole molecule to an orbital which is more localized on either of the phenyl rings it affects the ability to use the molecule to transmit a current [69]. We currently suggest that a probe giving information about the electron localization of biphenyl in gas phase may yield information about the conductivity of biphenyl in a molecular junction.

Figure 6.11 shows the HHG spectrum for biphenyl as a function of torsion. We use a 2×10^{14} W/cm^2, 775 nm laser field. The envelope is trapezoidal and consists of three optical cycles turn-on and turn-off and five cycles of constant amplitude. As the binding energy changes by just 0.3 eV, the cutoff will vary with less than a harmonic order (cf. Eq. (6.1)), and this change is hard to identify in the HHG spectrum. On the other hand, we see that the drastic changes of the orbital as torsion is increased leads to a large dependence of the spectrum on the torsion for lower lying harmonics. Such an order-of-magnitudes difference is easily observed in an experiment.

In Chapter 10 we probe the torsion of molecules by ionization using a femtosecond laser. Such an approach demands that some hydrogens be substituted with other atoms. In contrast, HHG provides a probe for torsion where no substitution is needed. Further, the method is all-optical, ideally non-demolishing (does not destroy the biphenyl target) and is seen very sensitive to small changes of torsion.

6.4 Summary

We studied the influence of molecular structure on high-order harmonic generation. In the three-step picture for high-order harmonic generation, the process is a product of ionization, acceleration of the electron in the laser field and recombination, and the molecular structure enters in the ionization and the recombination steps. We studied the interplay of these two steps and saw how they influence the dependence of the harmonics on the orientation of the molecule with respect to the laser field. Next, we saw how elliptically polarized harmonics can arise from a linearly polarized driving laser pulse as a result of electron drift from one atomic center of the molecule to another. We finally looked into the possibility of using high-order harmonic generation to study the torsional angle of the biphenyl molecule, and concluded that high-harmonic

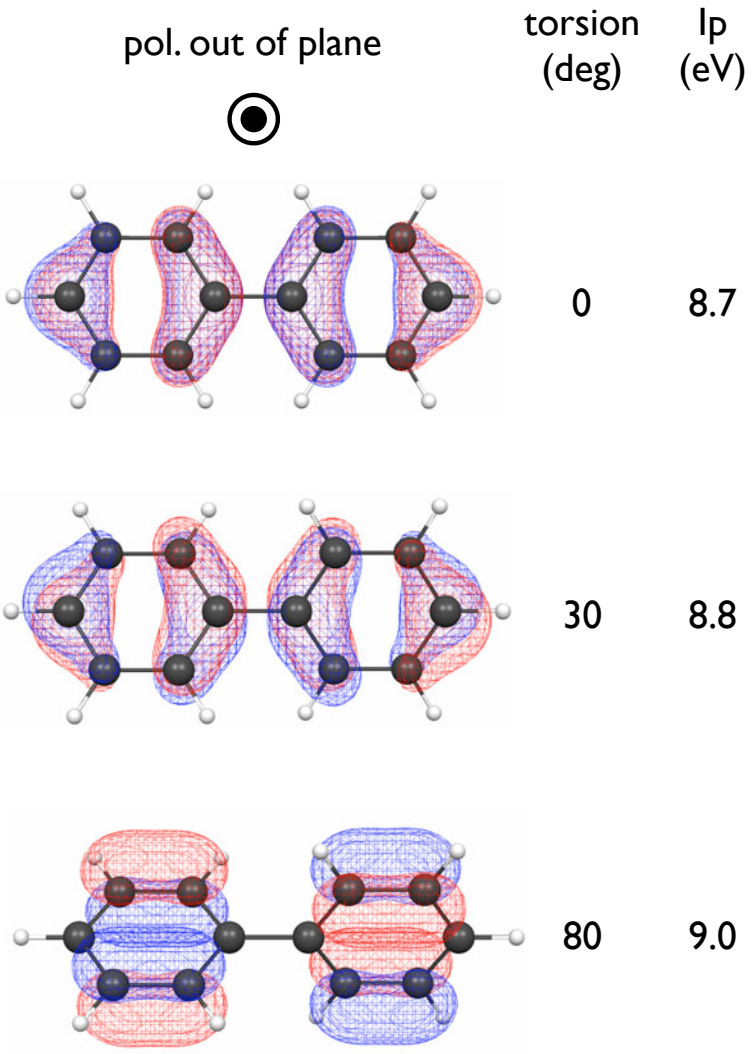

Figure 6.10: The HOMO wave function of biphenyl as a function of torsion. Different colors indicate different sign of the wave function. Also shown is the polarization axis of the linearly polarized laser used to calculate the HHG shown in figure 6.11. The last column lists the ionization potential, I_p, from the HOMO as a function of the torsional angle. The change of the ionization potential with torsion is small compared to the typical HHG driving laser photon energy ($\sim$ 1 eV), whereas the change of electronic structure is significant.

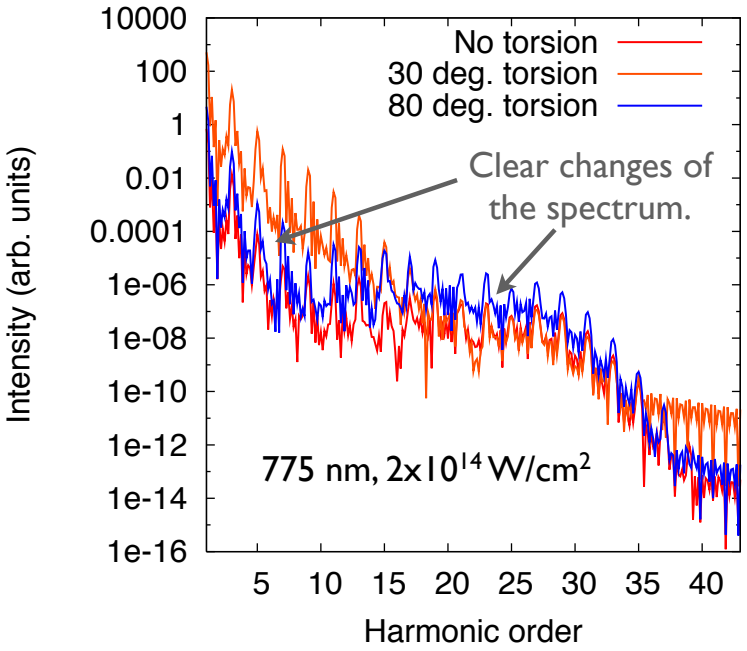

Figure 6.11: High-order harmonic spectrum for biphenyl as a function of the torsion for an 2×10^{14} W/cm^2, 775 nm laser field with a trapezoidal envelope consisting of three optical cycles turn-on and turn-off and five cycles constant amplitude. The position of the cutoff only has a small variation. This is in agreement with the small change of the ionization potential as a function of torsion mentioned in Fig. 6.10. According to the cutoff formula (Eq. (6.1)) the expected change of cutoff as a function of torsion is $\sim \Delta I_p/\hbar\omega_0 = 0.3$ eV/1.60 eV $= 0.19$ or less than a fifth of a harmonic order. However, the significant change of electronic structure as a function of torsion (see Fig. 6.10) is seen to give rise to a big change of the harmonics near the 9th harmonic order.

generation provides a sensitive, all-optical and ideally non-destructive way to measure torsion.

Chapter 7

HHG and the influence of molecular vibration

In this chapter we treat the effect of molecular vibration on the high-order harmonic generation. According to Chapter 5 high-order harmonic generation in molecular gases is accompanied by a vibrational wave packet in the molecular ion. We have expressed this wave packet in terms of Franck-Condon (FC) factors (defined as the square of the overlap integral between the vibrational wave functions of the neutral molecule and the ion, in their respective electronic states) and the accompanying time-dependent phases caused by the vibrational excitations. Franck-Condon factors and vibrational energies are available for a vast number of molecules or may be computed using standard approximations and technology from quantum chemistry (see Appendix B) and in these cases the influence of vibration is readily evaluated.

As we shall see, vibration is important in molecules that contain light atoms. In particular, we expect that nuclear motion takes place during the interaction with the short driving pulse for molecules with bound hydrogen atoms, including hydrogen molecules, but also other species such as water, methane or ethylene. Even for heavier molecules where the relaxed geometry of the cation is very different from the equilibrium geometry of the neutral molecule, e.g., oxygen, vibration turns out to have an effect. These findings have been confirmed by others [70].

7.1 The basics of vibration in HHG

An interpretation of the vibrational factor (5.7) is straightforward: As the molecule is ionized the ground vibrational state of the molecule suddenly experiences the potential energy surface corresponding to the cation, and thus is no longer an eigenstate. Instead, it can be viewed as a superposition of the vibrational eigenstates of the molecular ion. The amplitude of each term is the overlap of the initial vibrational state with the ion vibrational eigenstate or in other words the FC amplitude. As a result, the continuum electron wave packet is accompanied by a vibrational wave packet motion that

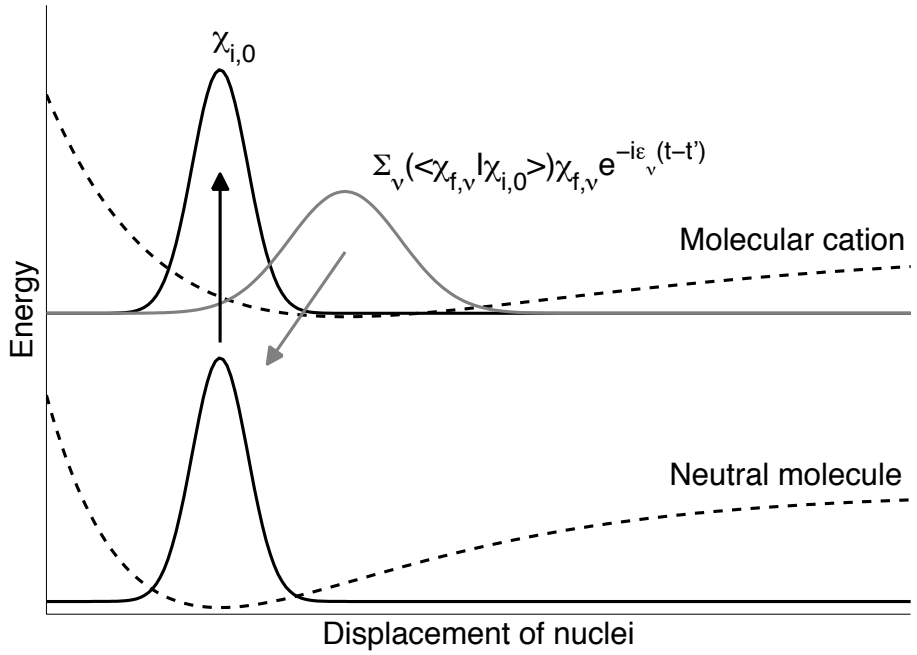

Figure 7.1: Simple sketch of the effect of vibration on HHG. When the molecule ionizes the laser launches a vibrational wave packet that evolves on the ionic Born-Oppenheimer surface. The overlap of this wave packet and the initial vibrational state (see Eq. (5.7)) weights the dipole velocity (see Eq. (5.6)) and hence the HHG signal.

evolves from the instant of ionization, t', to the moment of recombination, t: $\sum_{\boldsymbol{\nu}}(\langle\chi_{f,\boldsymbol{\nu}}|\chi_{i,0}\rangle)\chi_{f,\boldsymbol{\nu}}e^{-i\epsilon_{\boldsymbol{\nu}}(t-t')}$. The recombination probability amplitude will then be proportional to the overlap of the vibrational wave packet with the initial ground vibrational state of the molecule. The principle is illustrated in Fig. 7.1.

The period of an optical cycle of the laser field yields an estimate of the characteristic time difference $t - t'$ entering Eq. (5.7), since the electron is typically launched into the continuum within one half of an optical cycle and is driven back to recombine with the molecular ion within the other half. For an 800 nm harmonic-generating laser the time difference is of the order femtoseconds, and we infer that the harmonic spectrum contains information about the vibrational motion on a femtosecond time scale. On the other hand, vibration will only be of importance if the vibrational correlation function changes appreciably within a few femtoseconds. This amounts to saying that the nuclei must be light so that a broad range of ionic vibrational levels, separated by only small energies, are populated.

Based on the picture presented above it was predicted that HHG may be used to probe the fast nuclear motion in H_2 by comparing the HHG spectrum

to that of the isotope D_2 [45], and this was soon after confirmed in a pioneering experiment [17]. The D_2/H_2 ratio of the harmonic spectra is an increasing function of the harmonic order which can be understood from the basic idea that the harmonic order is associated with the time the electron spends in the continuum from initial ionization to recombination. The larger this time is, the higher the harmonic order. The reason for the observed increase is the faster nuclear motion in the lighter isotope H_2, leading to a smaller overlap of the nuclear wave packets in the recombination step. In the experiment [17] similar results were reported for HHG from methane isotopes (CD_4/CH_4).

7.2 Tracing nuclear reconfiguration of methane with HHG

In this section we investigate how the nuclear motion affects HHG from CH_4 and CD_4 when these molecules are driven by linearly polarized laser field (defining the LF X axis). The field contains a trapezoidal envelope with a carrier wavelength of 775 nm and is made up of two optical cycles, linear turn-on and turn-off, and three cycles of constant amplitude corresponding to peak intensity of 2×10^{14} W/cm^2. The model we use here for Methane allows us to identify the two most important modes for vibrational relaxation out of the possible nine. These important modes turn out to promote a $T_d \leftrightarrow C_{2v}$ nuclear geometry reconfiguration [see, e.g., Ref. [71] for a discussion of point group symmetry].

7.2.1 Structure of methane

We begin by determining the electronic structure and the FC factors which are used to calculate the harmonic yields. The configuration of the molecular orbitals is found to be $(1a_1)^2(2a_1)^2(3t_2)^6$ using GAMESS. We see there are six electrons distributed among three degenerate HOMOs (see Fig. 7.2) that could all contribute appreciably to the harmonic yield. To obtain the adiabatic ionization potential, we have compared the total energy of the methane to that of the relaxed methane ion and reached a value of $I_p = 12.92$ eV. We then obtain the effective ionization potential by adding the additional shifts ($\epsilon_{\boldsymbol{\nu}}$) due to vibrational excitation. The results of the FC analysis indicate that only two normal modes are excited when CH_4 (CD_4) ionizes. These modes include an E symmetry mode ($\omega \approx 1295$ cm^{-1} for CH_4^+; $\omega \approx 920$ cm^{-1} for CD_4^+) that brings the molecule towards a plane and an A_1 symmetry mode ($\omega \approx 2766$ cm^{-1} for CH_4^+; $\omega \approx 1960$ cm^{-1} for CD_4^+) that correspond to changes of the C−H (C−D) bond lengths. In Fig. 7.3 the one-dimensional FC factors for both modes are depicted along with insets indicating the nuclear rearrangements related to each normal mode. These modes are calculated from integrals over a single mode as explained in Appendix B. Further, these modes drive the molecular ion into the relaxed C_{2v} symmetry.

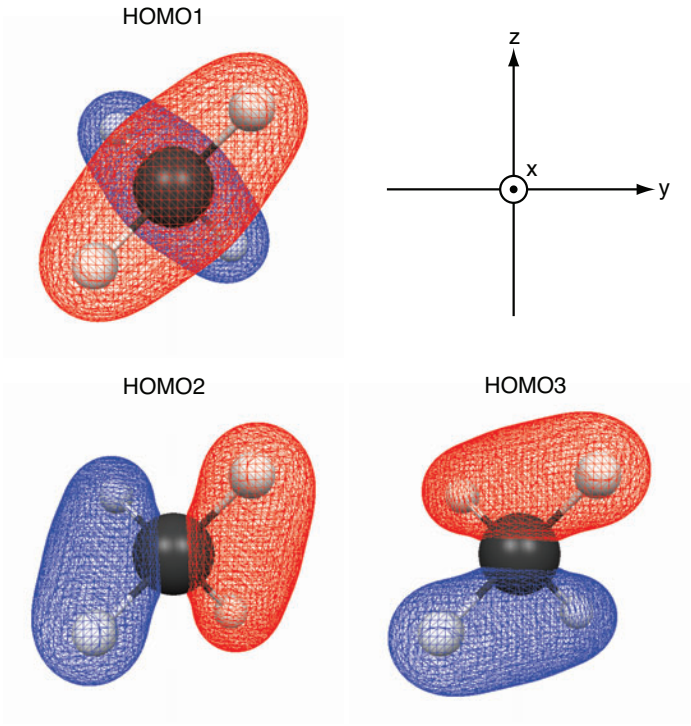

Figure 7.2: Isocontour plots of the degenerate HOMO wave functions of methane with the different colors indicating different signs of each wave function. Directions of the MF coordinate axes are shown. We calculate HHG yields with the linear laser field polarization along the x axis and include only the contribution from HOMO1 as this contribution dominates the total yield.

7.2.2 High-order harmonic spectra and nuclear motion

We have now obtained the molecular structure including the molecular orbitals and FC factors. The next step, in principle, is to calculate the molecular dipole velocity as given in Eq. (5.6) for different orientations of the molecule and for each of the (degenerate) orbitals and average the resulting dipole velocities. But, the methane molecule possesses high symmetry which indicates the harmonic yield only has a small angular dependence. Further, the yield is dominated by the contribution from a single orbital that couples strongly to the linearly polarized laser field. This has been verified by calculations for various orientations not shown here. Consequently, the averaging of the dipole velocities is redundant and the results presented here are carried out for one fixed orientation of the molecule and include only the yield of the dominant orbital (cf. Fig. 7.2). Additionally, we limit the t' integral in Eq. (5.6) to times when $\tau = t - t'$ is smaller than 0.65 times an optical cycle. We do this to have a one-to-one correspondence between the time the electron spends in the continuum (from the instant ionization, t', to the moment of recombination, t) and the harmonic order, i.e., the energy released when the electron

recombines [45].

The harmonic spectra of CH_4 and CD_4 are shown in Figure 7.4. Initially it is difficult to see the difference in the spectra for the two isotopes, but if we integrate the spectra in an interval around each (odd) harmonic order and plot the ratio of these numbers for the isotopes, we can more effectively compare the spectra. The result is shown in Fig. 7.5 by the dash-dotted curve. For comparison, we also plot the CD_4/CH_4 ratio of the vibrational correlation functions squared (see Eq. (5.7)) for three different cases. In one case we include only the dominant E symmetry mode (C_{E}), in another both the E and the A_1 symmetry mode ($C_{\mathrm{E+A_1}}$) and in the final case we include two slightly excited T_2 symmetry modes ($C_{\mathrm{E+A_1+T_2}}$). We see that the the major effect of nuclear motion is accounted for by E+A_1 motion. Since, the vibrational correlation functions are increasing monotonically we may also conclude that the oscillatory structure of the HHG ratio arises from the combined electron-nuclear dynamics.

7.2.3 Discussion of the the current treatment of nuclear motion

When the slope of the ratio predicted by the current theory is compared to measurements, it is found to be an underestimate [17]. Calculations carried out in more detail on the simpler systems H_2 and D_2 help us to understand this deviation. For these systems, we clearly understand the consequences of the approximations made here, and thus attribute the discrepancy to two factors. First, we expect that the harmonic approximation used here to retrieve the FC factors yields nuclear factors, $C(t-t')$, where the ratio between the isotopes is too low. This is because stretching of the molecule is underestimated when the asymmetry of the potential is not taken into account. To substantiate this claim we compared vibrational correlation functions resulting from FC factors based on the harmonic approximation to a more accurate Morse potential for H_2 and D_2 [72] and our reasoning is validated (see Fig. 7.6). Second, we have not included any coupling of nuclear and electron dynamics. In HHG from the isotopes H_2 and D_2 such coupling is known to result in a dynamic two-center interference effect that leads to a higher ratio in the D_2/H_2 spectrum [73].

The vibrational correlation function is expressed in terms of the FC factors (Eq. (5.7)). It is important to note that one may control the vibrational correlation function for systems where the weight on the different FC factors is effectively adjustable by preparation of the laser pulse. For example, this is the case in H_2 [74] and we have checked that by populating only FC factors $(0, \nu = 0)$ and $(0, \nu = 18)$ the vibrational correlation function oscillates with a period of 1.56 fs. It follows that the vibrational correlation function can be modulated within less than half an optical period of the typical HHG driving field (1.33 fs for an 800 nm field) and thereby drive enhancement and suppression of certain electron trajectories and associated harmonic orders. Controlling the relative strength of the harmonics is, for instance, useful for generating attosecond pulses [75]. The control scheme briefly discussed here

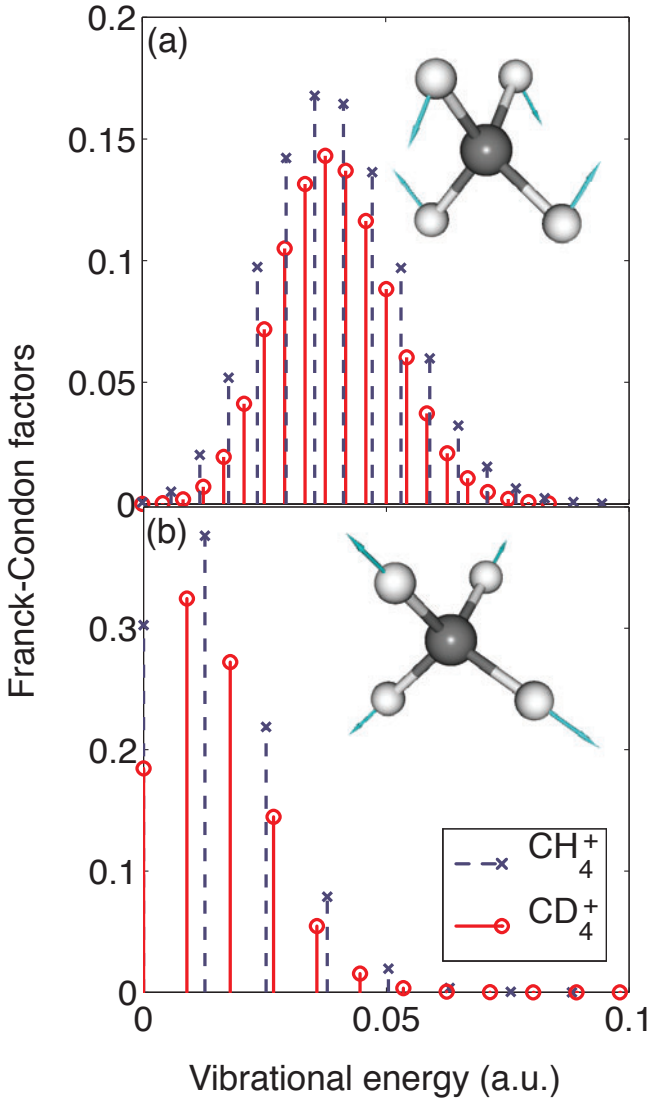

Figure 7.3: Franck-Condon factors for the two dominating modes in methane. The insets with molecular models and arrows indicate the the coordinates along which each of the modes vibrate. (a) shows the E mode and (b) the A_1 mode of CH_4^+ (dashed) and CD_4^+ (full). These two modes will drive the molecule from the tetrahedral T_d symmetry into the relaxed C_{2v} symmetry upon ionization as conjectured in [17].

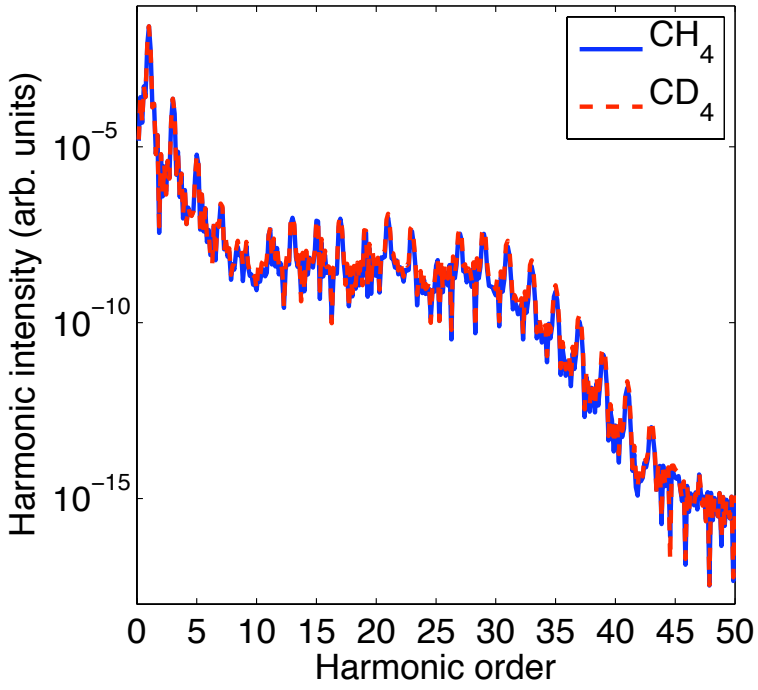

Figure 7.4: Harmonic spectra for CH_4 and CD_4 using a 775 nm linearly polarized laser of intensity 2×10^{14} W/cm^2 with the trapezoidal envelope made up of two optical cycles, linear turn-on and turn-off, and three cycles of constant amplitudes. Typical characteristics of harmonic spectra are illustrated by the curves in the figure including an exponential drop-off at low harmonic orders followed by a plateau with a cutoff around the harmonic order 33 in agreement with the cutoff formula (Eq. (6.1)).

is based on the intrinsic structure of the molecule.

Finally, since the vibrational correlation function is expressed in terms of one-dimensional FC factors, it is possible to identify the important part of the nuclear dynamics. This is done by studying how the vibrational correlation function changes as the different normal modes are gradually added.

7.3 The influence of nuclear motion on heavy molecules

For molecules that do not contain light atoms the effect of nuclear motion is less pronounced. However, it is not simply the mass of the atoms in the molecule that plays a role. Also the change in equilibrium geometry upon ionization is important. We illustrate this point below, where we compare the effect of nuclear motion on HHG from N_2 and the heavier O_2. We use the

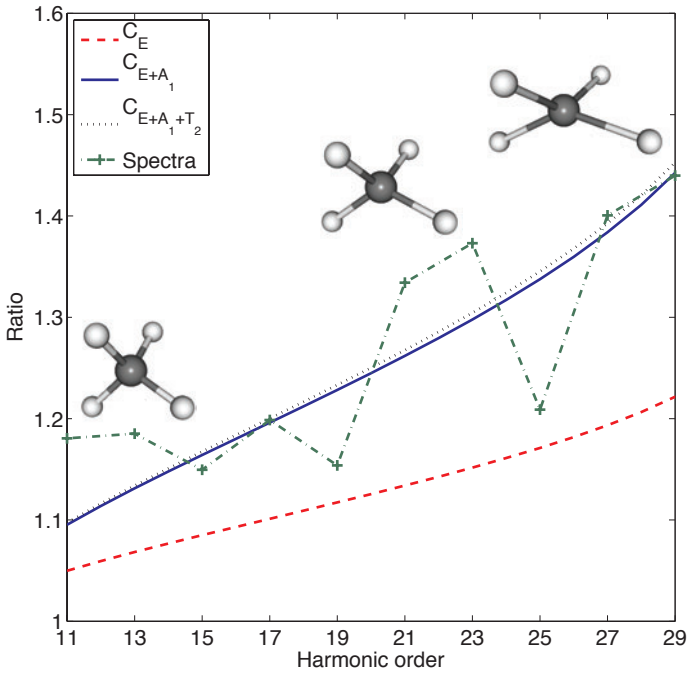

Figure 7.5: Curves displaying the ratio of the harmonic spectra from Fig. 7.4 (dash-dotted) and of the CD_4/CH_4 vibrational correlation functions (Eq. (5.7)) squared including normal modes of symmetry E (dashed), E and A_1 (full) and E and A_1 and T_2 (dotted).

Kuchiev-Ostrovsky model to calculate HHG with a linearly polarized 800 nm, 2×10^{14} W/cm^2 laser.

7.3.1 The N_2 molecule – negligible effect of nuclear motion

In the case of N_2 the FC factors and vibrational energies used are from Ref. [76]. Figure 7.7 shows the N_2 HHG spectrum in a geometry, where the internuclear axis of the molecule is aligned parallel to the polarization of the laser. There are three different curves on the figure. The dotted curve corresponds to Eq. (5.32), i.e., the case where the asymptotic wave function is used in both the ionization and recombination step of the HHG process. The dashed and solid curves correspond to Eq. (5.28) meaning that the improved wave function was employed in the LAR step. Calculations represented by the solid curve take nuclear motion into account.

The different forms of the HOMO wave function have been employed here to determine whether HHG is a phenomena that mainly probes the asymptotic region of the wave function or if the inner regions of the wave function

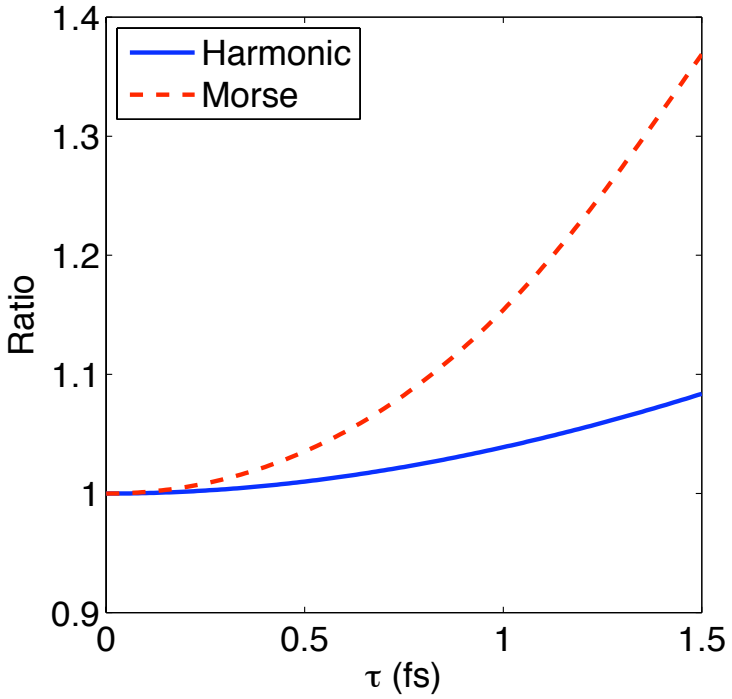

Figure 7.6: Ratio of the D_2/H_2 vibrational correlation function (Eq. (5.7)) squared for the harmonic approximation (solid) and the more accurate Morse potential (dashed)

are important. This question is answered by considering the fact that the harmonic spectrum of the N_2 molecule is different when the asymptotic wave function is used everywhere as compared to the case when the Gaussian wave function is employed in the recombination step. This result shows that the quality of the HOMO wave function is of importance.

It is also clear from Fig. 7.7 that the effect of nuclear motion in the case of N_2 is negligible. This is because the BO potential energy curves of the N_2 molecule and the N_2^+ molecular ion are nearly parallel, which means that ionization of an N_2 molecule in the ground state always leaves the residual molecular N_2^+ ion in the vibrational ground state of the cation.

7.3.2 The O_2 molecule – significant effect of nuclear motion

We next consider the O_2 molecule, which has a HOMO with π_g symmetry. In this case the FC factors and energies have been found from Ref. [77]. The laser parameters are the same as in the preceding subsection. Figure 7.9 shows the relative HHG spectrum assuming an angle of 36° between the internuclear axis and the polarization axis of the laser. The O_2 HOMO has nodal planes at 0 and 90° (see Fig. 7.8) and the HHG signal will vanish at these angles

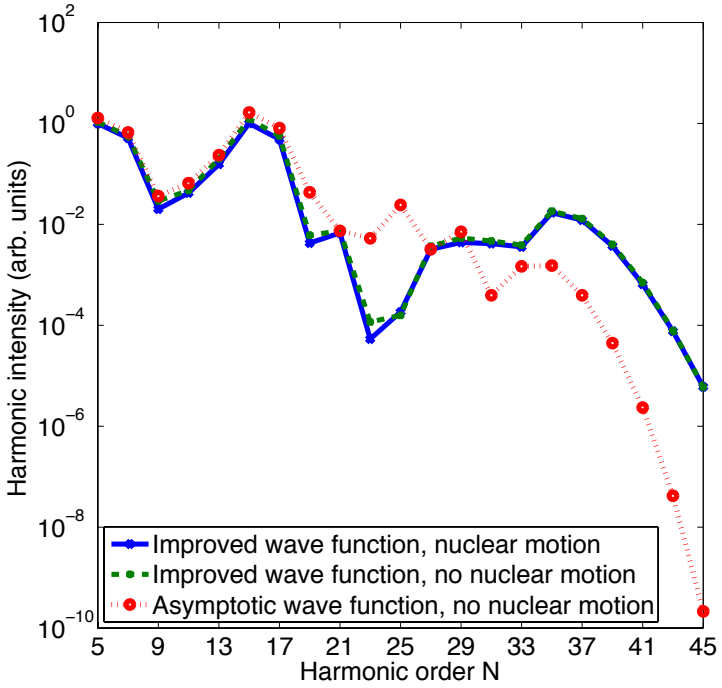

Figure 7.7: Calculated HHG from the N_2 molecule. We have used an 800 nm continuos wave laser with an intensity of 2×10^{14} W/cm^2 and linearly polarized parallel to the internuclear axis. We compare results with the asymptotic HOMO wave function used in both the recombination and the ionization step and in the ionization step only (improved wave function). Only the solid curve includes nuclear motion. The effect of nuclear motion is seen to be negligible in the case of N_2.

within the Kuchiev-Ostrovsky model. As in the case of N_2 it is important to use a better wave function than the asymptotic one in the recombination step. The effect of nuclear motion is more pronounced than for the N_2 molecule, because the Franck-Condon distribution of O_2 is broader than that of the N_2 molecule. Physically, this is due to the fact that the equilibrium geometry changes a lot upon ionization.

7.4 The potential for using HHG to probe nuclear dynamics in ethylene

An interesting molecule where FC factors are known is ethylene, C_2H_4 [78]. As in the case of methane, the FC distribution is broad which again leads to a rapidly varying vibrational correlation function. This is shown in Fig. 7.10.

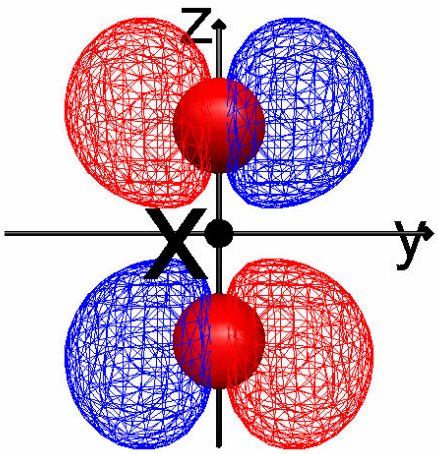

Figure 7.8: Isocontour plot of the π_g HOMO wave function of O_2, where different colors indicates different sign of the wave function.

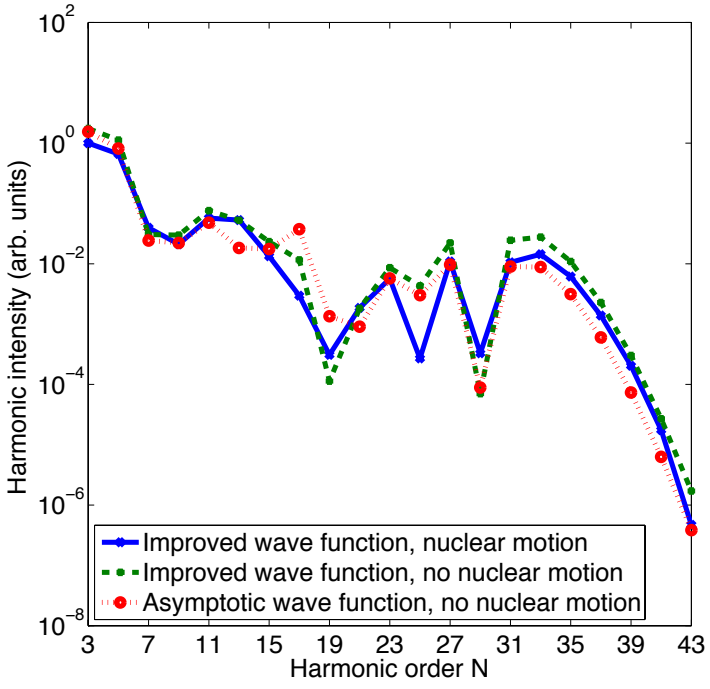

Figure 7.9: High-order harmonic generation from the O_2 molecule. See Fig. 7.7 for details on laser parameters and the meaning of the three curves. The internuclear axis is oriented at an angle $\beta = 36°$ with respect to the laser polarization axis, because the internuclear axis coincides with a nodal plane of the O_2 (see Fig. 7.8). There is an observable effect of nuclear motion.

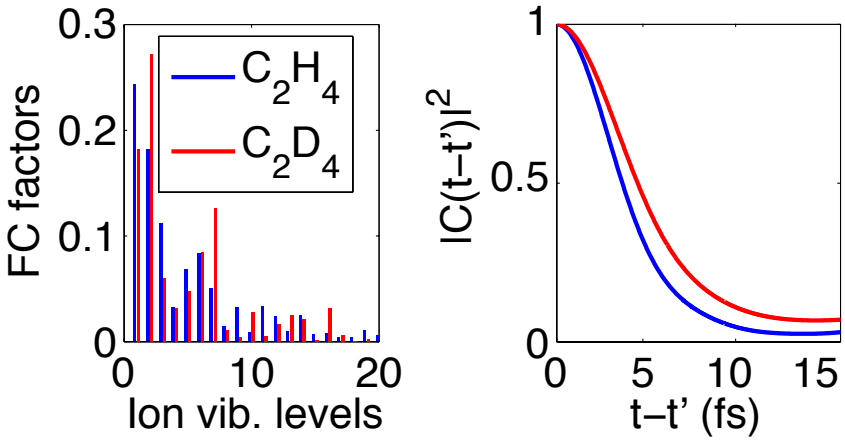

Figure 7.10: Franck-Condon factors and the resulting vibrational correlation functions squared for ethylene molecule (C_2H_4) along with the isotope. Note how the correlation function of the heavier isotope changes more slowly consistent with an increase in the ratio as seen in Fig. 7.6.

Consequently, if experimentalists measured HHG from ethylene and its isotope C_2D_4 and compared the ratio of the harmonic spectra the effect of nuclear motion should be clear.

Ethylene and related systems are very interesting from the point of view that some probes of the nuclear motion have already been carried out. Reference [79] reports that after excitation of the ethylene cation by $20 - 25$ eV photons $(H_2C{-}CH_2)^+$ the molecular ion experienced isomerization to the ethylidene configuration $(HC\text{-}CH_3)^+$ in 50 ± 25 fs, followed by an H_2 stretch motion. By the observation of different fragments, the group speculated about transient configurations. It would be interesting to see, if HHG can be used provide an efficient probe to explore the transient configurations and map the hydrogen migration with time resolution.

7.5 Summary

In this chapter we studied the influence of vibration on high-order harmonic generation. Vibration enters as a weight on the time-dependent dipole velocity that tends to suppress the harmonic signal from light molecules, because the weight function decreases rapidly. The weight function is related to Franck-Condon factors. We saw how molecules such as methane and ethylene containing light hydrogen atoms have a strong trace of nuclear motion in the harmonic signal. Even further, the much heavier O_2 molecule is affected by nuclear motion, because the equilibrium geometries of the neutral molecule and the cation deviate considerably from one another.

Chapter 8

Laser induced alignment and orientation

Gaining control over the external and the internal degrees of freedom of molecules is of great interest for a range of areas in molecular science. One approach, dating as far back as the 1920s [80, 81], relies on the application of inhomogenous (static or low frequency) magnetic and electric fields. This has proven most useful for controlling the full three-dimensional motion of molecules, including control of the velocity distribution, bringing molecules to a stand still, storing them for extended periods of times and trapping them in a confined volume [82].

An alternative and complementary approach relies on the use of non-resonant, non-ionizing laser fields typically supplied by pulsed lasers. Many studies during the last decade have shown that strong non-resonant laser fields can effectively manipulate the external degrees of freedom of isolated gas phase molecules. The manipulation results from laser-induced forces and torques due to the interaction between the induced dipole moment and the laser field itself. Examples of manipulation include deflection [83], focusing [84] and slowing [85] of molecules through the dependence of the non-resonant polarizability interaction on the intensity distribution in a laser focus. Likewise, the dependence of the induced dipole interaction on molecular orientation has proven highly useful for controlling the rotation of a variety of molecules [12]. In particular, the molecules can be sharply confined with respect to axes that are fixed in the laboratory. This is known as laser induced alignment.

In this chapter we will provide an introduction to laser induced alignment on a qualitative and quantum mechanical level.

8.1 The principle of laser induced alignment

To begin, let us specify what we mean by alignment and orientation. *Alignment* refers to the confinement of the internuclear axes of molecules with respect to a laboratory fixed frame, whereas *orientation* further implies the breaking of inversion symmetry. These concepts are illustrated in Fig. 8.1.

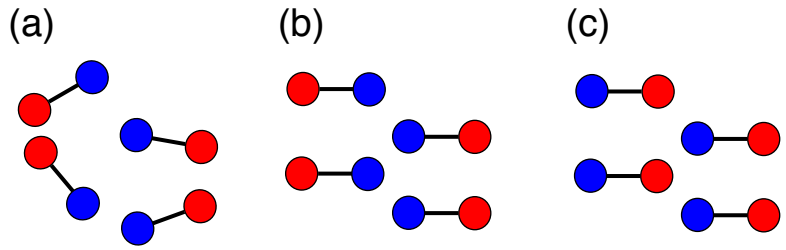

Figure 8.1: Alignment and orientation illustrated with an ensemble of heteronuclear diatomic molecules: (a) Unaligned, (b) aligned, and (c) oriented.

To understand the laser-molecule interaction that leads to molecular alignment it is useful to start from a macroscopic point of view. In general, when the molecule is exposed to an external, non-ionizing electric field, it is polarized and a dipole moment is induced. As the molecular structure is anisotropic, the molecule may polarize more readily in some directions than others, and consequently the induced dipole moment need not be along the direction of the electric field, but is more generally related linearly to the applied electric field through the *polarizability tensor*.[1] Along with the permanent dipole, the induced dipole interacts with the external electric field and causes the molecule to rotate into a position that minimizes the energy of the dipole in the electric field. Now, the electric field of the laser is oscillating on a femtosecond time scale, whereas it will take picoseconds or more for the molecule to change its orientation, and therefore the interaction terms should be averaged over several laser cycles. This implies that the interaction of the field with the permanent dipole vanishes, as the electric field changes sign every half cycle. The polarizability, on the other hand, changes its sign along with the field, and therefore the interaction term containing the polarizability does not average out. As a result the alignment dynamics of the molecule in the laser field are determined by the polarizability.

In order to handle the alignment interaction on a microscopic level, one must derive an effective description of the electronic response to the laser field. We shall only be concerned with cases when the laser frequency is far off resonance with any energy levels of the molecule. In this case, a direct dipole coupling between molecular states is negligible and instead the dominant interaction is a Raman coupling of neighboring molecular eigenstates in the electronic ground state through the molecular levels of the excited electronic states (see Fig. 8.2). These latter electronic states can be adiabatically eliminated by integrating out their motion and introducing their influence as a polarizability tensor. This interaction then leads to alignment by transferring an initial rotational state with ill-defined angular confinement into an angularly confined superposition of molecular levels in the electronic ground state.

[1] In principle, part of the induced dipole moment could depend nonlinearly on the electric field. We will not be concerned with the resulting higher order terms of the interaction.

8.2 Quantum mechanical description

We now transfer the qualitative picture given above to a quantitative level. We will closely follow the approach of Ref. [86]. Our starting point is the time-dependent Schrödinger Equation (for the sake of clarity we will not use atomic units in this derivation)

$$i\hbar\frac{\partial}{\partial t}\Psi(\Omega,\boldsymbol{R};\boldsymbol{r},t) = (H_0 + V(t))\Psi(\Omega,\boldsymbol{R};\boldsymbol{r},t). \tag{8.1}$$

The interaction between the quantum system and the laser light in the length gauge reads

$$V(t) = -\boldsymbol{d}\cdot\boldsymbol{F}(t) \tag{8.2}$$

with $\boldsymbol{d} = -e\sum_n \boldsymbol{r}_n$ the electric dipole operator, e the elementary charge.[2]

Using Euler's formula, we rewrite the laser electric field of Eq. (2.9) as

$$\boldsymbol{F}(t) = \frac{1}{2}\boldsymbol{e}F_0 h(t)(e^{i\omega_0 t} + c.c.), \tag{8.3}$$

Similar to Chapter 4, the molecule is initially in a time-independent thermal state and we project this on field-free energy eigenstates $\psi_{\boldsymbol{\alpha}_0}$ with energy $E_{\boldsymbol{\alpha}_0}$, where $\boldsymbol{\alpha}_0 = (\xi_0, \boldsymbol{\nu}_0, \boldsymbol{n}_0)$ denotes the state of the molecule through electronic ξ_0, vibrational $\boldsymbol{\nu}_0$ and rotational $\boldsymbol{n}_0$ indices. This state then evolves according to Eq. (8.1). At any time we may expand the resulting wave packet onto the field-free states as these form a complete set,

$$\Psi_{\boldsymbol{\alpha}_0}(\Omega,\boldsymbol{R};\boldsymbol{r},t) = \sum_{\boldsymbol{\alpha}'} c_{\boldsymbol{\alpha}'}(t)e^{-iE_{\boldsymbol{\alpha}'}t/\hbar}\psi_{\boldsymbol{\alpha}'}(\Omega,\boldsymbol{R};\boldsymbol{r},0). \tag{8.4}$$

If we project this expansion onto a specific field-free state, $\psi_{\boldsymbol{\alpha}}(\Omega,\boldsymbol{R};\boldsymbol{r},0)$ we get an expression for the time-dependent coefficient

$$i\hbar\frac{d}{dt}c_{\boldsymbol{\alpha}}(t) = \sum_{\boldsymbol{\alpha}'} V(\boldsymbol{\alpha}|\boldsymbol{\alpha}';t)e^{iE(\boldsymbol{\alpha}|\boldsymbol{\alpha}')t/\hbar}c_{\boldsymbol{\alpha}'}(t). \tag{8.5}$$

Here, $E(\boldsymbol{\alpha}|\boldsymbol{\alpha}') = E_{\boldsymbol{\alpha}} - E_{\boldsymbol{\alpha}'}$ denotes the energy difference between the field-free states and $V(\boldsymbol{\alpha}|\boldsymbol{\alpha}';t) = \langle\psi_{\boldsymbol{\alpha}}(0)|V(t)|\psi_{\boldsymbol{\alpha}'}(0)\rangle$ describes the coupling between states via the laser field.

The laser coupling between states depends on the field strength of the laser, but also on the frequency. If the laser frequency is tuned near an electronic resonance, the coupling will be strong and a significant part of the total population is moved. In this case, one may use a two-level approximation. Here, we are concerned with the situation where the frequency is far-detuned from vibronic transition frequencies. Then, a specific excited state that dominates the interaction cannot be singled out and real population resides solely

[2] We should in principle use the total dipole moment operator including all electrons and all nuclei. As explained in Chapter 4, however, the larger mass of the nuclei justifies that we include only the electronic part.

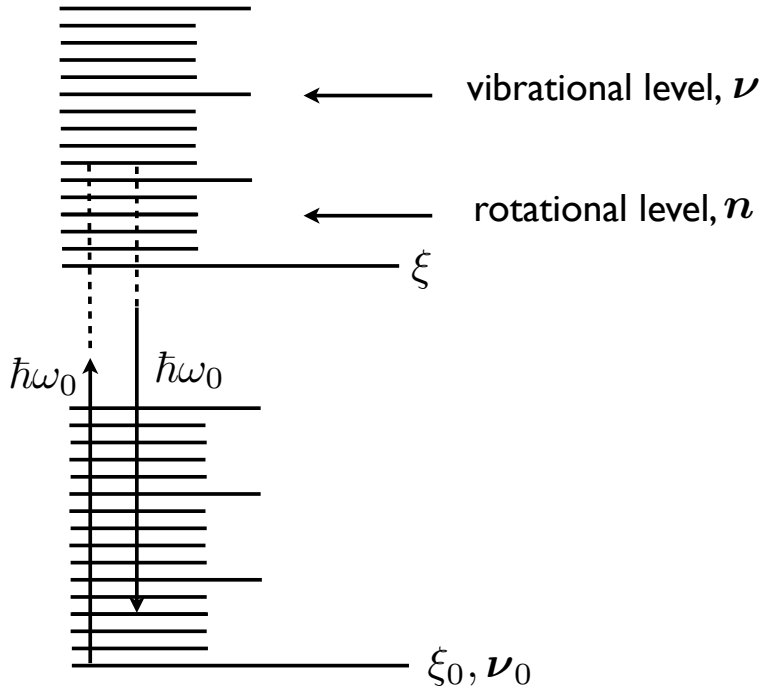

Figure 8.2: Transitions between the levels in the rotational states of the initial vibronic manifold $\{\xi_0, \boldsymbol{\nu}_0\}$ are mediated by far off-resonance (Raman) transitions via the rotational states of other vibronic manifolds. The role of the latter states is effectively described via the dynamic polarizability as explained in the text.

in the initial vibronic manifold, $\{\xi_0, \boldsymbol{\nu}_0\}$. With this in mind we rewrite the expansion of the wave packet from Eq. (8.4) as

$$\Psi_{\boldsymbol{n}}^{\xi_0,\boldsymbol{\nu}_0}(\Omega, \boldsymbol{R}; \boldsymbol{r}, t) = \sum_{\boldsymbol{n}'} c_{\boldsymbol{n}'}^{\xi_0,\boldsymbol{\nu}_0}(t) e^{-iE_{\boldsymbol{n}'}^{\xi_0,\nu_0} t/\hbar} \psi_{\boldsymbol{n}'}^{\xi_0,\boldsymbol{\nu}_0}(\Omega, \boldsymbol{R}; \boldsymbol{r}, 0) + \sum_{\xi,\boldsymbol{\nu},\boldsymbol{n}'} c_{\boldsymbol{n}'}^{\xi,\boldsymbol{\nu}}(t) e^{-iE_{\boldsymbol{n}'}^{\xi,\boldsymbol{\nu}} t/\hbar} \psi_{\boldsymbol{n}'}^{\xi,\boldsymbol{\nu}}(\Omega, \boldsymbol{R}; \boldsymbol{r}, 0). \tag{8.6}$$

We partitioned the sum into the rotational states within the initial vibronic manifold $\{\xi_0, \boldsymbol{\nu}_0\}$ that are significantly populated and the rotational states within other vibronic manifolds, $\{\xi, \boldsymbol{\nu}\}$, that will be negligibly populated. The latter states merely mediate dynamics through the couplings with the rotational states of the initial vibronic state (see Fig. 8.2). We will now eliminate them to get an effective Hamiltonian that refers only to the rotational states of the initial vibronic manifold. For the rotational states in vibronic

manifolds different from the initial one, we have

$$i\hbar\frac{d}{dt}c_{\boldsymbol{n}}^{\xi,\boldsymbol{\nu}}(t) = \sum_{\boldsymbol{n}'} V(\xi,\boldsymbol{\nu},\boldsymbol{n}|\xi_0,\boldsymbol{\nu}_0,\boldsymbol{n}';t)e^{iE(\xi,\boldsymbol{\nu},\boldsymbol{n}|\xi_0,\boldsymbol{\nu}_0,\boldsymbol{n}')t/\hbar}c_{\boldsymbol{n}'}^{\xi_0,\boldsymbol{\nu}_0}(t) + \sum_{\xi',\boldsymbol{\nu}',\boldsymbol{n}'} V(\xi,\boldsymbol{\nu},\boldsymbol{n}|\xi',\boldsymbol{\nu}',\boldsymbol{n}';t)e^{iE(\xi,\boldsymbol{\nu},\boldsymbol{n}|\xi',\boldsymbol{\nu}',\boldsymbol{n}')t/\hbar}c_{\boldsymbol{n}'}^{\xi',\boldsymbol{\nu}'}(t). \quad (8.7)$$

We assume that there is initially no population of any rotational states other than those belonging to the initial vibronic manifold. If we further assume that all couplings are mediated by rotational states within the initial vibronic manifold, the above equation may be integrated to yield

$$c_{\boldsymbol{n}}^{\xi,\boldsymbol{\nu}}(t) = -\frac{i}{\hbar}\int_{-\infty}^{t}\sum_{\boldsymbol{n}'} dt'\, V(\xi,\boldsymbol{\nu},\boldsymbol{n}|\xi_0,\boldsymbol{\nu}_0,\boldsymbol{n}';t')e^{iE(\xi,\boldsymbol{\nu},\boldsymbol{n}|\xi_0,\boldsymbol{\nu}_0,\boldsymbol{n}')t'/\hbar}c_{\boldsymbol{n}'}^{\xi_0,\boldsymbol{\nu}_0}(t'). \quad (8.8)$$

The main contribution to the amplitude comes from the terms that are not rapidly oscillating. To identify these terms, we need to write out the coupling matrix involving the laser

$$\begin{aligned} V(\xi,\boldsymbol{\nu},\boldsymbol{n}|\xi_0,\boldsymbol{\nu}_0,\boldsymbol{n}';t') &= \langle\psi_{\boldsymbol{n}}^{\xi,\boldsymbol{\nu}}(t')|V(t')|\psi_{\boldsymbol{n}'}^{\xi_0,,\boldsymbol{\nu}_0}(t')\rangle \\ &= \frac{1}{2}\boldsymbol{d}(\xi,\boldsymbol{\nu},\boldsymbol{n}|\xi_0,\boldsymbol{\nu}_0,\boldsymbol{n}')\cdot\boldsymbol{e}F_0h(t')e^{i\omega_0t'} + [\omega_0\rightarrow-\omega_0] \end{aligned} \quad (8.9)$$

with $\boldsymbol{d}(\xi,\boldsymbol{\nu},\boldsymbol{n};\xi_0,\boldsymbol{\nu}_0,\boldsymbol{n}') = \langle\psi_{\boldsymbol{n}}^{\xi,\boldsymbol{\nu}}(0)|\boldsymbol{d}|\psi_{\boldsymbol{n}'}^{\xi_0,\boldsymbol{\nu}_0}(0)\rangle$. Substitution of Eq. (8.9) into Eq. (8.8) and integration by parts yields

$$\begin{aligned} c_{\boldsymbol{n}}^{\xi,\boldsymbol{\nu}}(t) = -\frac{1}{2}\sum_{\boldsymbol{n}'}\Bigg(&\frac{e^{i(E(\xi,\boldsymbol{\nu},\boldsymbol{n}|\xi_0,\boldsymbol{\nu}_0,\boldsymbol{n}')+\hbar\omega_0)t/\hbar}}{E(\xi,\boldsymbol{\nu},\boldsymbol{n}|\xi_0,\boldsymbol{\nu}_0,\boldsymbol{n}')+\hbar\omega_0} \\ &\times\boldsymbol{d}(\xi,\boldsymbol{\nu},\boldsymbol{n}|\xi_0,\boldsymbol{\nu}_0,\boldsymbol{n}')\cdot\boldsymbol{e}F_0h(t)c_{\boldsymbol{n}'}^{\xi_0,\boldsymbol{\nu}_0}(t) \\ &-\int_{-\infty}^{t}dt'\frac{e^{i(E(\xi,\boldsymbol{\nu},\boldsymbol{n}|\xi_0,\boldsymbol{\nu}_0,\boldsymbol{n}')+\hbar\omega_0)t'/\hbar}}{E(\xi,\boldsymbol{\nu},\boldsymbol{n}|\xi_0,\boldsymbol{\nu}_0,\boldsymbol{n}')+\hbar\omega_0} \\ &\times\boldsymbol{d}(\xi,\boldsymbol{\nu},\boldsymbol{n}|\xi_0,\boldsymbol{\nu}_0,\boldsymbol{n}')\cdot\boldsymbol{e}F_0\frac{d}{dt'}[h(t')c_{\boldsymbol{n}'}^{\xi_0,\boldsymbol{\nu}_0}(t')]\Bigg) \\ &+[\omega_0\rightarrow-\omega_0] \end{aligned} \quad (8.10)$$

It is readily seen that further integration by parts gives rise to a series in higher derivatives $(d/dt')^s, s = 0,1,2,\ldots$ of the product $h(t')c_{\boldsymbol{n}'}^{\xi_0,\boldsymbol{\nu}_0}(t')$. If the envelope, $h(t')$ is slowly varying on the timescale of the field oscillations the product $h(t')c_{\boldsymbol{n}'}^{\xi_0,\boldsymbol{\nu}_0}(t')$ will also be slowly varying, and it is a good approxima-

tion to only include the $s = 0$ term in the above expression. Hence,

$$c_{\boldsymbol{n}}^{\xi,\boldsymbol{\nu}}(t) = -\frac{1}{2}\sum_{\boldsymbol{n}'} e^{iE(\xi,\boldsymbol{\nu},\boldsymbol{n}|\xi_0,\boldsymbol{\nu}_0,\boldsymbol{n}')t/\hbar}\Bigg(\frac{e^{i\omega_0 t}}{E(\xi,\boldsymbol{\nu},\boldsymbol{n}|\xi_0,\boldsymbol{\nu}_0,\boldsymbol{n}') + \hbar\omega_0} \times \boldsymbol{d}(\xi,\boldsymbol{\nu},\boldsymbol{n}|\xi_0,\boldsymbol{\nu}_0,\boldsymbol{n}')\cdot\boldsymbol{e}F_0 h(t) + [\omega_0 \to -\omega_0]\Bigg) c_{\boldsymbol{n}'}^{\xi_0,\boldsymbol{\nu}_0}(t'). \tag{8.11}$$

This amplitude relates the rotational states in the initial vibronic manifold to the rotational states in the remaining vibronic manifolds.

The amplitudes of the rotational states in the initial vibronic manifold are obtained from

$$\begin{aligned} i\hbar\frac{d}{dt}c_{\boldsymbol{n}}^{\xi_0,\boldsymbol{\nu}_0}(t) &= \sum_{\boldsymbol{n}'} V(\xi_0,\boldsymbol{\nu}_0,\boldsymbol{n}|\xi_0,\boldsymbol{\nu}_0,\boldsymbol{n}';t)e^{iE(\xi_0,\boldsymbol{\nu}_0,\boldsymbol{n}|\xi_0,\boldsymbol{\nu}_0,\boldsymbol{n}')t/\hbar}c_{\boldsymbol{n}'}^{\xi_0,\boldsymbol{\nu}_0}(t) \\ &\quad + \sum_{\xi',\boldsymbol{\nu}',\boldsymbol{n}'} V(\xi_0,\boldsymbol{\nu}_0,\boldsymbol{n}|\xi',\boldsymbol{\nu}',\boldsymbol{n}';t)e^{iE(\xi_0,\boldsymbol{\nu}_0,\boldsymbol{n}|\xi',\boldsymbol{\nu}',\boldsymbol{n}')t/\hbar}c_{\boldsymbol{n}'}^{\xi',\boldsymbol{\nu}'}(t). \end{aligned} \tag{8.12}$$

In this summation over the rotational manifold the first term represents the direct dipole coupling between different states in the initial vibronic state. For systems such as homonuclear molecules only the dipole between different electronic states will be non-vanishing and the dipole coupling vanishes. In general, this term expands into two terms oscillating with frequencies $E(\xi_0,\boldsymbol{\nu}_0,\boldsymbol{n}|\xi_0,\boldsymbol{\nu}_0,\boldsymbol{n}')/\hbar \pm \omega_0$. We have assumed a far off-resonance laser (cf. Fig. 8.2) and therefore $|E(\xi_0,\boldsymbol{\nu}_0,\boldsymbol{n}|\xi_0,\boldsymbol{\nu}_0,\boldsymbol{n}')| \ll \hbar\omega_0$. Thus, we discard the direct dipole coupling term, since it will be rapidly oscillating. We thereby arrive at

$$\begin{aligned} i\hbar\frac{d}{dt}c_{\boldsymbol{n}}^{\xi_0,\boldsymbol{\nu}_0}(t) &= \sum_{\xi',\boldsymbol{\nu}',\boldsymbol{n}'} V(\xi_0,\boldsymbol{\nu}_0,\boldsymbol{n}|\xi',\boldsymbol{\nu}',\boldsymbol{n}';t)e^{iE(\xi_0,\boldsymbol{\nu}_0,\boldsymbol{n}|\xi',\boldsymbol{\nu}',\boldsymbol{n}')t/\hbar}c_{\boldsymbol{n}'}^{\xi',\boldsymbol{\nu}'}(t) \\ &= \sum_{\boldsymbol{n}'} V_{\mathrm{pol}}(\xi_0,\boldsymbol{\nu}_0,\boldsymbol{n}|\xi_0,\boldsymbol{\nu}_0,\boldsymbol{n}';t)e^{iE(\xi_0,\boldsymbol{\nu}_0,\boldsymbol{n}|\xi_0,\boldsymbol{\nu}_0,\boldsymbol{n}')t/\hbar}c_{\boldsymbol{n}'}^{\xi_0,\boldsymbol{\nu}_0}(t). \end{aligned} \tag{8.13}$$

In the second line above we substituted the expression from Eq. (8.11) for $c_{\boldsymbol{n}'}^{\xi',\boldsymbol{\nu}'}$ to obtain a closed set of equations involving only the amplitudes of rotational states in the initial vibronic manifold. We note that $V(\xi_0,\boldsymbol{\nu}_0,\boldsymbol{n}|\xi',\boldsymbol{\nu}',\boldsymbol{n}')$ and $c_{\boldsymbol{n}'}^{\xi',\boldsymbol{\nu}'}$ contain two terms proportional to the dipole moment $\boldsymbol{d}(\xi_0,\boldsymbol{\nu}_0,\boldsymbol{n}|\xi',\boldsymbol{\nu}',\boldsymbol{n}')$ and $\boldsymbol{d}(\xi',\boldsymbol{\nu}',\boldsymbol{n}'|\xi_0,\boldsymbol{\nu}_0,\boldsymbol{n})$, respectively. We therefore immediately see that the structure of this substitution is four terms oscillating at with frequencies $E(\xi_0,\boldsymbol{\nu}_0,\boldsymbol{n}|\xi_0,\boldsymbol{\nu}_0,\boldsymbol{n}')/\hbar, E(\xi_0,\boldsymbol{\nu}_0,\boldsymbol{n}|\xi_0,\boldsymbol{\nu}_0,\boldsymbol{n}')/\hbar \pm 2\omega_0$. Again, keeping only

the slowly rotating terms we have

$$V_{\mathrm{pol}}(\xi_0,\boldsymbol{\nu}_0,\boldsymbol{n}|\xi_0,\boldsymbol{\nu}_0,\boldsymbol{n}';t) = \\ -\frac{(F_0h(t))^2}{4}\sum_{\xi''\boldsymbol{\nu}''\boldsymbol{n}''}\left(\frac{\boldsymbol{e}\cdot\boldsymbol{d}(\xi_0,\boldsymbol{\nu}_0,\boldsymbol{n}|\xi'',\boldsymbol{\nu}'',\boldsymbol{n}'')\boldsymbol{d}(\xi'',\boldsymbol{\nu}'',\boldsymbol{n}''|\xi_0,\boldsymbol{\nu}_0,\boldsymbol{n}')\cdot\boldsymbol{e}}{E(\xi'',\boldsymbol{\nu}'',\boldsymbol{n}''|\xi_0,\boldsymbol{\nu}_0,\boldsymbol{n}')+\hbar\omega_0}\right. \\ \left.+\frac{\boldsymbol{e}\cdot\boldsymbol{d}(\xi_0,\boldsymbol{\nu}_0,\boldsymbol{n}|\xi'',\boldsymbol{\nu}'',\boldsymbol{n}'')\boldsymbol{d}(\xi'',\boldsymbol{\nu}'',\boldsymbol{n}''|\xi_0,\boldsymbol{\nu}_0,\boldsymbol{n}')\cdot\boldsymbol{e}}{E(\xi'',\boldsymbol{\nu}'',\boldsymbol{n}''|\xi_0,\boldsymbol{\nu}_0,\boldsymbol{n}')-\hbar\omega_0}\right). \tag{8.14}$$

Assuming that the rovibrational coupling is not exhibited on the time scale of relevance and using the fact that rotational level spacing is much smaller than the vibronic, we may neglect the dependence on the rotational states and write

$$\begin{aligned} V_{\mathrm{pol}} &= -\frac{(F_0h(t))^2}{4}\sum_{\xi''\boldsymbol{\nu}''}\frac{2E(\xi'',\boldsymbol{\nu}''|\xi_0,\boldsymbol{\nu}_0)}{E(\xi'',\boldsymbol{\nu}''|\xi_0,\boldsymbol{\nu}_0)^2-(\hbar\omega_0)^2} \\ &\quad\times\boldsymbol{e}\cdot\boldsymbol{d}(\xi_0,\boldsymbol{\nu}_0|\xi'',\boldsymbol{\nu}'')\boldsymbol{d}(\xi'',\boldsymbol{\nu}''|\xi_0,\boldsymbol{\nu}_0)\cdot\boldsymbol{e} \\ &= -\frac{(F_0h(t))^2}{4}\sum_{i,i'}e_i\alpha_{i,i'}e_{i'}. \end{aligned} \tag{8.15}$$

Here, $\alpha_{i,i'}$ is the *dynamic polarizability* tensor

$$\alpha_{i,i'} = 2\sum_{\xi''\boldsymbol{\nu}''}\frac{E(\xi'',\boldsymbol{\nu}''|\xi_0,\boldsymbol{\nu}_0)}{E(\xi'',\boldsymbol{\nu}''|\xi_0,\boldsymbol{\nu}_0)^2-(\hbar\omega_0)^2}d_i(\xi_0,\boldsymbol{\nu}_0|\xi'',\boldsymbol{\nu}'')d_{i'}(\xi'',\boldsymbol{\nu}''|\xi_0,\boldsymbol{\nu}_0). \tag{8.16}$$

When the laser pulse is of relatively low frequency, e.g., in the near infrared, it may be an accurate description to neglect the dependence on the angular frequency and simply use the static polarizabilities. These are often available in literature.

The interaction given by Eq. (8.15) describes the effective coupling between the rotational states of the initial vibronic level. It induces a wave packet of rotational states in the manifold of the initial vibronic state. Now, the eigenstates of rotation are the angular momentum eigenstates and the variable(s) conjugate to angular momentum is the angle. Thus, the product of the spread in the angular momentum and the spread in angle fulfills a Heisenberg uncertainty relation [43], i.e., the spread of angular momentum and the angle are roughly inversely proportional. From this we may intuitively understand how the laser induced alignment brings an initial rotational state into a superposition of many rotational states (the wave packet) and through this allows for a very localized angular distribution.

8.3 Summary

In summary, this chapter described the concepts of alignment and orientation. We considered the non-resonant coupling of a laser to a molecule and derived

an effective Hamiltonian. This Hamiltonian leads to alignment, by inducing a rotational wave packet in a given vibronic state.

Chapter 9

ATI and HHG from aligned and oriented molecules

So far in this report we have studied ionization and high-order harmonic generation (HHG) from molecules that we assumed to be perfectly aligned along one or more axes in space. Experiments are faced with the issue of randomly oriented molecules which leads to blurred observations of processes. Thus, the features mentioned in Chapters 6 and 7 are partly or completely washed out.

The ability to align gas phase molecules by short non-ionizing laser pulses can be used to achieve more detailed insight into strong-field processes. In the typical experiment, a number of alignment (and possibly orienting) pump pulses are used to prepare the molecules. As explained in the previous chapter, this does not lead to a change of the electronic state, but merely a superposition of rotational states in the initial vibronic manifold which leads to an angularly confined gas of molecules. Then at some delay t_d a short (on the rotational time scale) strong laser pulse probes the system via, for instance, ionization or HHG (see Fig. 9.1).

In this chapter, we will discuss how to implement the theory developed in Chapter 8 to linear molecules and look at a few case studies of the pump-probe type of experiments mentioned above.

9.1 Calculating the alignment dynamics of linear molecules

The treatment of the alignment dynamics amounts to solving the rotational part of the time-dependent Schrödinger equation for the initial vibronic state. We currently limit ourselves to linear molecules in the Σ electronic state. In this case the field-free rotational eigenfunctions are simply spherical harmonics, $Y_J^M(\theta, \phi)$ and for a linearly polarized alignment pulse (defining the LF Z

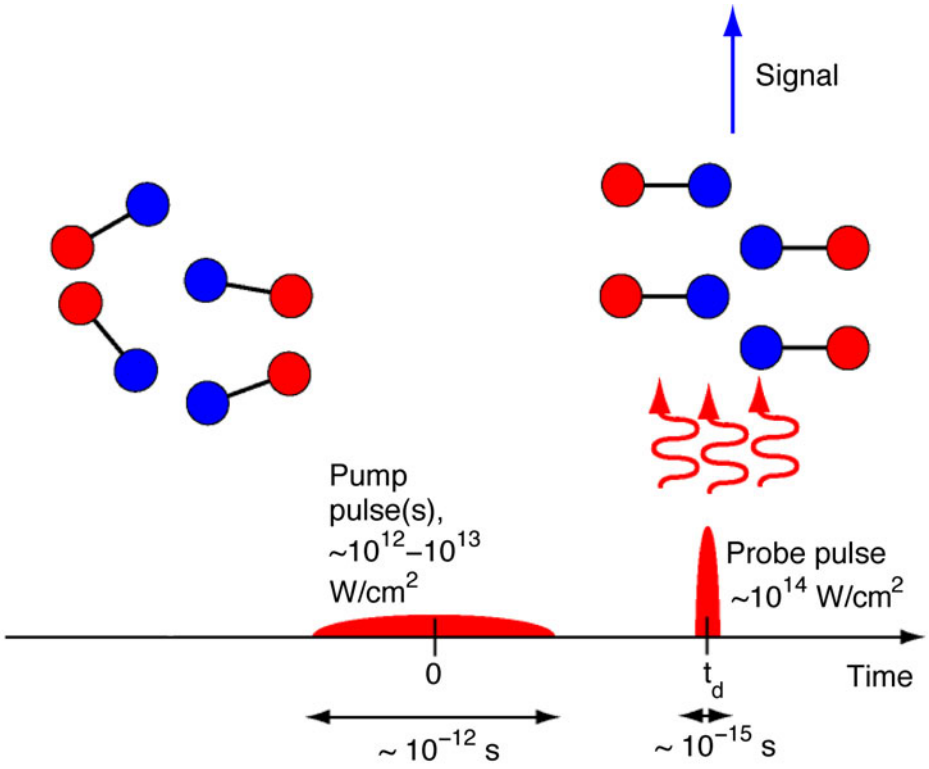

Figure 9.1: Illustration of a typical pump-probe experiment, where the molecular gas is pumped, or in other words prepared, by alignment and consequently probed by a short intense laser that causes for instance ionization or HHG.

axis) we may write Eq. (8.13) as[1]

$$i\frac{d}{dt}c_{J,M}(t) = -\frac{(F_0 h(t))^2}{4}\sum_{J'}\langle Y_J^M|\left[\alpha_\parallel\cos^2\theta + \alpha_\perp\sin^2\theta\right]|Y_{J'}^M\rangle e^{i(E_J-E_{J'})t} \times c_{J',M}(t), \tag{9.1}$$

where $\alpha_\parallel$ and $\alpha_\perp$ are the polarizability components parallel and perpendicular to the internuclear axis. The energy of the field-free eigenstate Y_J^M is $E_J = BJ(J+1) = (1/2)I^{-1}J(J+1)$, where B is the rotational constant and I is the principal moment of inertia. Note that the time evolution during any alignment pulse is sensitive only to the temporal changes in the pulse envelope, $h(t)$, and not the rapid oscillations with frequency ω_0 of the field. We will always assume that the envelope of the alignment pulse is a Gaussian envelope

$$h(t) = \exp\{-\ln(2)[t/(\tau_{\mathrm{FWHM}}/2)]^2/2\} \tag{9.2}$$

[1]There is no mixing of states belonging to different M's.

corresponding to a *full width at half maximum* (FWHM) pulse duration of τ_{FWHM}.

In the case of a series of pump pulses composed of a number of orienting electric fields $F^{(m)}_{\mathrm{orient}}(t)$ and alignment pulses with envelopes $F^{(n)}_{\mathrm{align},0}(t)$, all of the same linear polarization direction, defining the LF Z axis we have

$$\begin{aligned} i\frac{d}{dt}c_{J,M}(t) = &-\mu\sum_m F^{(m)}_{\mathrm{orient}}(t)\sum_{J'}\langle Y^M_J|\cos\theta|Y^M_{J'}\rangle e^{i(E_J-E_{J'})t}c_{J',M}(t) \\ &-\frac{1}{4}\sum_n F^{(n)^2}_{\mathrm{align},0}(t)\sum_{J'}\langle Y^M_J|\left[\alpha_\parallel\cos^2\theta+\alpha_\perp\sin^2\theta\right]|Y^M_{J'}\rangle e^{i(E_J-E_{J'})t} \\ &\times c_{J',M}(t) \end{aligned} \tag{9.3}$$

with μ the permanent dipole moment of the molecule. The matrix elements of the field-free states are known analytically and the differential equations may be solved numerically. As soon as the pump pulses are over, no population is transferred between different rotational states and the propagation can be carried out analytically. The phase difference accumulated between two neighboring J states due to the field-free evolution is $(E_{J+1}-E_J)\Delta t = I^{-1}J\Delta t$. Thus, we see that at time delays $\Delta t = T_{\mathrm{rev}} = 2\pi I$ the phase difference between all neighboring states in the wave packet is exactly an integer multiple of 2π. The wave function is thus only changed by an unimportant overall phase. This implies that alignment dynamics (as modeled here) are perfectly periodic after the alignment pulse(s). At the so-called half revival time, $t = T_{\mathrm{rev}}/2$, the relative sign between the components of the wave packet alternates.

The rotational states in the initial vibronic manifold of a molecule are closely spaced. It is therefore important to carry out thermally average calculations, i.e., average results from a range of initial rotational states each weighted by a Boltzmann factor $\propto \exp(-E_J/k_BT_{\mathrm{rot}})$ (see also Chapter 4) and, when relevant, a spin statistic weight.

9.2 Ionization from aligned CS_2

In this section, we will review an experiment on ionization from aligned CS_2 [4] to demonstrate how alignment provides a more detailed knowledge of the physics of ionization. This new detail challenges the predictions of the strong field approximation (SFA) and prompts the need for a deeper theoretical understanding.

9.2.1 The experimental setup

The experiment was conducted by Femtolab at Aarhus University and they used a pump-probe scheme (see Fig. 9.1) with two 800 nm lasers to investigate how ionization of the linear molecule CS_2 depends on the angle α between the internuclear axis and the polarization vector of the linearly polarized ionization pulse. Specifically, in the experiment CS_2 molecules were first aligned

along a given direction using a 0.5 ps (FWHM), $I = 2.9 \times 10^{12}$ W/cm^2 linearly polarized pump pulse. Then at a delay with respect to this pulse, the molecules were exposed to the 25 fs (FWHM), I= 7.7×10^{13} W/cm^2 ionizing pulse. Experimentally, the best degree of field-free alignment was observed to occur $\sim$ 76 ps after the alignment pulse which corresponds to the peak of the first half revival time (see the discussion following Eq. (9.3)). A velocity map imaging spectrometer was used to detect the electrons.

9.2.2 Experimental observations

Figure 9.2 shows the experimental setup and some measured momentum distributions. Each momentum distribution consists of radial ringlike peaks. These are multi-photon peaks (see also Chapter 3) with the innermost pair of half rings corresponding to ionization by the minimum number of photons, 10, required to overcome the ionization threshold, $I_p = 10.08$ eV. The very sharp radial substructures observed in the two innermost pairs of half rings are due to Rydberg states brought into resonance by the ac Stark shift [87].

We are currently interested in the emission direction of the electron. In the four images displayed in Fig. 9.2 the bulk of the electron emission occurs along the polarization vector of the ionization pulse for all the multi-photon channels. Pronounced differences are displayed between the detailed electron emission patterns for different molecular orientations in Figs. 9.2(c)-(e). These differences are particularly clear for electrons in the outermost rings emitted perpendicular to the polarization of the ionizing pulse, i.e., along the Z-axis in Fig. 9.2. This is clearly seen by comparing, for instance, the $N = 12$-, 13- and 14-photon channels recorded in the parallel geometry (see Fig. 9.2(c)) and the perpendicular geometry (Fig. 9.2(e)).

To quantify the dependence of the electron emission on the relative orientation α, each individual multi-photon channel is integrated radially over the corresponding pair of half rings in the images to give the photo-electron angular distribution (PAD). The results, represented as the number of electrons recorded per laser pulse versus ϕ_{2d}, are displayed in Fig. 9.3, where ϕ_{2d} is the angle between the two dimensional projected electron ejection direction and the vertical ionizing pulse polarization. We show the resulting curves without an alignment pulse and at $\alpha = 0^\circ$, 45° and 90° for the (a) 11-, (b) 12-, (c) 13-, and (d) 14-photon channels. First, we note that the electron signal depends on the orientation α. The $\alpha = 45^\circ$ geometry provides the largest and the 90° geometry the smallest signals. This observation is consistent with recent measurements, based on detection of ion yields, on the orientational dependence of intense-laser single ionization of the CO_2 molecule [88], whose highest occupied molecular orbital (HOMO) has π_g symmetry as in CS_2. Second, the angular distributions change for the different orientations for electrons centered around 90° and 270° (i.e., along the Z-axis). For example, in the 12-photon channel (Fig. 2(b)) there is local maximum in the PAD at $\phi_{2d} = 90^\circ$ for $\alpha = 45^\circ$, whereas the PAD recorded for $\alpha = 0^\circ$ exhibits a global minimum at $\phi_{2d} = 90^\circ$. Similar differences between the angular distributions recorded at different orientations are observed for the 13-photon and 14-photon channels.

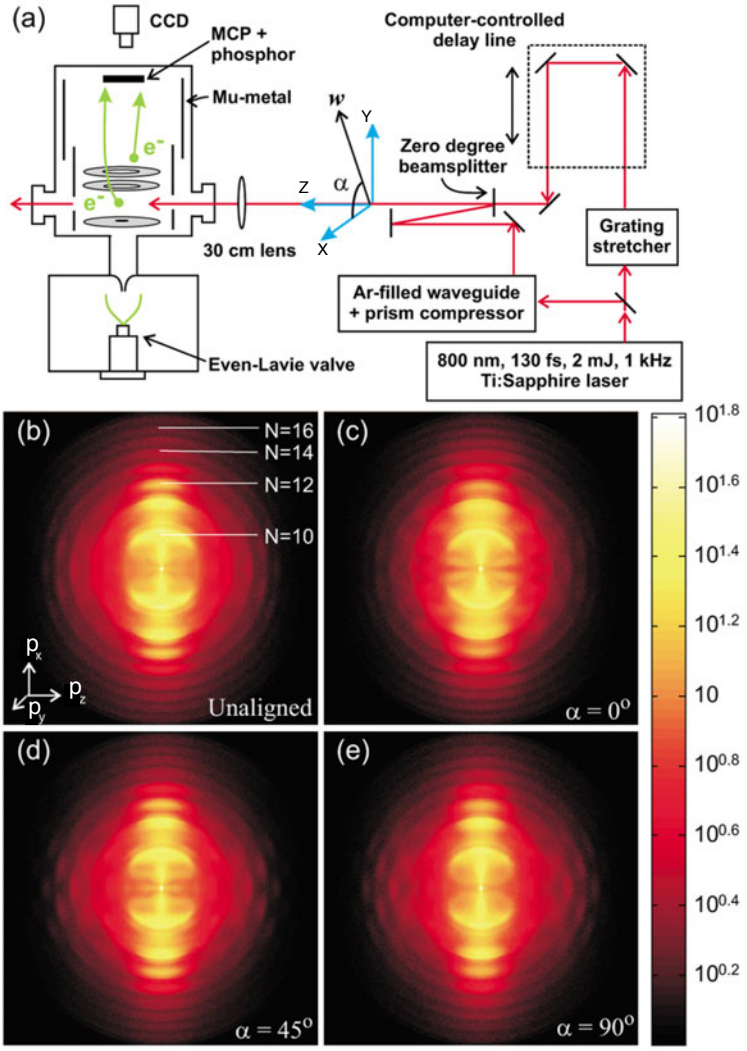

Figure 9.2: Experimental observation of ionization of aligned CS_2. Panel (a) shows the experimental setup, laser propagation (along Z) and polarization (along X) directions. The vector $\boldsymbol{w}$ represents the polarization of the alignment pulse, and hence the direction of alignment of the molecules. Panels (b)-(e) display two dimensional electron images as a function of the vertical momentum p_X and the horizontal momentum p_Z from multi-photon ionization of (b) unaligned molecules, and from aligned molecules with an angle (c) $\alpha = 0°$, (d) $\alpha = 45°$, (e) $\alpha = 90°$ between the polarizations of the alignment ($\boldsymbol{w}$) and ionizing ($\boldsymbol{\epsilon}$) pulse. The ring structure corresponds to different above-threshold ionization channels. In (b), N denotes the number of photon absorptions associated with the rings.

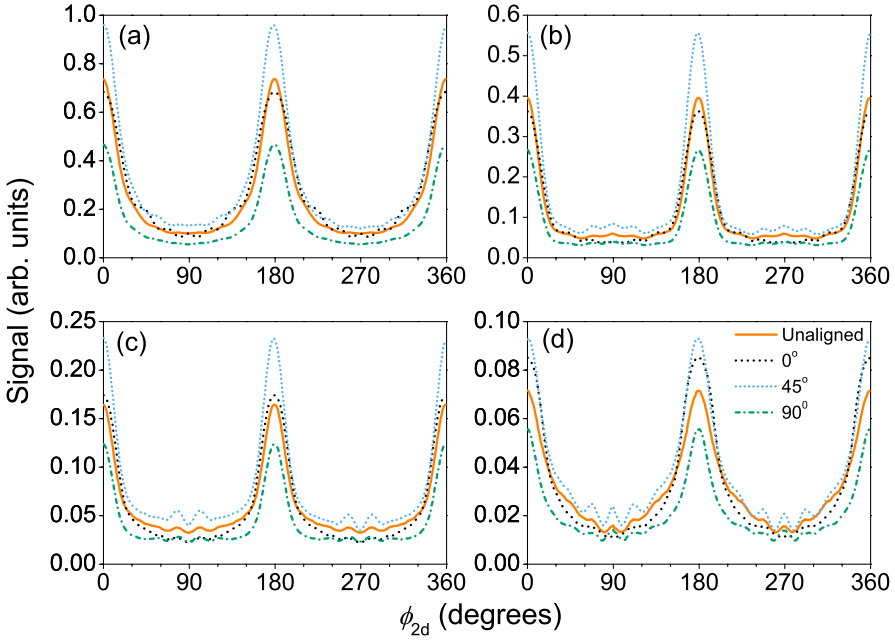

Figure 9.3: Experimental photo-electron angular distributions for the (a) 11-, (b) 12-, (c) 13- and (d) 14-photon ionization channels extracted from Figs. 1(b)-(e) by radial integration. The legends in (d) apply to all panels.

9.2.3 Modeling the experiment using the strong-field approximation

To understand the experimental observations, we will now calculate the PADs within the SFA. First, we find the orientational distribution of the molecules as a function of time using the procedure prescribed in the beginning of this chapter. In this procedure, we use a parallel (perpendicular) polarizability volume of 15.6 Å^3 (5.3 Å^3) and a linearly polarized aligning pulse with peak intensity 2.9×10^{12} W/cm^2 and duration of 0.5 ps (FWHM). The initial rotational temperature is taken to be 2 K. In agreement with the experimental observations, the calculated alignment distribution peaks after 75.8 ps, and we will use the orientational distribution at this instant to calculate the ionization signal according to Eq. (4.10) from Chapter 4 . For a given orientation, Ω, we calculate the momentum distribution of the electron

$$\frac{dP}{dp_X dp_Z}(p_X, p_Z; \Omega) = \int_{-\infty}^{\infty} dp_Y \, |T_{f,\boldsymbol{\nu},i}(\boldsymbol{p}, \Omega)|^2. \tag{9.4}$$

Here, $T_{f,\boldsymbol{\nu},i}$ is the transition amplitude from Eq. (5.34). The matrix element entering the transition amplitude may be evaluated analytically at each time

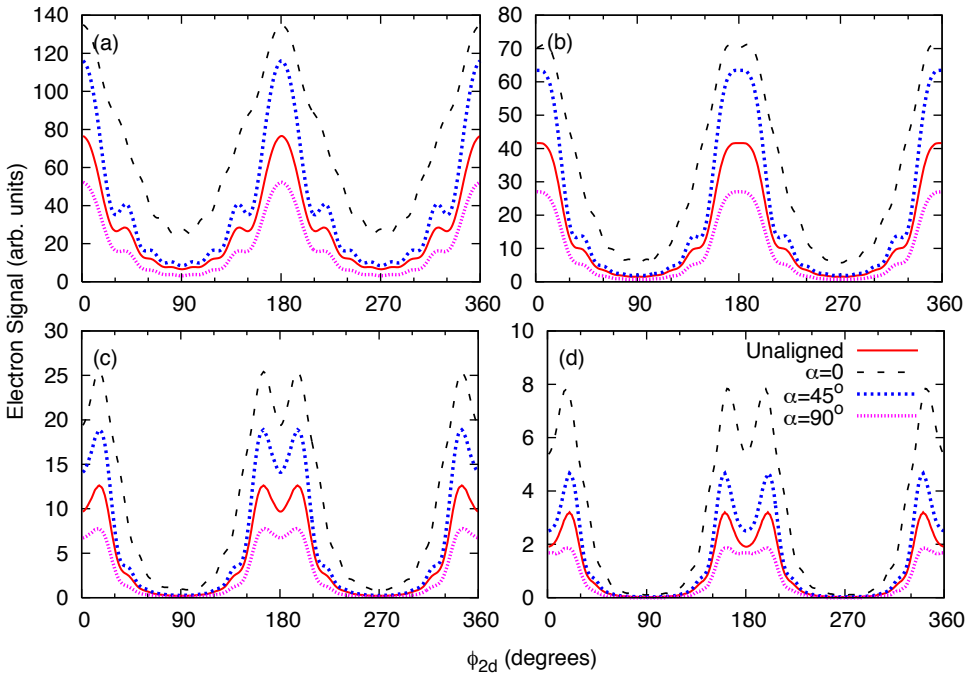

Figure 9.4: Photo-electron angular distributions calculated within the strong-field approximation. Panels (a)-(d) represent the signals obtained by integrating the $dP/dp_X dp_Z$ distribution over the circular areas identified as different ATI channels (see Fig. 9.2(b)). The different curves correspond to the unaligned, $\alpha = 0°$, $\alpha = 45°$, and $\alpha = 90°$ geometries as detailed by the legends in (d). For ease of comparison we have scaled the $\alpha = 90°$ alignment signals by a factor of 3.

step using the asymptotic form of the initial molecular wave function (see also the Kuchiev-Ostrovsky model in Chapter 5). As a function of time, the resulting integrand oscillates very rapidly, and we use the saddle-point method to calculate the time integral. This method basically reduces the integral to a sum of analytically known terms that are evaluated at the saddle points, t_{SP}, given by $(\boldsymbol{p} + \boldsymbol{A}(t_{\mathrm{SP}}))^2 + I_P = 0$. Here $\boldsymbol{A}(t)$ is the vector potential, and we use a sine squared envelope (Eq. (3.2)).

In addition to orientational averaging, we need to compensate for the fact that only a fraction of the large number of molecules used in the experiment actually experiences the real peak intensity (the intensity at the center of the beam). To do this we use a volume weighted average over all relevant intensities [89].

Finally, we integrate radially over each multi-photon peak in order to obtain the PAD for each multi-photon channel.

Our results are shown in Fig. 9.4. We have chosen to concentrate on an-

gular distributions corresponding to the 11-, 12-, 13- and 14-photon absorption channels of Figs. 9.3(a)-(d). The results in the figure show a qualitative agreement with the experiment. The calculations exhibit minima at $\phi_{2d} = 90°$ (270°) and maxima around $\phi_{2d} = 0°$ (180°). The detailed modulations, however, differ somewhat in size and shape from the experimental observations. When we look at the results on a quantitative level, there are significant differences. In the experimental data there is typically a factor of 8 between the minimum and the maximum in each PAD, whereas in the theoretical result this factor is $\sim 5.9 - 8.1$ in the 11-, $\sim 11.5 - 38.0$ in the 12-, $\sim 20.0 - 77.0$ in the 13- and $\sim 46.0 - 85.0$ in the 14-photon absorption channel. Hence the theoretical model generally overestimates the ϕ_{2d} dependence. Turning to the magnitudes of the signals in Fig. 9.4, theory predicts in decreasing order $\alpha = 0°$, 45°, unaligned and 90°. In the experimental data, the order is 45°, unaligned, 0°, and 90° for the 11- and 12- photon absorption channels while it is 45°, 0°, unaligned, and 90° in the 13- and 14-photon absorption channels.

9.2.4 Shortcomings of the strong-field approximation

We have investigated several possible reasons for the discrepancy between the measurements and the predictions of the SFA. First, we found that there is no effect of ionization from the second highest occupied orbital, primarily because its binding energy of 14.60 eV leads to a strongly reduced ionization probability compared to that of the HOMO. Second, we found that there is no significant change in the ionization probability or in the overall form of the PAD's if the S-C-S angle is reduced from 180° to 140°. This rules out the influence from possible bending (due to electronic or vibrational excitation) during the ionization pulse.

We believe that the disagreement between theory and experiment is associated with the excited state spectrum of the CS_2 molecule. Recent work seems to confirm this [90]. Additionally, deviation may arise from the final state Coulomb interaction. Neither of the two effects are accounted for in the SFA.

Our studies clearly show that the ability to align a molecular ensemble prior to the interaction with a strong femtosecond field leads to observations at an accuracy that challenges our current level of understanding and theory for ionizations from molecules.

9.3 HHG from the oriented CO molecules

In the previous section, we saw how alignment may be used to gain information from CS_2 with a resolution that could not have been achieved from an unaligned gas. As mentioned in Chapter 8, alignment only refers to an order with respect to an axis, but where the inversion symmetry is preserved. This does not make a difference for CS_2, since the molecule is already inversion symmetric. However, for heteronuclear molecules or other molecules that are not inversion symmetric, an aligned gas sample will suffer from an averag-

ing effect over the two opposite molecular orientations (cf. Fig. 8.1). Recent experimental efforts have shown that orientation of polar molecules may be accomplished using the combination of a laser field and a dc field [91–93] or by a two color laser field [94]. Measurements on molecules without inversion symmetry that are oriented, not merely aligned, will immediately lead to new observations.

High-order harmonic generation is one example where breaking of inversion symmetry strongly affects the experimental outcome. As briefly discussed in Chapter 6, the presence of inversion symmetry implies that only odd harmonics appear in the harmonic spectrum. If this inversion symmetry is broken even harmonics may occur.

Here, we investigate an experimental setup with CO molecules that would lead to the observation of even harmonics. The CO molecule has a rotational constant $B = 57.9$ GHz, dipole moment $\mu = 0.112$ Debye, and a parallel (perpendicular) polarizability volume of 1.925 Å^3 (1.420 Å^3). Orientation is accomplished using two electric fields of the same linear polarization direction, which specifies the LF Z axis. The electric field, breaking the inversion symmetry, is that of a half cycle pulse (HCP) [95]

$$F_{\text{orient}}(t) = \begin{cases} F_0 \cos^2(\pi t/\tau) & \text{for } -\frac{\tau}{2} \le t \le \frac{\tau}{2} \\ 0 & \text{otherwise} \end{cases} \tag{9.5}$$

with amplitude $F_0 = 870$ kV/cm and pulse duration $\tau = 0.5$ ps. It is followed 4.14 ps later by an alignment pulse with FWHM of 0.5 ps and intensity 5×10^{12} W/cm^2. The purpose of the HCP is to orient the molecule. We apply the alignment pulse shortly after to decelerate the rotation of molecular dipoles having small angles with respect to the orientation direction and accelerate dipoles having large angles. This corrects the rotational velocity aberration and improves the overall orientation at a later time [96]. Using an initial rotational temperature of 5 K, we obtain the time-dependent orientational distribution shown in Fig. 9.5(a). We observe a clear asymmetry about 90° at time $t_d = 8.1$ ps after the peak of the HCP. At this instant we should be able to drive even harmonics, as confirmed in panel (b) showing the emitted high-order harmonics generated by an 800 nm, 2×10^{14} W/cm^2 laser field of the same polarization direction as the pump pulses.

As a concluding remark, we mention that orientation of molecules is not needed to break the inversion symmetry and generate even harmonics. One may establish the needed asymmetry of the laser electric field by using a two-color ($\omega_0 - 2\omega_0$) driving field, where a second harmonic field is added to the fundamental driving pulse.

9.4 Summary

In the chapter above, we briefly described how numerically to solve the alignment dynamics given by the equations derived in Chapter 8. We then looked at alignment as a pump to prepare the system in a well defined initial state

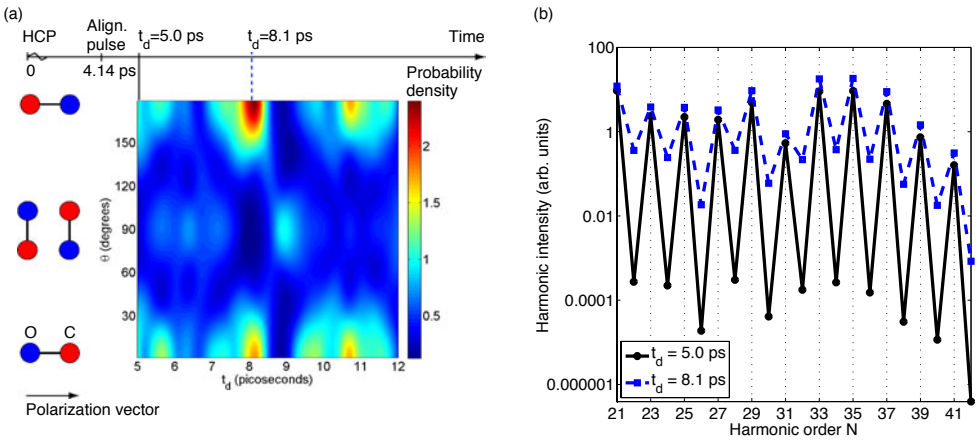

Figure 9.5: The figure illustrates a pump probe experiment that leads to even harmonics from the CO molecule. (a) The orientational distribution after orientation by a half cycle pulse (HCP) and an alignment pulse. Here θ is the angle from the polarization axis and there is azimuthal symmetry. (b) High-order harmonic yield from CO at delay t_d with respect to the HCP using an 800 nm driving pulse of intensity 2×10^{14} W/cm^2. Even harmonics are observed for $t_d = 8.1$ ps, and we also show the generated harmonics for $t_d = 5$ ps as a reference.

and thus avoid the loss of information that follows from averaging over orientations of an unaligned gas of molecules. Following alignment, a short pulse is fired to probe the system via ionization or high-order harmonic generation. Ionization from aligned CS_2 led to measurements with a precision that challenged the predictions of the strong-field approximation. Finally, we saw how the alignment combined with orientation opens for the generation of even high-order harmonics.

Chapter 10

Laser controlled torsion of molecules

The previous two chapters have demonstrated how strong non-resonant laser pulses may be used to control the orientation of molecules. Molecular manipulation by lasers extends beyond the control of external degrees of freedom and has been demonstrated for internal degrees of freedom. For small linear molecules the electric field from laser pulses has been used to control vibrational motion [97] and to modify energy potential barriers such that photoinduced bond breakage is guided to yield a desired final product [98, 99].

In the case of larger molecules, control of the lowest frequency vibrational modes attracts special interest since some of these modes correspond to motion along well-defined reaction coordinates separating two stable configurations of the molecule, *conformers*. In other words, a structural change of a molecule can be reached via the lowest frequency normal mode vibration. Although many molecules contain large number of conformers, it is often just two that dominate important chemical properties. An example is found in axially chiral molecules [100, 101] such as biaryl systems. Here, the two conformations are mirror images and they are known as *enantiomers*. Further, rotation about a single stereogenic carbon-carbon (C-C) bond axis changes the molecule from one enantiomer into the opposite enantiomer (see Fig. 10.1).

In this chapter, we will see that the laser-induced non-resonant polarizability interaction derived in Chapter 8 can be used to induce internal rotation of an axially chiral molecule around the stereogenic C-C bond axis [5]. This is to our knowledge the first demonstration that strong-field laser physics methods and time-resolved measurements are not limited to small linear molecules, but can actually be useful for describing exciting fundamental molecular phenomena; here chirality and enantiomeric transformation.

10.1 The principle of laser controlled torsion of molecules

In this section we outline the method used to obtain laser controlled torsion. The system used is 3,5-difluoro-3',5'-dibromo-biphenyl (DFDBrBPh), which is basically biphenyl (see Chapter 7), but where a pair of hydrogens have been substituted by fluorines and a pair of hydrogens with bromines through a chemical synthesis explained in Ref. [6]. The molecule is shown in Fig. 10.1. The fluorine and bromine substitutes serve a three-fold purpose. First, they are needed experimentally to detect the alignment distribution of the phenyl rings (see experimental details below). Second, the use of different atoms on each ring lets us discriminate the two rings. Finally, the much heavier bromines leads to a larger moment of inertia of the phenyl ring where these atoms are placed. Consequently, most of the laser induced rotation is carried by the lighter phenyl ring which eases interpretation of the experiment.

A model of the DFDBrBPh molecule with the stereogenic axis marked by red is shown in the inset of Fig. 10.1. In the absence of laser fields, torsional motion is governed by the field-free torsional potential. This potential has previously been calculated with quantum chemistry codes [102]. If we define the dihedral angle as the angle between the two phenyl rings, the field-free torsional potential has minima at dihedral angles of $\phi_d = \pm 39^\circ$ corresponding to the conformations of interest called the R_a and S_a enantiomers. The twisted equilibrium shape is characteristic of biphenyl compounds. Essentially, conjugation of the π-orbital systems of the phenyl rings favor a parallel geometry, but this trend is opposed by the steric repulsion between the ortho-positioned atoms [103] (the atoms closest to the stereogenic C-C axis). The field-free torsional potential is illustrated by the red dotted curve in Fig. 10.1. In the experiment the DFDBrBPh molecules are exposed to a moderate linearly polarized pulse with a duration of several nanoseconds (1 ns = 10^{-9} s). This is long compared to the time scale of the molecular rotation and causes each molecule to align with the stereogenic axis parallel to the polarization direction of the pulse [12, 104]. We then control ϕ_d using a femtosecond kick pulse to transiently modify the field-free potential curve (Fig. 10.1).[1] This pulse is linearly polarized perpendicularly to the previous pulse and its duration is of the order femtosecond. We refer to the femtosecond pulse as the *kick pulse*. The combined pulses will cause a three-dimensional alignment of the molecule a few picoseconds after the peak of the kick pulse, where all three axes of the molecule align along given axes fixed in space (defined by the two orthogonal polarization axes). More importantly, the kick pulse converts the initial stationary quantum states, localized near the minima of the torsional potential, into vibrational wave packets. Time-dependent torsional motion develops as a result of the temporal evolution of these wave packets. The grey and the black curves in Fig. 10.1 show the calculated expectation values of ϕ_d when the kick pulse has an intensity of 1.2×10^{13} W/cm^2 and a duration of 1.0 ps

[1] This interpretation is dependent on the fact that the polarizability interaction was derived in the length gauge (cf. Chapter 8).

(FWHM).

10.2 The experimental setup

The experiment was conducted by Femtolab. They used three focused, pulsed laser beams crossed at 90° through a rotationally cold gas of DFDBrBPh. The first laser beam is the nanosecond aligning pulse that aligns the stereogenic axis of the DFDBrBPh molecules. The duration and intensities used were 9 ns and $\sim 7 \times 10^{11}$ W/cm^2. The second laser beam is the kick pulse with a duration of 700 fs and a peak intensity of $\sim 5 \times 10^{12}$ W/cm^2. The third laser beam has not been mentioned above. It is a 25 fs, $\sim 2 \times 10^{14}$ W/cm^2 probe pulse which Coulomb explodes the molecules thereby producing ions. The ions were extracted by a weak static electric field, in a velocity imaging geometry, and projected onto a two-dimensional detector. The F^+ and Br^+ ions were detected separately by time gating.

10.2.1 Experimental observations

Figure 10.2(a) displays the ion images of F^+ and Br^+ at selected probe times. First, we must confirm that the nanosecond pulse is able to hold the C-C bond axis of DFDBrBPh along its polarization direction. By looking at Fig. 10.2(a) at $t_p = -0.87$ ps, we see the F^+ image is almost circularly symmetric. The small deviation from circular symmetry can be explained by noting that the kick pulse has a finite value at -0.87 ps. If the C-C bond axis is aligned perpendicular to the detector plane and the F-phenyl planes are uniformly distributed around the C-C bond axis, the innermost regions would contain no ions, which is exactly what we observe. The corresponding Br^+ image is also essentially circularly symmetric, although the empty portion in the center is less pronounced than for F^+. The fact that the heavier mass of Br gives it smaller momentum in the Coulomb explosion process may contribute to this.

Next, we look at how the kick pulse affects the system. At $t_p = 0.47$ ps, the circular symmetry is broken and both F^+ and Br^+ ions start to localize around the polarization direction of the kick pulse. The F^+ ions remain within the radial range of the ring structure. This shows that the kick pulse does not cause any significant distortion of the C-C bond axis alignment, but rather, initiates an overall rotation of the molecule around this axis. This overall rotation of the molecule around this axis is expected since the torque imparted by the kick pulse will force the second most polarizable axis (SMPA) (see Fig. 10.3) to align along the kick pulse polarization after a delay determined by the kick strength. At $t_p = 1.47$ ps the localization sharpens for both ions species. At this time Br^+ ions are simply more localized around the polarization axis while a four dot structure appears in the F^+ ion distribution. This behavior is consistent with alignment of the SMPA along the kick pulse polarization. In the limit of perfect SMPA alignment, the Br^+ ions would appear as two pairs of strongly localized regions on the detector corresponding to molecules with their Br-phenyl plane positioned either 11° clockwise or

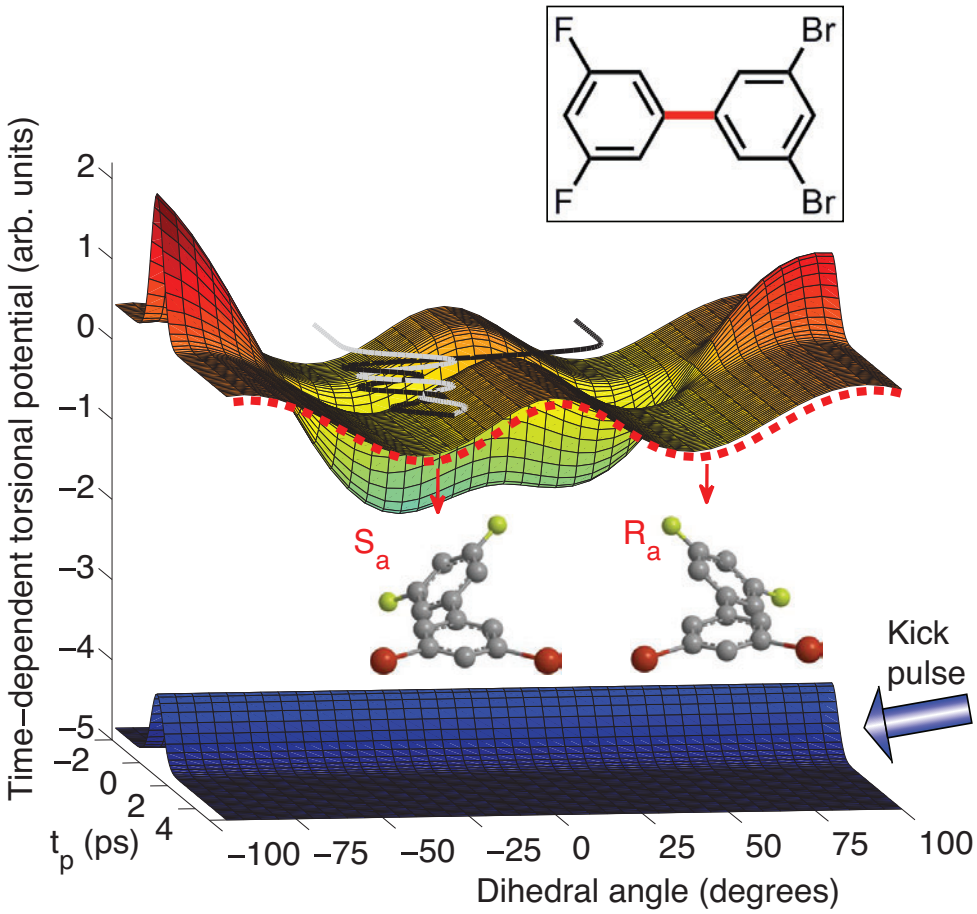

Figure 10.1: To illustrate the principle of laser-induced torsion we show the calculated kick pulse induced time-dependent torsional potential as a function of time. The asymmetry in the potential is obtained by orienting the molecules (here with the Br-phenyl plane out of the paper), three dimensionally aligning them, and by polarizing the kick pulse at an angle of 13° with respect to the second most polarizable axis (SMPA) (see Fig. 10.3). For the S_a enantiomer, starting out with $\langle\phi_d\rangle_i = -39°$, the time varying potential induces an oscillatory motion (grey curve) corresponding to torsion confined within the initial well. By contrast, due to the induced asymmetry between the two wells, the initial R_a enantiomer is traversing the central torsional barrier, and ends up as an S_a enantiomer (black curve). The inset shows a model of the DFDBrBPh molecule with the stereogenic axis marked by red (grey). We have omitted the hydrogen atoms on the molecular models for the sake of clarity (cf. Fig. 6.10).

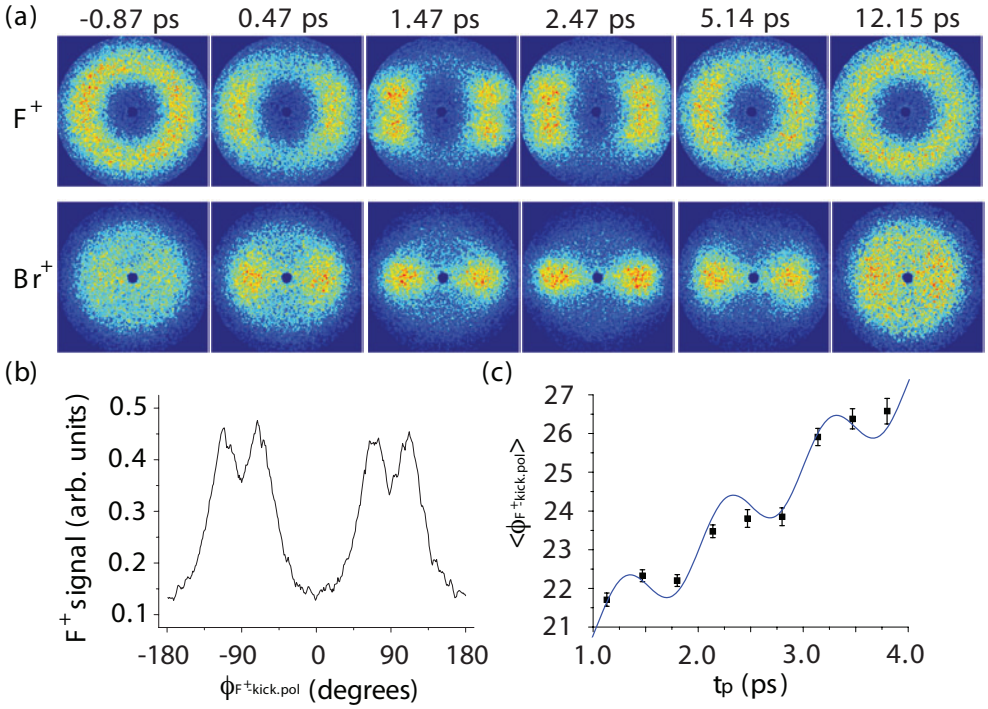

Figure 10.2: (a) Ion images of F^+ and Br^+ fragments at different probe times t_p. The nanosecond pulse is polarized perpendicularly to the image plane and the 5×10^{12} W/cm^2, 0.7 ps (FWHM) kick pulse is polarized horizontally. (b) Angular distribution of the F^+ ions, at t_p =1.47 ps, obtained by radially integrating the corresponding F^+ ion image. The splitting of the pairwise peaks is twice the average angle, $\langle \phi_{F^+\text{- kick. pol}} \rangle$, between the F^+ ion recoil (and thus the F-phenyl plane) and the kick pulse polarization. (c) $\langle \phi_{F^+\text{- kick. pol}} \rangle$ as a function of t_p, for times where a clear four-peak structure is visible in the angular distributions. The curve is a fit of the sum of a linear and a harmonic function to the experimental points (squares).

counterclockwise to the SMPA. Each pair of Br^+ ions would then be angularly separated by 22°. In practice the SMPA alignment is not strong enough to resolve the two Br^+ regions. It is, however, sharp enough to resolve the two pairs of F^+ ion hits due to the much larger offset of the F-phenyl plane from the SMPA. At $t_p = 2.47$ ps the Br^+ distribution has localized further showing that the Br-phenyl plane has rotated into stronger alignment with the kick pulse polarization. If the torsion was unaffected, i.e., ϕ_d remained unchanged, the F^+ ion image at $t_p = 2.47$ ps should exhibit a distinct four-dot structure similar to the image at $t_p = 1.47$ ps but with a larger angular splitting between the ion regions in each of the two pairs. Clearly, the four-dot structure at 2.47 ps is significantly blurred compared to the case at 1.47 ps. We conclude that the kick pulse not only sets the molecule into controlled rotation around the C-C axis, but it also initiates torsional motion.

Beyond 3.8 ps, the continued rotation around the C-C axis and the time dependent dihedral angle remove the angular confinement of both the F^+ and Br^+ ions. The images for both ion species eventually regain their circularly symmetric form (see images at 12.15 ps in Fig. 10.2(a)) identical to the pre-kick pulse images at -0.87 ps.

By analyzing the angular distribution of the F^+ ions as a function of t_p, we can gain deeper understanding into the effect of the kick pulse. Fig. 10.2(b) shows an example of the F^+ angular distribution at $t_p = 1.47$ ps. Figure 10.2(c) displays the average angle between the F-phenyl rings and the kick pulse polarization as a function of t_p in the time interval where a clear four-peak structure is visible in the angular distributions. The increase from 22.5° at 1.47 ps to 26.5° at 3.8 ps shows that the F-phenyl plane gradually moves away from the kick pulse polarization. This is due to the overall rotation of the molecule around the C-C bond axis, and we ascribe the recurrent dips to a periodical variation in ϕ_d. We estimate the period of this oscillation to be ~ 1 ps and the amplitude to $\sim 0.6°$.

10.3 A semi-classical theory on laser controlled torsion

10.3.1 Modeling the molecule

We use of two sets of coordinate systems, a molecular fixed (MF) frame attached to the molecule and a laboratory fixed (LF) frame specified by the lasers, to account for the observed motion of the nuclei of the DFDBrBPh molecule (see Fig. 10.3). The MF coordinates are chosen with the z axis along the stereogenic axis pointing from the phenyl ring with the bromines towards the phenyl ring with the fluorines, and the x axis is chosen along the phenyl ring with the bromines. The LF coordinates are chosen with the Z axis along the polarization direction of the nanosecond pulse and the X axis along the kick pulse polarization direction. We assume that the stereogenic axis of the DFDBrBPh molecule is aligned along the Z axis, in agreement with experimental observations. Additionally, we look at only the lowest normal

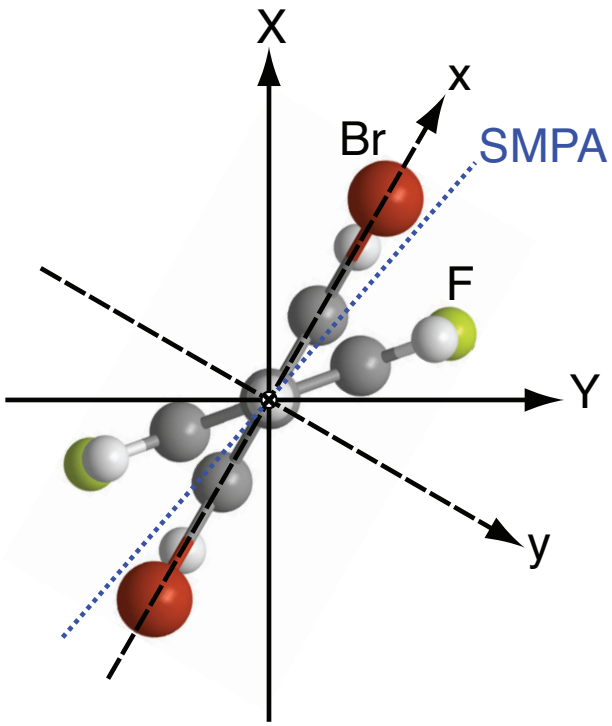

Figure 10.3: Model of DFDBrBPh along with the molecular fixed (MF) xyz and the laboratory fixed (LF) XYZ coordinate axes. The $z = Z$ axis points into the plane of the paper. The dotted line indicates the second most polarizable axis (SMPA), which is located 11° from the Br-phenyl ring and 28° from the F-phenyl ring.

mode, which corresponds to torsion.[2]

In this simplified situation the task is to describe the coupled rotations of the two (rigid) phenyl rings of the molecule as given in the LF frame by the field-free Hamiltonian

$$H_0 = -\frac{1}{2I_{\mathrm{Br}}}\frac{\partial^2}{\partial\phi_{\mathrm{Br}}^2} - \frac{1}{2I_{\mathrm{F}}}\frac{\partial^2}{\partial\phi_{\mathrm{F}}^2} + V_{\mathrm{tor}}(\phi_{Br} - \phi_F), \tag{10.1}$$

where $\phi_i, i = \mathrm{Br}, \mathrm{F}$ is the angle of the i phenyl ring with respect to the kick pulse polarization axis, I_i is the moment of inertia for rotation of the i phenyl ring around the stereogenic axis ($I_{\mathrm{Br}} = 8911925$ a.u., $I_{\mathrm{F}} = 1864705$ a.u.) and $V_{\mathrm{tor}}(\phi_{\mathrm{Br}} - \phi_{\mathrm{F}})$ is the field-free torsional potential as obtained from quantum chemistry calculations (see Fig. 10.1).

[2]Neglecting all other normal modes has been justified via a normal mode analysis. The normal mode analysis showed that the lowest frequency vibration corresponds almost purely to the torsion of the phenyl rings. Additionally, the Raman cross-section with respect to torsion is by far larger than the Raman cross-section with respect to any other normal mode meaning that the laser coupling with torsion dominates.

By changing the coordinates to the dihedral angle $\phi_d = \phi_{\mathrm{Br}} - \phi_{\mathrm{F}}$ between the two phenyl rings and the weighted azimuthal angle $\Phi = (1-\eta)\phi_{\mathrm{Br}} + \eta\phi_{\mathrm{F}}$, characterizing the rotation of the molecule, with $\eta = I_{\mathrm{F}}/(I_{\mathrm{F}} + I_{\mathrm{Br}}) = 0.173$, we obtain

$$\begin{aligned} H_0 &= \left(-\frac{1}{2I}\frac{\partial^2}{\partial\Phi^2}\right) + \left(-\frac{1}{2I_{\mathrm{rel}}}\frac{\partial^2}{\partial\phi_d^2} + V_{\mathrm{tor}}(\phi_d)\right) \\ &= H_\Phi + H_{\phi_d}. \end{aligned} \tag{10.2}$$

Here $I = I_{\mathrm{Br}} + I_{\mathrm{F}}$ is the total moment of inertia of the molecule for rotation around the stereogenic axis and $I_{\mathrm{rel}} = I_{\mathrm{Br}}I_{\mathrm{F}}/I$ is a relative moment of inertia for the two phenyl rings around the axis. A full rotation of either phenyl ring leaves us with the same molecule implying 2π-periodic boundary conditions of the eigenfunctions of H_0 from Eq. (10.1), i.e., $\psi(\phi_{\mathrm{Br}} + 2\pi m, \phi_{\mathrm{F}} + 2\pi n) = \psi(\phi_{\mathrm{Br}}, \phi_{\mathrm{F}})$, with m and n integers. We shall assume that this property also applies to Φ and ϕ_d, so that we simply need to consider eigenfunctions $\tilde{\psi}(\Phi, \phi_d) = \xi(\Phi)\chi(\phi_d)$ of Eq. (10.2) that separates into rotation of the molecule as described by the 2π-periodic function $\xi(\Phi)$ and torsion accounted for by the 2π-periodic function $\chi(\phi_d)$.[3] The separation is physically motivated by considering the energy scales related to rotation and torsion. The energy scale of the prior is given by $\hbar^2/(2I) = 1.3$ μeV. For torsion, on the other hand, the relevant energy is determined by the torsional potential, and a harmonic approximation of the potential near the minimum at 39° yields a frequency corresponding to the energy 3.1 meV. Being that the period of motion is of the order Planck's constant divided by the energy, we therefore see that the molecule rotates (Φ change) on a nanosecond time scale, whereas the torsion (ϕ_d change) is of picosecond duration.

The small energy separation of the rotational levels compared to that of the torsional levels implies that many rotational states will be occupied in thermal equilibrium. Consequently, we expect the Φ dynamics to behave classically (cf. Fig. 10.5), and we only treat the torsional dynamics quantum mechanically. The torsion is described by the stationary Schrödinger equation

$$H_{\phi_d}\chi_\nu(\phi_d) = E_\nu\chi_\nu(\phi_d), \tag{10.3}$$

with $\nu = 1, 2, \ldots$ denoting the energy eigenstates. To solve this equation we expand the Hamiltonian onto an orthonormal basis of 2π-periodic functions, which we diagonalize. The eigenstates below the torsional barriers exhibit an almost exact fourfold degeneracy, and linear combinations of the approximately degenerate states will also be stable at the time scales of the experiment. In particular, we can produce such stable states that are localized in the wells of the torsional potential and thus corresponds to the observable enantiomers. We will denote these states by $|L^{(i)}_{\nu_{\min}}\rangle$, with $i = 1, 2, 3, 4$ and

[3] Rigorously, the bounds for Φ depend on ϕ_d [105]. At the time scales of interest, however, a molecule generally only makes a small fraction of a full rotation so that the effect of Φ-ϕ_d coupling is negligible.

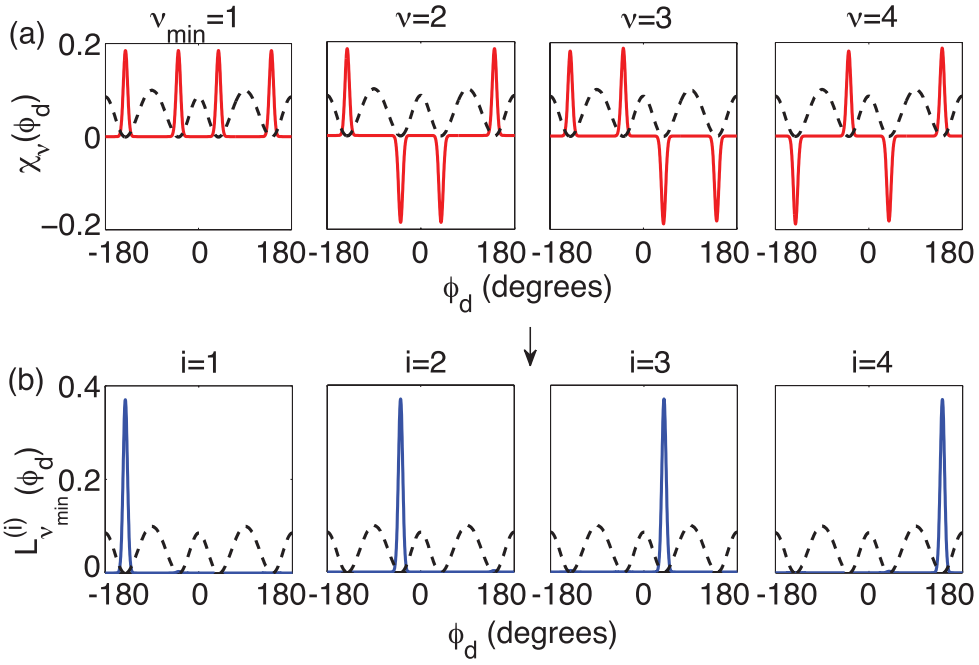

Figure 10.4: The field-free torsional states in units of $1/\sqrt{\text{degrees}}$. The (scaled) torsional potential is indicated with a dashed line. (a) The four first almost degenerate energy eigenstates lie 1.71 meV above the minimum of the torsional potential. From linear combinations of these we obtain the corresponding localized states shown in (b). The calculated energy differences are of the order 10^{-11} meV, and hence the lifetimes of the localized states are tens of milliseconds.

$\nu_{\min}$ the smallest ν of the four degenerate states. In Fig. 10.4 we show the first four energy eigenstates and the corresponding localized states along with the torsional potential. The experiment is generally carried out on a gas of molecules in a mixed state. At time t_0 prior to any pulses this state is given by the density matrix

$$\rho(t_0) = \sum_{\nu_{\min}} \sum_{i=1}^{4} P^{(i)}_{\nu_{\min}} |L^{(i)}_{\nu_{\min}}\rangle\langle L^{(i)}_{\nu_{\min}}| + \sum_{\nu} P_\nu |\chi_\nu\rangle\langle\chi_\nu|, \tag{10.4}$$

with the P's being weight factors that sum to unity, and where the latter sum includes the states above the torsional barrier. Due to the periodic boundary conditions, even the states with energies above the highest torsional barrier will be discrete rather than forming a continuum.

Table 10.1: The table lists the relevant polarizability components, $\alpha_{\rm ij}$, in atomic units of DFDBrBPh in the MF frame as a function of the dihedral angle, ϕ_d. The components are π-periodic and fulfill $\alpha_{\rm xx}(\phi_{\rm d}) = \alpha_{\rm xx}(\pi - \phi_{\rm d})$, $\alpha_{\rm yy}(\phi_{\rm d}) = \alpha_{\rm yy}(\pi - \phi_{\rm d})$ and $\alpha_{\rm xy}(\phi_{\rm d}) = -\alpha_{\rm xy}(\pi - \phi_{\rm d})$. Also, $\alpha_{\rm yx} = \alpha_{\rm xy}$.

$\phi_{\rm d}$	0°	15°	30°	45°	60°	75°	90°
$\alpha_{\rm xx}$	217.694	215.590	209.463	200.975	192.431	186.240	184.048
$\alpha_{\rm yy}$	92.352	95.201	102.634	112.658	122.693	130.015	132.639
$\alpha_{\rm xy}$	0.000	-9.488	-16.360	-18.810	-16.225	-9.295	0.000

10.3.2 Laser induced dynamics

The kick pulse introduces dynamics that we determine from the alignment potential created by the pulse. By convention the electric field is polarized along the LF X axis, and we use a Gaussian envelope (see Eq. 9.2). As for the polarizability tensor it has been calculated in the MF frame as a function of the dihedral angle by others (see Table 10.1) and must then be transformed into the LF frame. This is achieved by the application of directional cosine matrices [50]. We then arrive at the interaction

$$\begin{aligned} V_{\rm kick}(\Phi, \phi_d, t) = -\frac{1}{4} F_0^2(t) [&\alpha_{\rm xx}(\phi_d) \cos^2(\Phi + \eta\phi_d) \\ &+ \alpha_{\rm yy}(\phi_d) \sin^2(\Phi + \eta\phi_d) \\ &- 2\alpha_{\rm xy}(\phi_d) \cos(\Phi + \eta\phi_d) \sin(\Phi + \eta\phi_d)]. \end{aligned} \tag{10.5}$$

For the following analysis it is helpful to note a few qualitative features of the potential and we refer to Fig. 10.3 for graphical guidance. For a fixed dihedral angle the potential is minimal when the SMPA is parallel to the X axis. We will denote this by the $\|$-geometry. Conversely, the potential is maximal if the molecule is rotated 90° from the $\|$-geometry, and we will denote this by the $\perp$-geometry. Next, in the $\|$-geometry the potential favors a reduction of the dihedral angle, whereas an increase of the dihedral angle is resulting from the $\perp$-geometry. Hence, the overall effect of the kick pulse will be to align the molecules into the $\|$-geometry and drive a change of the dihedral angle.

We proceed with the quantitative analysis of the field-induced dynamics. The state $\chi_\nu(\phi_d)$ is no longer an eigenstate of the torsion when the kick pulse is applied, but will develop into a wave packet

$$\chi_\nu(\phi_d) \to \chi_\nu^\Phi(\phi_d, t) = \sum_{\nu'} c_{\nu'}^\Phi(t) e^{-iE_{\nu'}(t-t_0)} \chi_{\nu'}(\phi_d) \tag{10.6}$$

with the coefficients determined by

$$i\frac{d}{dt} c_{\nu'}^\Phi(t) = \sum_\nu \langle \chi_{\nu'} | V_{\rm kick}(\Phi, t) | \chi_\nu \rangle e^{-i(E_\nu - E_{\nu'})(t-t_0)} c_\nu^\Phi(t). \tag{10.7}$$

Once we find these new states of torsion the expectation value of the dihedral angle and of the kick potential from Eq. (10.5) are determined by tracing the product of the density matrix with the respective operators (cf. Chapter 4). From the latter we obtain the torque, which causes the molecule to rotate into the ‖-geometry. If the molecule lies at an angle Φ it is exposed to a torque $-\partial\langle V_{\mathrm{kick}}(\Phi,t)\rangle/\partial\Phi$ directed along the Z axis and hence achieves an angular acceleration given by

$$I\frac{d^2}{dt^2}\Phi(t) = -\frac{\partial\langle V_{\mathrm{kick}}(\Phi,t)\rangle}{\partial\Phi}. \tag{10.8}$$

Along with the initial conditions given at Eq. (10.4), the Eqs. (10.7) and (10.8) provide a set of coupled differential equations that may be integrated to obtain the coordinates $\Phi(t)$ and $\langle\phi_d(t)\rangle$ at time t. Rather than solving these coupled equations, we, however, assume that the angle Φ has the constant value Φ_0 during the short time interval of the kick pulse, and we integrate Eq. (10.8) twice to arrive at

$$\Phi(t) = \Phi_0 - t\frac{1}{I}\left(\frac{\partial}{\partial\Phi}\int_{-\infty}^{\infty} dt'\langle V_{\mathrm{kick}}(\Phi,t')\rangle\right)\Bigg|_{\Phi=\Phi_0}. \tag{10.9}$$

Consistently, we solve Eq. (10.7) with Φ fixed at Φ_0.

In the calculations below, we start with a distribution of values for Φ_0 in the interval $[-\pi,\pi]$ along with an initial density matrix, $\rho(t_0)$. We propagate each member of the distribution according to Eqs. (10.7) and (10.9). This procedure yields an ensemble of $\Phi(t)$'s and $\langle\phi_d(t)\rangle$'s and we finally employ the relations $\phi_{\mathrm{Br}}(t) = \Phi(t) + \eta\langle\phi_d(t)\rangle$ and $\phi_{\mathrm{F}}(t) = \Phi(t) - (1-\eta)\langle\phi_d(t)\rangle$ to find the angular distributions of bromines and fluorines.

10.4 Theoretical results

Before presenting the theoretical results on DFDBrBPh, we want to confirm the validity of the classical treatment of rotation. We apply the model to the simpler 3,5-difluoroiodobenzene (DFIB). Here, DFIB has its most polarizable axis fixed by a nanosecond laser pulse and is sequentially set into rotation about this axis by an orthogonally polarized femtosecond pulse. There is no torsion for this system and the rotational dynamics have been observed directly recently [106]. In Fig. 10.5, we compare the theoretical and experimental results. The agreement is good in the sense that the classical model is able to capture the time dependence of the alignment dynamics. To elaborate on the differences between theory and experiment, we note that a simple quantum calculation of the rotational dynamics exhibits the same time dependent behavior as the classical calculation, but with smaller modulations. Thus, the smaller experimental modulations must be due to quantum interferences. We ascribe difference in the theoretical and experimental intensities to the fact that the theoretical calculation does not include an average over the focal volume of the laser.

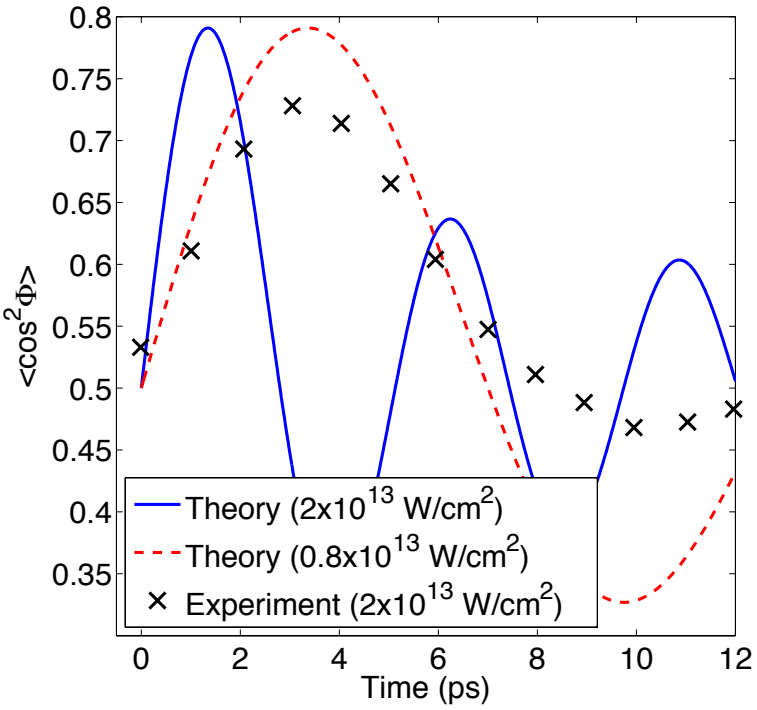

Figure 10.5: Comparison of the classical model for rotation at various intensities with the experiment of Ref. [106]. The theory captures the laser induced rotation within the first 12 ps, but generally overestimates the degree of angular confinement.

We now return to the DFDBrBPh system. Figure 10.6 shows the results of a calculation with laser parameters identical to the experimental values and an initial rotational temperature of 0 K. Prior to the kick pulse the angular distributions of the Br- and F-phenyl rings are isotropic as in the experiment. Maximum alignment of the SMPA occurs at 1.3 ps and the confinement of the F-phenyl rings at a large angle with respect to the kick pulse polarization (cf. middle panel, Fig. 10.6(a)) explains the distinct four-dot structure observed at $t_p = 1.47$ ps in the experimental F^+ ion image (Fig. 10.2(a)). At $t_p = 1.47$ ps the confinement of the Br-phenyl rings at a small angle with respect to the kick pulse polarization predicts a much less distinct four-dot structure. This is consistent with the Br^+ ion image, since the Coulomb explosion imaging technique broadens the observed distribution of the Br-phenyl rings. At $t_p = 2.47$ ps the angular localization of the F-phenyl rings has broadened (right panel, Fig. 10.6(a)) and a blurred four-dot structure is seen in agreement with the experimental result at $t_p = 2.47$ ps. The distribution of the Br-phenyl rings is also broadened (right panel, Fig. 10.6(b)), but remains localized around the kick pulse polarization fully consistent with the Br^+ ion

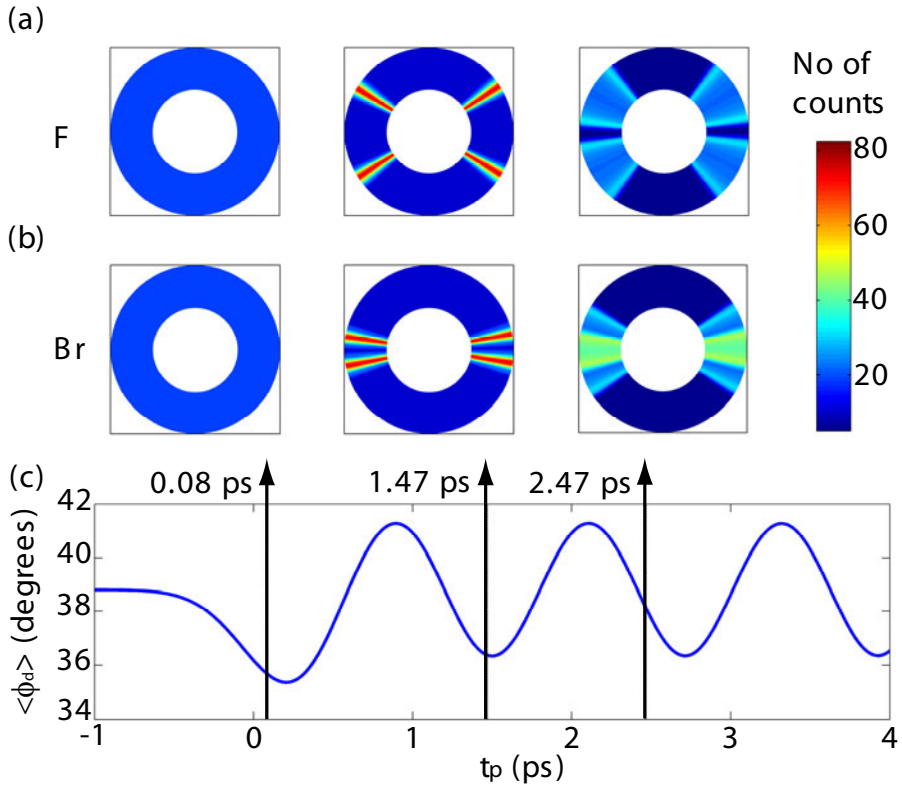

Figure 10.6: Angular distributions of (a) F-phenyl and (b) Br-phenyl rings at $t_p = 0.08$, 1.47 and 2.47 ps. (c) Expectation value of the dihedral angle for a molecule starting out with the SMPA aligned along the kick pulse polarization. The kick pulse is as in Fig. 10.2.

distribution, recorded at 2.47 ps.

The theoretical value $\langle\phi_d\rangle$ exhibits oscillations (Fig. 10.6(c)) with a period of ~ 1.2 ps and amplitude of $\sim 2.45°$. The period simply stems from the interference of the first localized state with the corresponding localized state lying 3.42 meV above. No further energy levels are populated appreciably at the intensity and duration used for the kick pulse in the experiment. The period agrees well with the experimental value (~ 1 ps), and smaller modulation in $\langle\phi_d\rangle$ is expected in the experiment ($\sim 0.6°$) since the SMPA is not pre-aligned and due to deviations from the stated laser peak intensity. The qualitative agreement of Figs. 10.2(b) and 10.6(c) corroborates the interpretation of the kick pulse inducing time-dependent torsional motion.

10.5 Outlook

We will now discuss some perspectives of the demonstrated laser control of torsion. First, we suggest a time-resolved study of de-racemization [107–111], where one enantiomer is steered into its mirror form. To obtain this, we will need to repeat the experiment with increased kick strength to overcome the torsional barrier. The interaction strength between the molecule and the kick pulse may be increased either through higher intensity, a longer kick pulse or by trains of synchronized kick pulses [112–114]. However, the molecules are fixed with the stereogenic axis along the LF Z axis by alignment and therefore both molecules with the Br-phenyl ring pointing in the positive and negative direction will occur (cf. Fig. 8.1). This inversion symmetry is an issue, because the R_a enantiomer with the Br-phenyl ring pointing in one direction has the same XY projection as the S_a enantiomer pointing in the opposite direction and the kick pulse interaction is only sensitive to this projection (cf. Eq. (10.5)). Consequently, as we convert R_a into S_a enantiomers, an equal number of molecules starting out as S_a enantiomers will be converted simultaneously into R_a enantiomers and altogether no de-racemization takes place.[4] We break the inversion symmetry of the C-C bond axis by orienting each molecule. This allows us to discriminate between the two enantiomeric forms. Theory [116, 117] and experiment [91–93, 118] show that orientation can be added to three dimensional alignment by combining the nanosecond alignment pulse with a static electric field. Finally, we optimize the excitation of torsional motion by eliminating initial rotation around the C-C bond through alignment of the SMPA (Fig. 10.3) prior to the kick pulse. This may be achieved by replacing the linearly polarized nanosecond pulse with an elliptically polarized nanosecond pulse [12, 119].

Assuming initial orientation and confinement of the SMPA, we have calculated the ϕ_d dynamics for both conformations the DFDBrBPh molecule with a reduced torsional barrier (see caption to Fig. 10.7). The results are shown in Fig. 10.7. Clearly, the present method would allow for a time-resolved study of the transition from one enantiomer into the other. A quantitative analysis of the efficiency of the process shows that after the pulse 99% of the molecules starting out as R_a has changed into S_a enantiomers, whereas only 13% of the S_a enantiomers changed into R_a. The inverse process causing an excess of R_a enantiomers, is achieved simply by inverting the orientation of the molecules.

We believe that the results presented in this paper also fuel the field of molecular junctions [120–122] with new possibilities. The conductivity of molecules like biphenyl will depend on the dihedral angle [123]. As such this type of molecules, if placed between two leads, can function as a molecular junction [69, 124–126] that may be used to control the charge flow and act as, e.g., a switch [119]. Importantly, we can realize quantum control of such a system by means of kick pulse schemes and in this way tailor very specific tor-

[4] Mathematically, the problem of the alignment interaction is that it is invariant under inversion of the molecular coordinates. No such invariant interaction can on its own lead to de-racemization [115].

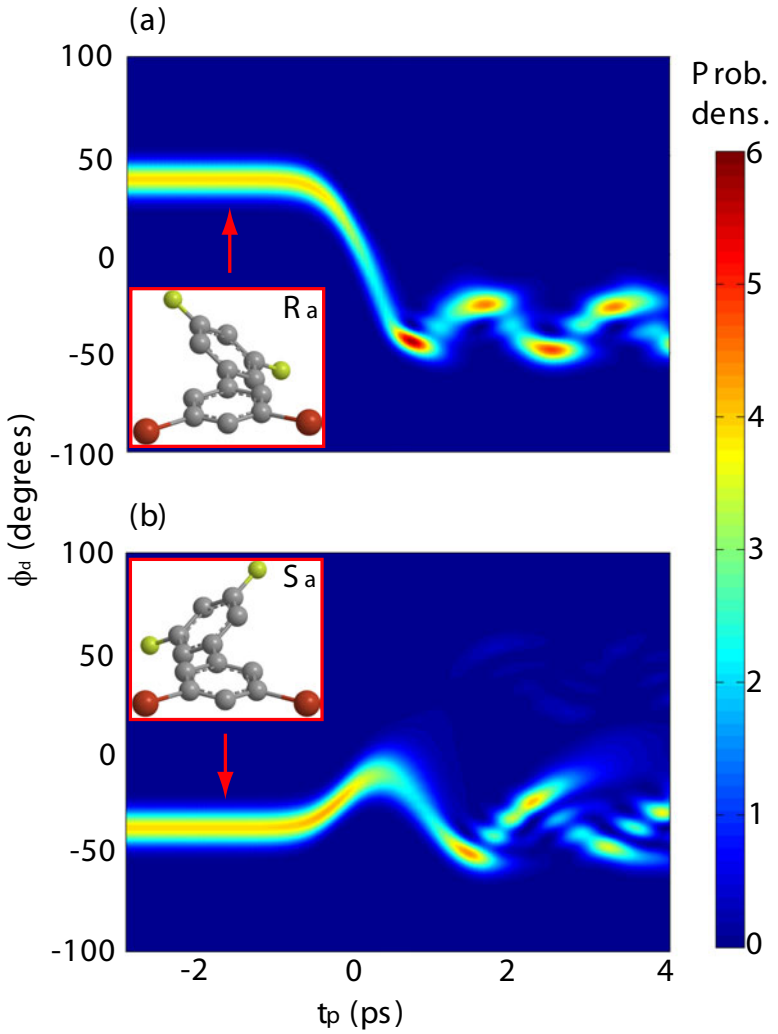

Figure 10.7: Time evolution of the dihedral angle for a molecule starting out as (a) an R_a or (b) an S_a enantiomer (see also Fig. 10.1). Initially, the molecule is three dimensionally oriented with the Br-phenyl end pointing out of the paper and the SMPA aligned at an angle of 13° with respect to the kick pulse polarization. The kick pulse triggering the torsional motion has a peak intensity of 1.2×10^{13} W/cm^2 and duration (FWHM) of 1.0 ps. The torsional potential is scaled down by 1/4 rather than by increasing the kick strength. Reduction of the torsional barrier is possible by modifying the aromatic rings or by using halogen substituted biphenylacetylene.

sional wave packets [127] to dictate the detailed time-dependent dihedral motion and thereby the current flow through the molecular junction. In the light of controllability, molecular junctions based on laser controlled torsion complements the available schemes, such as the mechanical break junctions [128] and the previously suggested resonantly light driven molecular junctions [129–131].

10.6 Summary

In summary, we introduced the first experiment to provide a femtosecond time-resolved study on laser controlled torsion of axially chiral molecules. The symmetry axis of DFDBrBPh molecules was held fixed in space by a long alignment laser pulse while a femtosecond kick pulse, polarized perpendicular to the fixed axis, was applied. The torsion as well as the overall rotation of the molecule was monitored with femtosecond time resolution using a delayed probe pulse. To explain the observations, we developed an original theoretical model. The model divides the dynamics of the molecule into a the rotation with classical behavior and quantum mechanical torsional dynamics. As such the model provides a transparent physical interpretation of essential features of laser controlled torsion of DFDBrBPh. Based on the theoretical model, we further discussed the extension of the experiment to a setup that will facilitate a femtosecond time-resolved study of de-racemization. Finally, we pointed to perspectives of using molecules like DFDBrBPh in molecular junctions in order to realize laser controlled charge flow.

Chapter 11

Summary (Dansk resumé)

In this thesis we have studied molecules in intense laser fields. We presented a semi-classical theory for treating the interaction of the charged system with a laser field. The radiation field is treated classically, but the molecular system is described using quantum mechanics. We then went on to study specific processes.

We studied the dynamics of H_2^+ in a laser field at wavelengths 400 to 600 nm. Specifically, we calculated the joint energy distribution of the outgoing electron and proton fragments in dissociative ionization. We saw that multi-photon structures appear and that these structures survive if we integrate out the nuclear energy dependence, but not if we integrate out the electron energy dependence. This is the first time the joint energy distribution of the nuclei and electron has been calculated, and we believe that our prediction of photon peaks could serve as a strong motivation to pursue experiments where the electron and nuclei are detected in coincidence.

After an introduction to high-order harmonic generation (HHG), we discussed methods to calculate ionization and HHG from more complex molecules than H_2^+. The basic idea is to partly or completely freeze the nuclei during the interaction with the laser pulse, since the laser pulse duration is short compared to the periods of vibration and rotation of large molecules. Even within this approximation, there is a need for further simplification, and to this end we invoked the strong-field approximation (SFA). Here, the basic assumptions are that the electron is unaffected by the laser field until the time of ionization and that the electron is unaffected by the attractive potential of the residual cation upon ionization.

We looked at the influence of molecular structure on HHG, a topic that has attracted much interest. Further, early indications that the harmonics can be used to reconstruct molecular orbitals brought even more attention to this topic. The reconstruction of molecular orbitals is far from trivial, since we showed that the imprint of the molecular structure stems from both the ionization step and the recombination step in HHG. Instead of molecular orbital reconstruction, we demonstrated a more straightforward application of HHG as a sensitive probe for the torsional angle between the two phenyl

rings in the biphenyl molecule. Finally, we saw that the multi-center structure of molecules in itself opens the possibility for elliptically polarized harmonic radiation with a linearly polarized driving pulse. This is a very distinct feature of HHG from molecules that is not observed in the case of atoms.

For molecules containing light atoms such as hydrogen, certain modes of vibration are comparable to the time scale of the laser driving the HHG. We presented a method to single out these modes using a Franck-Condon analysis. Once these modes are obtained, we can easily calculate the effect of nuclear motion on HHG. We exemplified this procedure with the methane and ethylene molecules. Not only the mass of the atoms in the molecule determines the importance of nuclear motion, but nuclear motion is important any time the equilibrium geometries of the neutral molecule and the cation differ significantly. This was, for instance, shown to be the case for the O_2 molecule.

The ability to use strong lasers to control the spatial orientation of molecules has opened the door for more detailed information about the molecular systems. Spatial orientation can be achieved through non-resonant laser induced alignment. We saw how alignment is often used as a pump to prepare the initial state, which is then followed by a pulse that probes the system through processes like ionization and HHG. The pre-alignment of the molecules reduces effects of averaging that would occur in the case of randomly aligned molecules. In an example with ionization from CS_2 molecules, the extra information gained by pre-alignment exposed shortcomings of the SFA.

Finally, we looked at a pioneering experiment of femtosecond time-resolved studies of torsional motion by a combination of aligning, kick and ionizing pulses. We developed an original theoretical model to explain the experiments. The model divides the dynamics of the molecule into rotation with classical behavior and quantum mechanical torsional dynamics. Based on the theoretical model we proposed schemes for ultrafast switching in molecular junctions and femtosecond time-resolved studies of de-racemization. As such, we believe that this work opens new directions of cross-disciplinary research firmly anchored in strong-field physics.

11.1 Dansk resumé

Vi har i denne afhandling præsenteret studier af molekyler i stærke laserfelter. Efter at have etableret det teoretiske kvantemekaniske fundament betragtede vi det simpleste af alle molekyler H_2^+. Vi studerede ioniseringsdynamikken af molekylet i laserfelter med intensiteter omkring 10^{14} W/cm^2 og bølgelængder mellem 400 og 600 nm. Helt konkret beregnede vi den kombinerede fordeling af kinetisk energi for elektron-proton fragmenterne, der produceres ved ionisering af molekylet. De resulterende beregninger har vist, at en fotonstruktur optræder. Denne struktur overlever, hvis vi integrerer fordelingen over protonenergien, men udvaskes hvis der integreres over elektronenergien. Det er første gang, den kombinerede energifordeling af kerner og elektroner er blevet studeret, og vi tror, at vores forudsigelse af fotontoppe vil være

en vigtig motivationsfaktor til at foretage eksperimenter, hvor elektroner og kerner detekteres i koincidens.

Efter at have studeret ionisering fra det simpleste molekyle introducerede vi høj harmonisk generation (HHG), det vil sige dannelsen af kohærent stråling med høj energi som følge af laser-molekyle vekselvirkningen. For at beregne ionisering og HHG fra systemer større end H_2^+, udnytter man, at kernebevægelsen i molekyler, dvs. rotation og vibration, generelt er meget langsommere end det tidsrum, hvor molekylet vekselvirker med det intense laserfelt. Det betyder, at kernebevægelse kan delvist eller fuldstændigt ignoreres, hvilket forenkler beregninger. Selv med denne simplifikation er der dog stadig et behov for yderligere reduktion af beskrivelsen af systemet. Dette kan nås med stærkfeltsapproksimationen (SFA), hvor de grundlægende antagelser, som nedsætter kompleksiteten, er at gå ud fra, at elektronen ikke påvirkes af laserfeltet, før ionisering, og at der ikke er nogen vekselvirking mellem elektronen og den tilbageværende kation efter ionisering.

Det har været en vigtig opgave indenfor de sidste fem år at kortlægge signaturen af molekylær struktur på HHG. Opgaven er til dels af fundamental interesse, men en ekstra relevans og øget interesse er affødt af tidlige indikationer på, at harmonisk stråling kan anvendes til at rekonstruere bølgefunktioner i molekylet og dermed potentielt bruges til at afbilde fysiske og kemiske reaktioner på atomar skala med rumlig og tidslig opløsning. Vi viste dog at molekylær struktur påvirker molekylet i to trin i HHG processen, nemlig når molekylet ioniseres og igen når elektronen rekombinerer, og det medfører, at rekonstruktionen af molekylære bølgefunktioner er mindre ligefrem end først antaget. Vi demonstrerede her en mere ligefrem, men stadig meget interessant anvedelse af HHG. Den dannede stråling kan tjene som en følsom probe for torsionsvinklen mellem de to fenylringe i molekylet bifenyl. Som et sidste eksempel på effekten af molekylær struktur på HHG viste vi, hvordan mulitcenterstrukturen af molekyler i sig selv kan lede til elliptisk polariseret harmonisk stråling fra en lineært polariseret drivpuls.

I tilfælde, hvor molekyler indeholder lette atomer såsom hydrogenatomer, vil visse af molekylets vibrationstilstande foregå på en tidsskala, der er sammenlignelig med varigheden af den laserpuls, som driver HHG. Vi præsenterede en metode til at identificere disse vibrationstilstande. Når først disse tilstande er bestemt, er det forholdvis simpelt at beregne effekten af kernebevægelse i molekylet. Vi så på to konkrete eksempler i form af molekylerne metan og etylen. Ikke kun massen af atomer i et molekyle er bestemmende for, om kernebevægelse har en stor effekt. Kernebevægelse har betydning nårsomhelst, ligevægtsgeometrien af kationen afviger betragteligt fra ligevægtsgeometrien af det neutrale molekyle. Et eksempel er O_2 molekylet.

Mange eksperimenter med ionisering eller HHG fra intense lasere lider under en midlingseffekt, fordi molekylerne, der probes, peger i alle retninger. Vi så, hvordan stærke lasere kan anvendes til at kontrollere den rumlige orientering af molekyler og dermed minimere denne midling, som har en tendens til at udvaske detaljer. Et eksempel, vi gav, var ionisering fra molekylet CS_2, hvor muligheden for at orientere molekylerne afslørede SFA'ens utilstrækkelighed.

Det førte til en dybere forståelse af hvilke fysiske processer, der var vigtige i eksperimentet.

Vi udvidede kontrollen af molekyler med laserere til at styre torsionen i et bifenyllignende molekyle. Vi så på et banebrydende eksperiment med femtosekundopløst måling af torsion ved kombination af tre laserpulser. En helt ny teoretisk model blev udviklet for at forklare eksperimentet. På basis af teorien pegede vi mod realiseringen af ultrahurtige molekylære kontakter og tidsopløste studier af den kemiske process deracemisering, hvor en blanding af molekyler renses.

Appendix A

Numerical solution of the TDSE

This appendix contains a review of the numerical methods used in Chapter 3 in relation to the numerical solution of the time dependent Schrödinger equation (TDSE). We introduce the Finite Element Discrete Variable Representation (FEDVR) and discuss how to find the outgoing scattering states.

A.1 FEDVR

We want to write out the details for using FEDVR. We will consider a particle of mass μ restricted to move along an axis x. The generalization to higher dimension in cartesian coordinates readily follows from this. The idea of FEDVR is to take a domain $[x_{\min}, x_{\max}]$ and split it into a number of elements, N_e. Then, within each element, expand the solution on a function basis giving the Discrete Variable Representation (DVR) (see Fig. A.1). The solution will be matched at each boundary between elements, but we will only match the function, not the derivative.

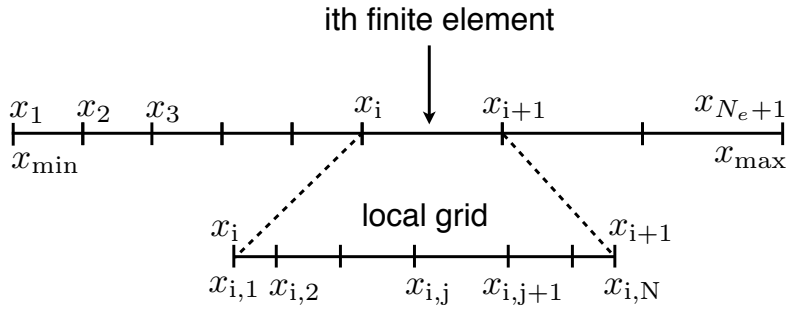

Figure A.1: One dimensional FEDVR grid.

We require our basis functions to have the following property

$$u_n(x_i) = \delta_{n,i} \tag{A.1}$$

where n runs from 1 to N over all the basis functions and i runs from 1 to N over the grid points in a given element. For the following discussion, we will assume that each element $[x_j, x_{j+1}]$ has been mapped to the logical domain $[-1, 1]$ using

$$x = \frac{x_{j+1} - x_j}{2} y + \frac{x_{j+1} + x_j}{2}, \quad y \in [-1, 1]. \tag{A.2}$$

We write our basis functions as

$$u_n(y) = \frac{(1 - y^2)\phi'_{N-2}(y)}{[(1 - y_n^2)\phi_{N-2}(y_n)]'(y - y_n)}, \tag{A.3}$$

where the ϕ_n's are the orthogonal polynomials of the *Gauss-Lobatto* quadrature (see page 888 of Ref. [132]) with the end points fixed at ± 1.

Next, we expand the wave functions as

$$\psi(x) = \sum_{j,n} c_{j,n} u_n^j(x). \tag{A.4}$$

The label j indicates where the u_n is defined and $\psi(x_n^j) = c_{j,n}$. Continuity of the wave function at element boundaries requires

$$\lim_{x \to x_{j,-}} \psi(x) = \lim_{x \to x_{j,+}} \psi(x) \Leftrightarrow c_{j,N} = c_{j+1,n}. \tag{A.5}$$

So,

$$\begin{aligned} \psi = & \sum_{j=2}^{N_e - 1} \left[\sum_{n=1}^{N-1} c_{j,n} u_n^j + c_{j,N} u_N^j \right] \\ & + \sum_{n=2}^{N} c_{N_e,n} u_n^{N_e} + \sum_{n=1}^{N-1} c_{1,n} u_n^1. \end{aligned} \tag{A.6}$$

We note that the terms $c_{j,N} u_N^j$ could also be replaced by $c_{j+1,1} u_1^{j+1}$, but that only one should be included to avoid double counting.

In Chapter 3 we need to solve the stationary Schrödinger equation (SSE) to find the initial laser field-free states of H_2^+ and to find the outgoing scattering states (see also Appendix A.2). If we put $\boldsymbol{c} = (c_{1,1}, c_{1,2}, \ldots, c_{N_e,N})^T$ the SSE may be expressed as

$$\boldsymbol{H}\boldsymbol{c} = E\boldsymbol{S}\boldsymbol{c}. \tag{A.7}$$

The overlap matrix is

$$\begin{aligned} (\boldsymbol{S})_{\alpha,\beta} = \langle u_{n'}^{j'} | u_n^j \rangle &= \delta_{j',j} \int_{x_j}^{x_{j+1}} dx\, u_{n'}^j(x) u_n^j(x) \\ &= \delta_{j',j} \frac{x_{j+1} - x_j}{2} w_n \delta_{n',n} \end{aligned} \tag{A.8}$$

with w_n weights of the Gauss-Lobatto quadrature [132]. This applies to all cases save $n' = 1$ or N. In those cases we need

$$\begin{aligned}(\boldsymbol{S})_{\alpha,\beta} &= \left(\langle u_N^{j'}| + \langle u_1^{j'+1}|\right)|u_n^j\rangle = \langle u_N^{j'}|u_n^j\rangle + \langle u_1^{j'+1}|u_n^j\rangle \\ &= \delta_{j',j}\frac{x_{j+1}-x_j}{2}\delta_{n,N}w_N + \delta_{j'+1,j}\frac{x_{j+1}-x_j}{2}\delta_{n,1}w_1 \end{aligned} \tag{A.9}$$

and

$$\begin{aligned}(\boldsymbol{S})_{\alpha,\beta} &= \left(\langle u_N^{j'}| + \langle u_1^{j'+1}|\right)\left(|u_N^j\rangle + |u_1^{j+1}\rangle\right) \\ &= \langle u_N^{j'}|u_N^j\rangle + \langle u_1^{j'+1}|u_1^{j+1}\rangle \\ &= \delta_{j',j}\frac{x_{j+1}-x_j}{2}w_N + \delta_{j',j}\frac{x_{j+2}-x_{j+1}}{2}w_1. \end{aligned} \tag{A.10}$$

Inspection of these expressions and the form of ψ from Eq. (A.6) shows that the overlap matrix consists of diagonal $N \times N$ block matrices in one element, and they overlap at the corners due to continuity. Thus, the overlap matrix is diagonal.

Next, we turn to the Hamiltonian which is composed of the kinetic energy matrix and the potential energy matrix. The kinetic energy matrix can be evaluated within each element, then the total matrix constructed

$$(\boldsymbol{T})^j_{n',n} = \langle u_{n'}|T|u_n\rangle = -\frac{1}{2\mu}\int_{x_j}^{x_{j+1}} dx\, u^j_{n'}(x)\frac{d^2}{dx^2}u^j_n(x) \tag{A.11}$$

$$\begin{aligned} &= -\frac{1}{2\mu}\frac{2}{x_{j+1}-x_j}\left[\delta_{n',N}u_n^{j\prime}(1) - \delta_{n',1}u_n^{j\prime}(-1)\right] \\ &+ \frac{1}{2\mu}\frac{2}{x_{j+1}-x_j}\int_{-1}^{1} dy\, u^{j\prime}_{n'}(y)u_n^{j\prime}(y). \end{aligned} \tag{A.12}$$

We go from Eq. (A.11) to Eq. (A.12) by integrating by parts. The question is whether the surface terms survive when we build the full kinetic energy matrix. To answer this questions we point out that if we integrate the kinetic energy by parts on the whole domain $[x_1, x_{N_e+1}]$, all basis functions satisfy $u = 0$ or $u' = 0$ at the domain boundaries, so the surface terms at x_1 and x_{N_e+1} vanish. We can then split the remaining integral into a sum of integrals over subintervals corresponding to the elements, which leads to the expression of Eq. (A.12) minus the surface terms. This is called the *weak form* while the second derivative version of Eq. (A.11) is the *strong form*. We currently employ the weak form, because we use basis functions with a discontinuous first derivative. Thus,

$$(\boldsymbol{T})^j_{n',n} = \frac{1}{2\mu}\frac{2}{x_{j+1}-x_j}\sum_{i+1}^{N} w_i u^{j\prime}_{n'}(y_i)u^{j\prime}_n(y_i) \tag{A.13}$$

The full kinetic energy matrix is composed of these elemental T-matrices. Finally, the potential energy is simply

$$\langle u^{j'}_{n'}|V|u^j_n\rangle = \delta_{j',j}\delta_{n',n}\frac{x_{j+1}-x_j}{2}w_n V(x_n). \tag{A.14}$$

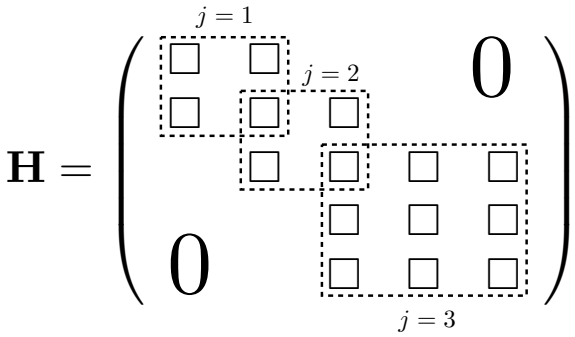

Figure A.2: Example of the banded Hamiltonian matrix for three elements with a (2/2/3) basis.

Returning now to equation (A.7) we have $\boldsymbol{S}$ diagonal and $\boldsymbol{H}$ banded (see Fig. A.2), and we may therefore convert it into a standard eigenvalue problem using a Cholesky decomposition

$$\boldsymbol{S} = \boldsymbol{L}\boldsymbol{L}^T, \tag{A.15}$$

with $\boldsymbol{L} = \boldsymbol{S}^{1/2}$ simply the square root of the diagonal elements. Then, defining

$$\tilde{\boldsymbol{H}} = \boldsymbol{L}^{-1}\boldsymbol{H}(\boldsymbol{L}^T)^{-1}, \boldsymbol{d} = \boldsymbol{L}^T\boldsymbol{c} \tag{A.16}$$

we may rephrase Eq. (A.7) as

$$\tilde{\boldsymbol{H}}\boldsymbol{d} = E\boldsymbol{d} \tag{A.17}$$

Finally, we address the imposition of boundary conditions. With the Gauss-Lobatto quadrature we automatically get the case $\psi' = 0$ if nothing further is done. To impose $\psi = 0$, we simply leave out u_1 in the left-most element or u_N in the right-most.

A.2 Finding the outgoing scattering states

In this section we will explain how to use the FEDVR as detailed in the previous section to find outgoing continuum scattering states, i.e., the solutions of Eqs. (3.15) and (3.16). In other words, we want to solve the SSE, but we are looking for non-bound states. To within a proportionality constant, the solution at any chosen energy E is uniquely specified by the boundary condition at the origin (ψ or $\psi' = 0$). At sufficiently large distances $x \geq x_0$ the solution we seek is a linear combination of Coulomb functions [133] f and g with constant coefficients given by an amplitude A and a phase δ

$$\psi(x) = A[f(x)\cos(\delta) - g(x)\sin(\delta)], \quad x \geq x_0. \tag{A.18}$$

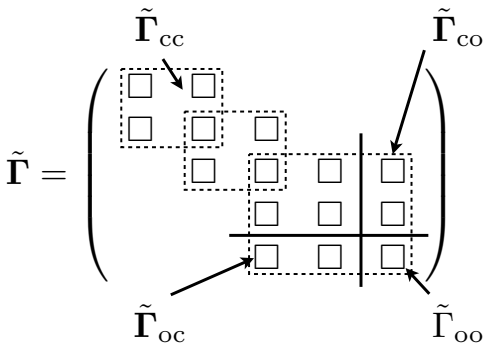

Figure A.3: The $\tilde{\mathbf{\Gamma}}$ matrix illustrated in the case of three elements with a (2/2/3) basis.

We may phrase this as a generalized eigenvalue problem using the eigenchannel R-matrix formulation [134] (our notation and definitions are carried over from the previous section)

$$\tilde{\mathbf{\Gamma}}\boldsymbol{d} = b\tilde{\mathbf{\Lambda}}\boldsymbol{d}, \tag{A.19}$$

$$\tilde{\mathbf{\Gamma}} = \boldsymbol{L}^{-1}\boldsymbol{T}(\boldsymbol{L}^T)^{-1} - E\mathbb{I} + \boldsymbol{V}, \tag{A.20}$$

$$(\boldsymbol{V})_{m,n} = V(x_n)\delta_{m,n} \text{ with } x_n \text{ element boundaries}, \tag{A.21}$$

$$(\tilde{\mathbf{\Lambda}})_{m,n} = \frac{1}{2\mu}\delta_{m,n}\left[\frac{2}{w_1(x_2-x_1)}\delta_{m,1} - \frac{2}{w_{N_e+1}(x_{N_e+1}-x_{N_e})}\delta_{m,N}\right] \tag{A.22}$$

We solve this by dividing the $\tilde{\mathbf{\Gamma}}$ and $\tilde{\mathbf{\Lambda}}$ matrices into open (o) and closed (c) spaces according to the basis functions on the boundary. Closed means that the basis function is zero at the boundary (see Fig. A.3). Note, there is only one non-zero element at the boundary. Accordingly $\boldsymbol{d} = (\boldsymbol{d}_{\mathrm{c}}^T, d_{\mathrm{o}})^T$. We then just have to solve

$$\Omega d_{\mathrm{o}} = b\tilde{\Lambda}_{\mathrm{o,o}}d_{\mathrm{o}}, \tag{A.23}$$

where

$$\Omega = \tilde{\Gamma}_{\mathrm{o,o}} - \tilde{\mathbf{\Gamma}}_{\mathrm{o,c}}\tilde{\mathbf{\Gamma}}_{\mathrm{c,c}}^{-1}\tilde{\mathbf{\Gamma}}_{\mathrm{c,o}}. \tag{A.24}$$

We find the inverted matrix, $\tilde{\mathbf{\Gamma}}_{\mathrm{c,c}}^{-1}$ by writing

$$\tilde{\mathbf{\Gamma}}_{\mathrm{c,c}}^{-1}\tilde{\mathbf{\Gamma}}_{\mathrm{c,o}} = \boldsymbol{B}_{\mathrm{c,o}} \tag{A.25}$$

$$\tilde{\mathbf{\Gamma}}_{\mathrm{c,o}} = \tilde{\mathbf{\Gamma}}_{\mathrm{c,c}}\boldsymbol{B}_{\mathrm{c,o}} \tag{A.26}$$

and solve as a linear system. We will also want the eigenvector and $\boldsymbol{d}_{\mathrm{c}}$ is given by

$$\boldsymbol{d}_{\mathrm{c}} = -\boldsymbol{B}_{\mathrm{c,o}}d_{\mathrm{o}}. \tag{A.27}$$

The unknown

$$b = \frac{\Omega}{\tilde{\Lambda}_{\mathrm{o,o}}} \tag{A.28}$$

that we get from solving Eq. (A.23) is the log derivative of the physical wave function and matching at the boundary gives

$$\left.\frac{\psi'(x)}{\psi(x)}\right|_{x=x_0} = \left.\frac{f'\cos\delta - g'\sin\delta}{f\cos\delta - g\sin\delta}\right|_{x=x_0} = -b \tag{A.29}$$

From this we derive the phase shift

$$\tan\delta = \frac{f' + bf}{g' + bg} \tag{A.30}$$

With the phase shift at hand, we finally use Eq. (A.18) to match the solutions, i.e., determine A and get the properly energy-normalized solution.

Appendix B

Determining Franck-Condon integrals

In this appendix we provide a method to determine Franck-Condon (FC) integrals, i.e., $\langle \chi_{f,\boldsymbol{\nu}} | \chi_{i,0} \rangle$, between a vibrationally-cold initial state, $\chi_{i,0}$, and a vibrationally-excited final state, $\chi_{f,\boldsymbol{\nu}}$, where the subscript $\boldsymbol{\nu}$ denotes the excitation level.

For a non-linear molecule with N atoms we may write the total nuclear Hamiltonian as

$$H_{\text{nuc}} = \frac{1}{2} \sum_{i=1}^{3N} \left(-\frac{\partial^2}{\partial q_i^2} + \sum_{j=1}^{3N} \frac{\partial^2}{\partial q_i \partial q_j} V_{\text{nuc}}(\boldsymbol{q}) \Big|_{\boldsymbol{q}=\boldsymbol{0}} q_i q_j \right), \tag{B.1}$$

where we use a harmonic approximation for the nuclear potential energy. The vector $\boldsymbol{q} = (q_1, q_2, \ldots, q_{3N})$ contains the mass-weighted coordinates, where q_i is related to the displacement x_i of the ith atom of mass M_i from the equilibrium position through the relation $q_i = \sqrt{M_i} x_i$. The nuclear potential energy, V_{nuc}, is found by solving the electronic Schrödinger equation within the Born-Oppenheimer approximation and depends on the electronic state.

The cross terms in the potential energy of Eq. (B.1) may be avoided by an appropriate coordinate transformation which leads to the normal coordinates, $\boldsymbol{Q}$, with the corresponding Hamiltonian of the form

$$H_{\text{nuc}} = \frac{1}{2} \sum_{i=1}^{3N} \left(-\frac{\partial^2}{\partial Q_i^2} + \omega_i^2 Q_i^2 \right). \tag{B.2}$$

Here ω_i is the frequency of mode i. Some ω_i's turn out to be zero and simply correspond to translations and rotations of the molecule. The remaining N_m modes ($3N - 6$ for non-linear molecules and $3N - 5$ for linear molecules), correspond to vibrations.

To calculate equilibrium geometries and normal modes one may use standard chemistry packages. For the work on methane presented in Chapter 7 this has been done using the hybrid density functional B3LYP level of theory

in conjunction with the triple-ζ valence basis set as implemented in GAUSSIAN [135].

The Hamiltonian in Eq. (B.2) is a sum of terms each depending on only one normal coordinate. Therefore, the vibrational wave functions describing the initial state (the neutral molecule) and the final state (the cation) can be expressed as a product of wave functions for each mode. Further, each of the wave functions are simple harmonic oscillator states

$$\chi_{i,0}(\mathbf{Q}') = \left(\det \mathbf{\Gamma}'/\pi^{N_m}\right)^{\frac{1}{4}} \exp\left(-\frac{1}{2}\mathbf{Q}'^{\dagger}\mathbf{\Gamma}'\boldsymbol{Q}'\right), \tag{B.3}$$

and

$$\begin{aligned}\chi_{f,\boldsymbol{\nu}}(\mathbf{Q}) = &\left(\det \mathbf{\Gamma}/\pi^{N_m}\right)^{\frac{1}{4}} \exp\left(-\frac{1}{2}\mathbf{Q}^{\dagger}\mathbf{\Gamma}\boldsymbol{Q}\right) \\ &\times \prod_{j=1}^{N_m} (2^{\nu_j}\nu_j!)^{-1/2}\, H_{\nu_j}(\mathbf{\Gamma}^{1/2}\boldsymbol{Q}).\end{aligned} \tag{B.4}$$

Here, $\mathbf{\Gamma}$ is a diagonal matrix with elements $\Gamma_{j,j} = 1/\omega_j$, where ω_j is the vibrational frequency of mode j, N_m is the number of vibrational degrees of freedom, the index $\boldsymbol{\nu} = (\nu_1, \nu_2, \ldots, \nu_{N_m})$ is a vector of vibrational excitations and H_{ν_j} is the ν_jth Hermite polynomial. For a vibrationally-cold state, $\boldsymbol{\nu} = (0_1, 0_2, \ldots, 0_{N_m}) \equiv 0$. The normal coordinates of the initial state and the final state are related by the simple transformation [136],

$$\mathbf{Q}' = \mathbf{J}\mathbf{Q} + \mathbf{\Delta}, \tag{B.5}$$

where $\mathbf{J}$ is the Duschinsky matrix and the vector $\mathbf{\Delta}$ expresses the geometry change in the final state. The $\mathbf{J}$ matrix reflects the mapping of the normal coordinates of the initial-state onto those of the final-state.

The multi-dimensional FC integral, within the harmonic approximation, reads

$$\begin{aligned}\langle \chi_{f,\boldsymbol{\nu}} \mid \chi_{i,0} \rangle = N \int &dQ_1 \ldots dQ_{N_m} H_{\nu_1}(\Gamma_1 Q_1) \ldots \\ &\times H_{\nu_{N_m}}(\Gamma_{N_m} Q_{N_m}) \\ &\times \exp\left[-\frac{1}{2}\Gamma_1 Q_1^2 - \ldots - \frac{1}{2}\Gamma_{N_m} Q_{N_m}^2\right] \\ &\times \exp\left[-\frac{1}{2}\Gamma'_1 {Q'_1}^2 - \ldots - \frac{1}{2}\Gamma'_{N_m} {Q'_{N_m}}^2\right].\end{aligned} \tag{B.6}$$

where the normalization factor is given by

$$N = \prod_{j=1}^{N_m} \left(\frac{\Gamma_j^{1/2}\Gamma_j'^{1/2}}{\pi 2^{\nu_j}\nu_j!}\right)^{1/2}. \tag{B.7}$$

When evaluating the integrals, a considerable simplification is introduced by assuming that the off-diagonal elements in **J** (see Eq. (B.5)) are very small so that

$$\begin{aligned} Q'_j &= J_{j,1}Q_1 + J_{j,2}Q_2 + \ldots + J_{j,N_m}Q_{N_m} + \Delta_j \\ &\approx J_{j,j}Q_1 + \Delta_j. \end{aligned} \tag{B.8}$$

Accordingly, the multi-dimensional FC integral reduces to a product of one-dimensional integrals,

$$\begin{aligned} \langle \chi_{f,\boldsymbol{\nu}} \mid \chi_{i,0} \rangle = \prod_j^{N_m} \int dQ_j H_{\nu_j}(\Gamma_j Q_j) \\ \times \exp\left[-\frac{1}{2}\Gamma_j Q_j^2 - \frac{1}{2}\Gamma'_j (J_{j,j}Q_j + \Delta_j)^2 \right]. \end{aligned} \tag{B.9}$$

The Ansbacher recurrence relations are used to obtain the overlap integrals of the one-dimensional harmonic wave functions [137].

Bibliography

[1] C. B. Madsen and L. B. Madsen, *High-order harmonic generation from arbitrarily oriented diatomic molecules including nuclear motion and field-free alignment*, Phys. Rev. A **74**, 023403 (2006).

[2] C. B. Madsen, A. S. Mouritzen, T. K. Kjeldsen and L. B. Madsen, *Effects of orientation and alignment in high-order harmonic generation and above-threshold ionization*, Phys. Rev. A **76**, 035401 (2007).

[3] C. B. Madsen and L. B. Madsen, *Theoretical studies of high-order harmonic generation: Effects of symmetry, degeneracy, and orientation*, Phys. Rev. A **76**, 043419 (2007).

[4] V. Kumarappan, L. Holmegaard, C. Martiny, C. B. Madsen, T. K. Kjeldsen, S. S. Viftrup, L. B. Madsen and H. Stapelfeldt, *Multiphoton Electron Angular Distributions from Laser-Aligned CS_2 Molecules*, Phys. Rev. Lett. **100**, 093006 (2008).

[5] C. B. Madsen, L. B. Madsen, S. S. Viftrup, M. P. Johansson, T. B. Poulsen, L. Holmegaard, V. Kumarappan, K. A. Jørgensen and H. Stapelfeldt, *Manipulating the Torsion of Molecules by Strong Laser Pulses*, Phys. Rev. Lett. **102**, 073007 (2009).

[6] C. B. Madsen, L. B. Madsen, S. S. Viftrup, M. P. Johansson, T. B. Poulsen, L. Holmegaard, V. Kumarappan, K. A. Jørgensen and H. Stapelfeldt, *A combined experimental and theoretical study on realizing and using laser controlled torsion of molecules*, J. Chem. Phys. **130**, 234310 (2009).

[7] A. Etches, C. B. Madsen and L. B. Madsen, *Inducing elliptically polarized high-order harmonics from aligned molecules with linearly polarized femtosecond pulses*, Phys. Rev. A **81**, 013409 (2010).

[8] C. B. Madsen, M. Abu-samha and L. B. Madsen, *High-order harmonic generation from polyatomic molecules including nuclear motion and a nuclear modes analysis*, Phys. Rev. A **81**, 043413 (2010).

[9] C. B. Madsen, F. Anis, L. B. Madsen and B. D. Esry, *Correlated electron-nuclear continuum energy distribution following strong-field ionization of H_2^+*, in preparation.

[10] C. B. Madsen and L. B. Madsen, *Influence of the torsion on high-order harmonic generation from biphenyl*, in preparation.

[11] J. H. Posthumus, *The dynamics of small molecules in intense laser fields*, Reports on Progress in Physics **67**, 623 (2004).

[12] H. Stapelfeldt and T. Seideman, *Colloquium: Aligning molecules with strong laser pulses*, Rev. Mod. Phys. **75**, 543 (2003).

[13] A. H. Zewail, *Femtochemistry: Atomic-Scale Dynamics of the Chemical Bond*, J. Phys. Chem. A **104**, 5660 (2000).

[14] M. Drescher, M. Hentschel, R. Kienberger, G. Tempea, C. Spielmann, G. A. Reider, P. B. Corkum and F. Krausz, *X-ray Pulses Approaching the Attosecond Frontier*, Science **291**, 1923 (2001).

[15] M. Lein, N. Hay, R. Velotta, J. P. Marangos and P. L. Knight, *Interference effects in high-order harmonic generation with molecules*, Phys. Rev. A **66**, 023805 (2002).

[16] T. Kanai, S. Minemoto and H. Sakai, *Quantum interference during high-order harmonic generation from aligned molecules*, Nature **435**, 470 (2005).

[17] S. Baker, J. S. Robinson, C. A. Haworth, H. Teng, R. A. Smith, C. C. Chirilă, M. Lein, J. W. G. Tisch and J. P. Marangos, *Probing Proton Dynamics in Molecules on an Attosecond Time Scale*, Science **312**, 424 (2006).

[18] A.-T. Le, R. D. Picca, P. D. Fainstein, D. A. Telnov, M. Lein and C. D. Lin, *Theory of high-order harmonic generation from molecules by intense laser pulses*, J. Phys. B: At. Mol. Opt. Phys. **41**, 081002 (2008).

[19] J. Itatani, J. Levesque, D. Zeidler, H. Niikura, H. Pépin, J. C. Kieffer, P. B. Corkum and D. M. Villeneuve, *Tomographic imaging of molecular orbitals*, Nature **432**, 867 (2004).

[20] S. Haessler, J. Caillat, W. Boutu, C. Giovanetti-Teixeira, T. Ruchon, T. Auguste, Z. Diveki, P. Breger, A. Maquet, B. Carre, R. Taieb and P. Salieres, *Attosecond imaging of molecular electronic wavepackets*, Nature Phys. **6**, 200 (2010).

[21] F. Krausz and M. Ivanov, *Attosecond physics*, Rev. Mod. Phys. **81**, 163 (2009).

[22] D. J. Griffiths, *Introduction to electrodynamics* (Prentice Hall, New Jersey, 1999), 3rd edition.

[23] B. H. Bransden and C. J. Joachain, *Physics of atoms and molecules* (Prentice Hall, Harlow, 2003), 2nd edition.

[24] L. B. Madsen and D. Dimitrovski, *Time-resolved subcycle dynamics: Importance of physical fields and gauge invariance*, Phys. Rev. A **78**, 023403 (2008).

[25] A. F. Starace, *Length and Velocity Formulas in Approximate Oscillator-Strength Calculations*, Phys. Rev. A **3**, 1242 (1971).

[26] L. B. Madsen, *Gauge invariance in the interaction between atoms and few-cycle laser pulses*, Phys. Rev. A **65**, 053417 (2002).

[27] W. C. Henneberger, *Perturbation Method for Atoms in Intense Light Beams*, Phys. Rev. Lett. **21**, 838 (1968).

[28] K. C. Kulander, F. H. Mies and K. J. Schafer, *Model for studies of laser-induced nonlinear processes in molecules*, Phys. Rev. A **53**, 2562 (1996).

[29] B. Feuerstein and U. Thumm, *Fragmentation of H_2^+ in strong 800-nm laser pulses: Initial-vibrational-state dependence*, Phys. Rev. A **67**, 043405 (2003).

[30] S. Saugout, C. Cornaggia, A. Suzor-Weiner and E. Charron, *Ultrafast Electronuclear Dynamics of H_2 Double Ionization*, Phys. Rev. Lett. **98**, 253003 (2007).

[31] A. I. Kuleff, J. Breidbach and L. S. Cederbaum, *Multielectron wave-packet propagation: General theory and application*, J. Chem. Phys. **123**, 044111 (2005).

[32] F. Martín, *Ionization and dissociation using B-splines: photoionization of the hydrogen molecule*, J. Phys. B: At. Mol. Opt. Phys. **32**, R197 (1999).

[33] L. B. Madsen, L. A. A. Nikolopoulos, T. K. Kjeldsen and J. Fernández, *Extracting continuum information from $\Psi(t)$ in time-dependent wave-packet calculations*, Phys. Rev. A **76**, 063407 (2007).

[34] J. S. Parker, L. R. Moore, K. J. Meharg, D. Dundas and K. T. Taylor, *Double-electron above threshold ionization of helium*, J. Phys. B: At. Mol. Opt. Phys. **34**, L69 (2001).

[35] A. McPherson, G. Gibson, H. Jara, U. Johann, T. S. Luk, I. A. McIntyre, K. Boyer and C. K. Rhodes, *Studies of multiphoton production of vacuum-ultraviolet radiation in the rare gases*, J. Opt. Soc. Am. B **4**, 595 (1987).

[36] P. B. Corkum, *Plasma Perspective on Strong-field Multiphoton Ionization*, Phys. Rev. Lett. **71**, 1994 (1993).

[37] B. Sundaram and P. W. Milonni, *High-order harmonic generation: Simplified model and relevance of single-atom theories to experiment*, Phys. Rev. A **41**, 6571 (1990).

[38] D. J. Diestler, *Harmonic genereation: Quantum-electrodynamical theory of the harmonic photon-number spectrum*, Phys. Rev. A **78**, 033814 (2008).

[39] V. Tosa, H. T. Kim, I. J. Kim and C. H. Nam, *High-order harmonic generation by chirped and self-guided femtosecond laser pulses. I. Spatial and spectral analysis*, Phys. Rev. A **71**, 063807 (2005).

[40] X. Zhou, X. M. Tong, Z. X. Zhao and C. D. Lin, *Alignment dependence of high-order harmonic generation from N_2 and O_2 molecules in intense laser fields*, Phys. Rev. A **72**, 033412 (2005).

[41] F. H. M. Faisal, A. Abdurrouf, K. Miyazaki and G. Miyaji, *Origin of Anomalous Spectra of Dynamic Alignments Observed in N_2 and O_2*, Phys. Rev. Lett. **98**, 143001 (2007).

[42] R. Torres, N. Kajumba, J. G. Underwood, J. S. Robinson, S. Baker, J. W. G. Tisch, R. de Nalda, W. A. Bryan, R. Velotta, C. Altucci, I. C. E. Turcu and J. P. Marangos, *Probing Orbital Structure of Polyatomic Molecules by High-Order Harmonic Generation*, Phys. Rev. Lett. **98**, 203007 (2007).

[43] J. J. Sakurai, *Modern quantum mechanics* (Addison-Wesley Publishing Company, New York, 1994), revised edition.

[44] M. Lewenstein, P. Balcou, M. Y. Ivanov, A. L'Huillier and P. B. Corkum, *Theory of high-harmonic generation by low-frequency laser fields*, Phys. Rev. A **49**, 2117 (1994).

[45] M. Lein, *Attosecond Probing of Vibrational Dynamics with High-Harmonic Generation*, Phys. Rev. Lett. **94**, 053004 (2005).

[46] M. W. Schmidt, K. K. Baldridge, J. A. Boatz, S. T. Elbert, M. S. Gordon, J. H. Jensen, S. Koseki, N. Matsunaga, K. A. Nguyen, S. Su, T. L. Windus, M. Dupuis and J. A. M. Jr, *General atomic and molecular electronic structure system*, J. Comput. Chem. **14**, 1347 (1993).

[47] C. C. Chirilă and M. Lein, *Strong-field approximation for harmonic generation in diatomic molecules*, Phys. Rev. A **73**, 023410 (2006).

[48] C. F. de Morrison Faria, *High-order harmonic generation in diatomic molecules: A quantum-orbit analysis of interference patterns*, Phys. Rev. A **76**, 043407 (2007).

[49] I. S. Gradshteyn and I. M. Ryzhik, *Table of integrals, series and products* (Academic Press, New York, 2000), 6th edition.

[50] R. N. Zare, *Angular momentum: understanding spatial aspects in chemistry and physics* (John Wiley, New York, 1988).

[51] M. Y. Kuchiev and V. N. Ostrovsky, *Quantum theory of high harmonic generation as a three-step process*, Phys. Rev. A **60**, 3111 (1999).

[52] K. Burnett, V. C. Reed, J. Cooper and P. L. Knight, *Calculation of the background emitted during high-harmonic generation*, Phys. Rev. A **45**, 3347 (1992).

[53] K. Burnett, V. C. Reed, J. Cooper and P. L. Knight, *Calculation of the background emitted during high-harmonic generation*, Phys. Rev. A **45**, 3347 (1992).

[54] A. D. Bandrauk, S. Chelkowski, D. J. Diestler, J. Manz and K.-J. Yuan, *Quantum simulation of high-order harmonic spectra of the hydrogen atom*, Phys. Rev. A **79**, 023403 (2009).

[55] T. K. Kjeldsen and L. B. Madsen, *Strong-field ionization of diatomic molecules and companion atoms: Strong-field approximation and tunneling theory including nuclear motion*, Phys. Rev. A **71**, 023411 (2005).

[56] A. Rouzèe, S. Guèrin, V. Boudon, B. Lavorel and O. Faucher, *Field-free alignment of ethylene molecule*, Phys. Rev. A **73**, 033418 (2006).

[57] J. G. Underwood, B. J. Sussman and A. Stolow, *Field-Free Three Dimensional Molecular Axis Alignment*, Phys. Rev. Lett. **94**, 143002 (2005).

[58] J. Levesque, Y. Mairesse, N. Dudovich, H. Pépin, J.-C. Kieffer, P. B. Corkum and D. M. Villeneuve, *Polarization State of High-Order Harmonic Emission from Aligned Molecules*, Phys. Rev. Lett. **99**, 243001 (2007).

[59] X. Zhou, R. Lock, N. Wagner, W. Li, H. C. Kapteyn and M. M. Murnane, *Elliptically Polarized High-Order Harmonic Emission from Molecules in Linearly Polarized Laser Fields*, Phys. Rev. Lett. **102**, 073902 (2009).

[60] M. B. Gaarde, J. L. Tate and K. J. Schafer, *Macroscopic aspects of attosecond pulse generation*, J. Phys. B: At. Mol. Opt. Phys. **41**, 132001 (2008).

[61] E. Lorin, S. Chelkowski and A. D. Bandrauk, *Attosecond pulse generation from aligned molecules—dynamics and propagation in* H_2^+, New J. Phys. **10**, 025033 (2008).

[62] M. Lein, N. Hay, R. Velotta, J. P. Marangos and P. L. Knight, *Role of the Intramolecular Phase in High-Harmonic Generation*, Phys. Rev. Lett. **88**, 183903 (2002).

[63] M. Born and E. Wolf, *Principles of Optics: Electromagnetic Theory of Propagation, Interference and Diffraction of Light* (Pergamon Press, 1970), 4th edition.

[64] C. C. Chirilă and M. Lein, *Explanation for the smoothness of the phase in molecular high-order harmonic generation*, Phys. Rev. A **80**, 013405 (2009).

[65] O. Smirnova, S. Patchkovskii, Y. Mairesse, N. Dudovich, D. Villeneuve, P. Corkum and M. Y. Ivanov, *Role of the Intramolecular Phase in High-Harmonic Generation*, Phys. Rev. Lett. **102**, 063601 (2009).

[66] M. Y. Ivanov, T. Brabec and N. Burnett, *Coulomb corrections and polarization effects in high-intensity high-harmonic emission*, Phys. Rev. A **54**, 742 (1996).

[67] S. Ramakrishna, P. A. J. Sherratt, A. D. Dutoi and T. Seideman, *Origin and implication of ellipticity in high-order harmonic generation from aligned molecules*, Phys. Rev. A **81**, 021802 (2010).

[68] B. Zimmermann, M. Lein and J. M. Rost, *Analysis of recombination in high-order harmonic generation in molecules*, Phys. Rev. A **71**, 033401 (2005).

[69] M. Čížek, M. Thoss and W. Domcke, *Charge transport through a flexible molecular junction*, Czechoslovak Journal of Physics **55**, 189 (2005).

[70] S. Patchkovskii, *Nuclear Dynamics in Polyatomic Molecules and High-Order Harmonic Generation*, Phys. Rev. Lett. **102**, 253602 (2009).

[71] P. Atkins and R. Friedman, *Molecular quantum mechanics* (Oxford University Press, Oxford, 2005), 4th edition.

[72] G. H. Dunn, *Franck-Condon Factors for the Ionization of H_2 and D_2*, J. Chem. Phys. **44**, 2592 (1966).

[73] S. Baker, J. S. Robinson, M. Lein, C. C. Chirilă, R. Torres, H. C. Bandulet, D. Comtois, J. C. Kieffer, D. M. Villeneuve, J. W. G. Tisch and J. P. Marangos, *Dynamic Two-Center Interference in High-Harmonic Generation from Molecules with Attosecond Nuclear Motion*, Phys. Rev. Lett. **101**, 053901 (2008).

[74] C. R. Calvert, T. Birkeland, R. B. King, I. D. Williams and J. F. McCann, *Quantum chessboards in the deuterium molecular ion*, J. Phys. B: At. Mol. Opt. Phys. **41**, 205504 (2008).

[75] G. Farkas and C. Tóth, *Proposal for attosecond light pulse generation using laser induced multiple-harmonic conversion processes in rare gases*, Physics Letters A **168**, 447 (1992).

[76] M. Halmann and I. Laulicht, *Isotope Effects on Vibrational Transition Probabilities. III. Ionization of Isotopic H_2, N_2, O_2, NO, CO, and HCl Molecules*, J. Chem. Phys. **43**, 1503 (1965).

[77] R. W. Nicholls, *Franck-Condon factors for ionizing transitions of O_2 , CO, NO and H_2 and for the NO + ($A\ ^1-\Sigma X\ ^1\Sigma$) band system*, J. Phys. B: At. Mol. Opt. Phys. **1**, 1192 (1968).

[78] J. M. Luis, M. Torrent-Sucarrat, M. Solà, D. M. Bishop and B. Kirtman, *Calculation of Franck-Condon factors including anharmonicity: Simulation of the $C_2H_4^+\tilde{x}\ ^2B_{3u} \leftarrow C_2H_4\tilde{x}\ ^1A_g$ band in the photoelectron spectrum of ethylene*, J. Chem. Phys. **122**, 184104 (2005).

[79] J. van Tilborg, T. K. Allison, T. W. Wright, M. P. Hertlein, Y. Liu, H. Merdji, R. W. Falcone and A. Belkacem, *EUV-driven femtosecond dynamics in ethylene*, Journal of Physics: Conference Series **194**, 012015 (2009).

[80] H. Kallmann and F. Reiche, *On the transfer of molecules through inhomogeneous force fields*, Z. Phys. **6**, 352 (1921).

[81] O. Stern, *Zur Methode der Molekularstrahlen. I*, Z. Phys. A **39**, 751 (1926).

[82] S. Y. T. van de Meerakker, H. L. Bethlem and G. Meijer, *Taming molecular beams*, Nature Phys. **4**, 595 (2008).

[83] H. Stapelfeldt, H. Sakai, E. Constant and P. B. Corkum, *Deflection of neutral molecules using the nonresonant dipole force*, Phys. Rev. Lett. **79**, 2787 (1997).

[84] Hoi Sung Chung, Bum Suk Zhao, Sung Hyup Lee, Sungu Hwang, Keunchang Cho Cho, Sang-Hee Shim, S. Wee Kyung Kang and Doo Soo Chung, *Molecular lens applied to benzene and carbon disulfide molecular beams*, J. Chem. Phys. **114**, 8293 (2001).

[85] R. Fulton, A. I. Bishop, M. N. Shneider and P. F. Barker, *Controlling the motion of coldmolecules with deep periodic optical potentials*, Nature Phys. **2**, 465 (2006).

[86] B. J. Sussman, J. G. Underwood, R. Lausten, M. Y. Ivanov and A. Stolow, *Quantum control via the dynamic Stark effect: Application to switched rotational wave packets and molecular axis alignment*, Phys. Rev. A **73**, 053403 (2006).

[87] R. Freeman, P. Bucksbaum, H. Milchberg, S. Darack, D. Schumacher and M. Geusic, *Above-threshold ionization with subpicosecond laserpulses*, Phys. Rev. Lett. **59**, 1092 (1987).

[88] D. Pavicic, K. F. Lee, D. M. Rayner, P. B. Corkum and D. M. Villeneuve, *Direct Measurement of the Angular Dependence of Ionization for N_2, O_2, and CO_2 in Intense Laser Fields*, Phys. Rev. Lett. **98**, 243001 (2007).

[89] Z. Chen, T. Morishita, A.-T. Le and C. D. Lin, *Analysis of two-dimensional high-energy photoelectron momentum distributions in the single ionization of atoms by intense laser pulses*, Phys. Rev. A **76**, 043402 (2007).

[90] M. Abu-samha and L. B. Madsen, *Theory of strong-field ionization of aligned CO_2*, Phys. Rev. A **80**, 023401 (2009).

[91] L. Holmegaard, J. H. Nielsen, I. Nevo, H. Stapelfeldt, F. Filsinger, J. Küpper and G. Meijer, *Laser-Induced Alignment and Orientation of Quantum-State-Selected Large Molecules*, Phys. Rev. Lett. **102**, 023001 (2009).

[92] I. Nevo, L. Holmegaard, J. H. Nielsen, J. L. Hansen, H. Stapelfeldt, F. Filsinger, G. Meijer and J. Küpper, *Laser-induced 3D alignment and orientation of quantum state-selected molecules*, Phys. Chem. Chem. Phys. **11**, 9912 (2009).

[93] L. Holmegaard, J. L. Hansen, L. Kalhøj, S. L. Kragh, H. Stapelfeldt, F. Filsinger, J. Küpper, G. Meijer, D. Dimitrovski, M. Abu-samha, C. P. J. Martiny and L. B. Madsen, *Photoelectron angular distributions from strong-field ionization of oriented molecules*, Nature Physics **6**, 428 (2010).

[94] S. De, I. Znakovskaya, D. Ray, F. Anis, N. G. Johnson, I. A. Bocharova, M. Magrakvelidze, B. D. Esry, C. L. Cocke, I. V. Litvinyuk and M. F. Kling, *Field-Free Orientation of CO Molecules by Femtosecond Two-Color Laser Fields*, Phys. Rev. Lett. **103**, 153002 (2009).

[95] C. M. Dion, A. Keller and O. Atabek, *Orienting molecules using half-cycle pulses*, Eur. Phys. J. D **14**, 249 (2001).

[96] E. Gershnabel, I. S. Averbukh and R. J. Gordon, *Orientation of molecules via laser-induced antialignment*, Phys. Rev. A **73**, 061401 (2006).

[97] H. Niikura, P. B. Corkum and D. Villeneuve, *Controlling vibrational wave packet motion with intense modulated laser fields*, Phys. Rev. Lett. **90**, 203601 (2003).

[98] B. J. Sussman, D. Townsend, M. Y. Ivanov and A. Stolow, *Dynamic stark control of photochemical processes*, Science **314**, 278 (2006).

[99] B. J. Sussman, M. Y. Ivanov and A. Stolow, *Nonperturbative quantum control via the nonresonant dynamic Stark effect*, Phys. Rev. A **71**, 051401(R) (2005).

[100] E. L. Eliel and A. H. Wilen, *Stereochemistry of Organic Compounds, Chapter 14* (Wiley, New York, 1994).

[101] G. Bringmann, A. Mortimer, P. Keller, M. Gresser, J. Garner and M. Breuning, *Atroposelective synthesis of axially chiral biaryl compounds*, Angew. Chem. Int. Ed. **44**, 5384 (2005).

[102] M. P. Johansson and J. Olsen, *Torsional Barriers and Equilibrium Angle of Biphenyl: Reconciling Theory with Experiment*, J. Chem. Theory Comput. **4**, 1460 (2008).

[103] F. Grein, *Twist Angles and Rotational Energy Barriers of Biphenyl and Substituted Biphenyls*, J. Phys. Chem. A **106**, 3823 (2002).

[104] V. Kumarappan, C. Z. Bisgaard, S. S. Viftrup, L. Holmegaard and H. Stapelfeldt, *Role of rotational temperature in adiabatic alignment*, J. Chem. Phys. **125**, 194309 (2006).

[105] K. Hoki, D. Kröner and J. Manz, *Selective preparation of enantiomers from a racemate by laser pulses: model simulation for oriented atropisomers with coupled rotations and torsions*, Chem. Phys. **267**, 59 (2001).

[106] S. Viftrup, V. Kumarappan, S. Trippel, H. Stapelfeldt, E. Hamilton and T. Seideman, *Holding and spinning molecules in space*, Phys. Rev. Lett. **99**, 143602 (2007).

[107] K. Faber, *Non-sequential processes for the transformation of a racemate into a single stereoisomeric product: Proposal for stereochemical classification*, Chem. Eur. J. **7**, 5004 (2001).

[108] Y. Fujimura, L. González, K. Hoki, J. Manz and Y. Ohtsuki, *Selective preparation of enantiomers by laser pulses: quantum model simulation for H_2POSH*, Chem. Phys. Lett. **306**, 1 (1999).

[109] M. Shapiro, E. Frishman and P. Brumer, *Coherently Controlled Asymmetric Synthesis with Achiral Light*, Phys. Rev. Lett. **84**, 1669 (2000).

[110] D. Kröner and B. Klaumünzer, *Stereoselective laser pulse control of an axial chiral molecular model system supporting four stereoisomers*, Chem. Phys. **338**, 268 (2007).

[111] D. Kröner and B. Klaumünzer, *Laser-operated chiral molecular switch: quantum simulations for the controlled transformation between achiral and chiral atropisomers*, Phys. Chem. Chem. Phys. **9**, 5009 (2007).

[112] M. Leibscher, I. Sh. Averbukh and H. Rabitz, *Molecular Alignment by Trains of Short Laser Pulses*, Phys. Rev. Lett. **90**, 213001 (2003).

[113] C. Z. Bisgaard, S. S. Viftrup and H. Stapelfeldt, *Alignment enhancement of a symmetric top molecule by two short laser pulses*, Phys. Rev. A **73**, 053410 (2006).

[114] K. F. Lee, I. V. Litvinyuk, P. W. Dooley, M. Spanner, D. M. Villeneuve and P. B. Corkum, *Two-pulse alignment of molecules*, J. Phys. B: At. Mol. Opt. Phys. **37**, L43 (2004).

[115] P. Brumer, E. Frishman and M. Shapiro, *Principles of electric-dipole-allowed optical control of molecular chirality.*, Phys. Rev. A **65**, 015401 (2001).

[116] B. Friedrich and D. Herschbach, *Manipulating Molecules via Combined Static and Laser Fields*, J. Phys. Chem. A **103**, 10280 (1999).

[117] B. Friedrich and D. Herschbach, *Enhanced orientation of polar molecules by combined electrostatic and nonresonant induced dipole forces*, J. Chem. Phys. **111**, 6157 (1999).

[118] H. Tanji, S. Minemoto and H. Sakai, *Three-dimensional molecular orientation with combined electrostatic and elliptically polarized laser fields*, Phys. Rev. A **72**, 063401 (2005).

[119] S. Ramakrishna and T. Seideman, *Torsional Control by Intense Pulses*, Phys. Rev. Lett. **99**, 103001 (2007).

[120] A. Nitzan and M. A. Ratner, *Electron Transport in Molecular Wire Junctions*, Science **300**, 1384 (2003).

[121] Z. J. Donhauser *et* al. , *Conductance Switching in Single Molecules Through Conformational Changes*, Science **292**, 2303 (2001).

[122] J. Chen and M. Reed, *Electronic transport of molecular systems*, Chem. Phys. **281**, 127 (2002).

[123] J. M. Seminario, A. G. Zacarias and J. M. Tour, *Theoretical Interpretation of Conductivity Measurements of a Thiotolane Sandwich. A Molecular Scale Electronic Controller*, J. Am. Chem. Soc. **120**, 3970 (1998).

[124] M. Čížek, M. Thoss and W. Domcke, *Theory of vibrationally inelastic electron transport through molecular bridges*, Phys. Rev. B **70**, 125406 (2004).

[125] C. Benesch, M. Čížek, M. Thoss and W. Domcke, *Vibronic effects on resonant electron conduction through single molecule junctions*, Chem. Phys. Lett. **430**, 355 (2006).

[126] C. Benesch, M. Čížek, J. Klimeš, I. Kondov, M. Thoss and W. Domcke, *Vibronic Effects in Single Molecule Conductance: First-Principles Description and Application to Benzenealkanethiolates between Gold Electrodes*, J. Phys. Chem. C **112**, 9880 (2008).

[127] J. Werschnik and E. K. U. Gross, *Quantum optimal control theory*, J. Phys. B: At. Mol. Opt. Phys. **40**, R175 (2007).

[128] S. Wu, M. T. Gonźalez, R. Huber, S. Grunder, M. Mayor, C. Schönenberger and M. Calame, *Twist Angles and Rotational Energy Barriers of Biphenyl and Substituted Biphenyls*, Nature Nanotech. **3**, 569 (2008).

[129] S. Loudwig and H. Bayley, *Photoisomerization of an Individual Azobenzene Molecule in Water: An On-Off Switch Triggered by Light at a Fixed Wavelength*, J. Am. Chem. Soc. **128**, 12404 (2006).

[130] C. Zhang, M.-H. Du, H.-P-Cheng, X.-G. Zhang, A. E. Roitberg and J. L. Krause, *Coherent Electron Trnsport through an Azobenzene Molecule: A Light-Driven Molecular Switch*, Phys. Rev. Lett. **92**, 158301 (2004).

[131] M. del Valle, R. Gutiérrez, C. Tejedor and G. Cuniberti, *Tuning the conductance of a molecular switch*, Nature Nanotech. **2**, 176 (2007).

[132] M. Abramowitz and I. A. Stegun, *Handbook of Mathematical Functions with Formulas, Graphs, and Mathematical Tables*, volume Washington : U.S. Government Printing Office, 1967 (Dover, New York, 1964), ninth dover printing, tenth gpo printing edition.

[133] A. R. Barnett, D. H. Feng, J. W. Steed and L. J. B. Goldfarb, *Coulomb wave functions for all real η and ρ*, Computer Physics Communications **8**, 377 (1974).

[134] M. Aymar, C. H. Greene and E. Luc-Koenig, *Multichannel Rydberg spectroscopy of complex atoms*, Rev. Mod. Phys. **68**, 1015 (1996).

[135] M. J. Frisch, G. W. Trucks, H. B. Schlegel, G. E. Scuseria, M. A. Robb, J. R. Cheeseman, J. A. Montgomery, Jr., T. Vreven, K. N. Kudin, J. C. Burant, J. M. Millam, S. S. Iyengar, J. Tomasi, V. Barone, B. Mennucci, M. Cossi, G. Scalmani, N. Rega, G. A. Petersson, H. Nakatsuji, M. Hada, M. Ehara, K. Toyota, R. Fukuda, J. Hasegawa, M. Ishida, T. Nakajima, Y. Honda, O. Kitao, H. Nakai, M. Klene, X. Li, J. E. Knox, H. P. Hratchian, J. B. Cross, V. Bakken, C. Adamo, J. Jaramillo, R. Gomperts, R. E. Stratmann, O. Yazyev, A. J. Austin, R. Cammi, C. Pomelli, J. W. Ochterski, P. Y. Ayala, K. Morokuma, G. A. Voth, P. Salvador, J. J. Dannenberg, V. G. Zakrzewski, S. Dapprich, A. D. Daniels, M. C. Strain, O. Farkas, D. K. Malick, A. D. Rabuck, K. Raghavachari, J. B. Foresman, J. V. Ortiz, Q. Cui, A. G. Baboul, S. Clifford, J. Cioslowski, B. B. Stefanov, G. Liu, A. Liashenko, P. Piskorz, I. Komaromi, R. L. Martin, D. J. Fox, T. Keith, M. A. Al-Laham, C. Y. Peng, A. Nanayakkara, M. Challacombe, P. M. W. Gill, B. Johnson, W. Chen, M. W. Wong, C. Gonzalez and J. A. Pople, *Gaussian 03, Revision C.02*, Gaussian, Inc., Wallingford, CT, 2004.

[136] A. Toniolo and M. Persico, *Efficient calculation of Franck-Condon factors and vibronic couplings in polyatomics*, J. Comput. Chem. **22**, 968 (2001).

[137] F. Ansbacher, *A note on the overlap integral of 2 harmonic oscillator wave functions*, Z. Naturforschg. **14a**, 889 (1959).